

## **Final Technical Report**

**Purchase Request Number: N68936-01-C-0094**

**Sponsor: Naval Air Warfare Center**

**Agency: U.S. Department of Defense**

**Title: Kinematic and Dynamic Studies of the Coso Geothermal and  
Surrounding Areas.**

**Technical Proposal Title: Pliocene to Recent Kinematics of the Wild  
Horse Mesa and Coso Wash: An Integrated Study Using Micropolar  
Theory and Paleomagnetic Determinations to Examine Spatial and  
Temporal Variations in Strain.**

**Prepared by:  
Jonathan C. Lewis  
Department of Geosciences  
University of Massachusetts  
Amherst, MA 01003**

**and**

**Christopher J. Pluhar  
Department of Earth Sciences  
University of California  
Santa Cruz, CA 95064**

**12 September 2003**

**DISTRIBUTION STATEMENT A**  
**Approved for Public Release**  
**Distribution Unlimited**

**Purchase Request Number: N68936-01-C-0094**

**20030929 033**

# REPORT DOCUMENTATION PAGE

Form Approved  
OMB No. 0704-0188

Public reporting burden for this collection of information is estimated to average 1 hour per response, including the time for reviewing instructions, searching data sources, gathering and maintaining the data needed, and completing and reviewing the collection of information. Send comments regarding this burden estimate or any other aspect of this collection of information, including suggestions for reducing this burden to Washington Headquarters Service, Directorate for Information Operations and Reports, 1215 Jefferson Davis Highway, Suite 1204, Arlington, VA 22202-4302, and to the Office of Management and Budget, Paperwork Reduction Project (0704-0188) Washington, DC 20503.

PLEASE DO NOT RETURN YOUR FORM TO THE ABOVE ADDRESS.

1. REPORT DATE (DD-MM-YYYY) 09-12-2003		2. REPORT DATE Final Technical Report		3. DATES COVERED (From - To) Nov 2001 -- Sept 2003	
4. TITLE AND SUBTITLE Kinematic and Dynamic Studies of the Coso Geothermal and Surrounding Areas. (Pliocene to Recent Kinematics of the Wild Horse Mesa and Coso Wash: An Integrated Study Using Micropolar Theory and Paleomagnetic Determinations to Examine Spatial and Temporal Variations in strain				5a. CONTRACT NUMBER N68936-01-C-0094	
				5b. GRANT NUMBER	
				5c. PROGRAM ELEMENT NUMBER	
				5d. PROJECT NUMBER	
				5e. TASK NUMBER	
6. AUTHOR(S) Jonathan C. Lewis (a) Christopher J. Pluhar (b)				5f. WORK UNIT NUMBER	
7. PERFORMING ORGANIZATION NAME(S) AND ADDRESS(ES) (a) Dept. Geosciences, Univ. Massachusetts, Amherst, MA 01003 (b) Dept. Earth Sci., Univ. Calif., Santa Cruz, CA 95064				8. PERFORMING ORGANIZATION REPORT NUMBER 5-28108	
9. SPONSORING/MONITORING AGENCY NAME(S) AND ADDRESS(ES)				10. SPONSOR/MONITOR'S ACRONYM(S) NAVAIR	
				11. SPONSORING/MONITORING AGENCY REPORT NUMBER DI-MISC-80711A	
12. DISTRIBUTION AVAILABILITY STATEMENT non-classified activity, cleared for public release					
13. SUPPLEMENTARY NOTES					
14. ABSTRACT					
15. SUBJECT TERMS seismicity, volcanism, kinematics, strain, paleomagnetism, geothermal field					
16. SECURITY CLASSIFICATION OF:			17. LIMITATION OF ABSTRACT	18. NUMBER OF PAGES	19a. NAME OF RESPONSIBLE PERSON
a. REPORT	b. ABSTRACT	c. THIS PAGE			19b. TELEPHONE NUMBER (Include area code)

## Table of Contents

<b>TABLE OF CONTENTS</b> .....	<b>2</b>
<b>1.0 EXECUTIVE SUMMARY</b> .....	<b>3</b>
<b>2.0 INTRODUCTION</b> .....	<b>4</b>
2.1 PROJECT BACKGROUND.....	4
2.2 TECTONIC SETTING.....	4
2.2.1 Seismicity.....	4
2.2.2 Volcano-stratigraphy.....	5
2.2.3 Shearing history.....	5
2.3 TECHNICAL APPROACH.....	6
2.3.1 Micropolar Theory.....	6
2.3.2 X-Ray Fluorescence.....	7
2.3.3 Paleomagnetism.....	9
Paleomagnetism of Sediments.....	9
Paleomagnetism of Lavas.....	10
2.3.4 Geochronology.....	11
<b>3.0 RESULTS</b> .....	<b>11</b>
3.1 SEISMOGENIC STRAIN.....	11
3.2 EXPOSED OUTCROP-SCALE BRITTLE FAULTS.....	11
3.3 UNIT CORRELATION FROM X-RAY FLUORESCENCE GEOCHEMISTRY.....	13
3.4 PALEOMAGNETISM.....	14
3.4.1 Sedimentary Sections.....	14
3.4.2 Lava Localities.....	15
3.5 GEOCHRONOLOGY.....	18
<b>4.0 DISCUSSION</b> .....	<b>18</b>
<b>5.0 CONCLUSION</b> .....	<b>21</b>
<b>TABLES</b> .....	<b>22</b>
<b>FIGURES</b> .....	<b>35</b>
<b>REFERENCES CITED</b> .....	<b>70</b>
<b>APPENDIX A</b> .....	<b>72</b>
SUPPLEMENTARY GEOCHEMICAL DATA: V, Ni, Cr.....	72
<b>APPENDIX B</b> .....	<b>74</b>
<sup>40</sup> Ar/ <sup>39</sup> Ar GEOCHRONOLOGY DATA.....	74
<b>APPENDIX C</b> .....	<b>90</b>
LATERAL EXTENT OF ERUPTIVE UNITS.....	90

## 1.0 Executive Summary

During the final stages of this project we encountered some delays in securing a no-cost extension that was requested in order to complete additional analyses that were not originally anticipated. These analyses include one additional radiometric age and geochemical analyses of lava flow units. This Final Technical Report serves to convey the results of the efforts of Tasks 1, 2, 3 and 4 (Table 1.1). Because Task 4 represents Integration and Interpretation, the results contained herein largely reflect efforts under this task. It is expected that two manuscripts for publication will stem directly from the efforts of this project. An additional 4 manuscripts for publication are expected to result from efforts that set the stage for the work conducted under this contract.

Seismogenic strain at the Wild Horse Mesa suggests that deformation is partitioned with depth, whereas the time-integrated record of shearing suggests a much finer spatial scale of deformation partitioning. Active deformation is characterized by subhorizontal east-west maximum stretching both above and below a depth of 5 km. At the shallower crustal levels maximum shortening is subvertical and associated with crustal thinning, whereas at the deeper crustal levels maximum shortening is subhorizontal and associated with horizontal dextral shearing. Both levels record plane strain and evidence for block rotation at rates different than for the large-scale continuum. The time-integrated record of shearing at upper Wild Horse Mesa indicates that horizontal dextral shearing with subhorizontal west southwest-east northeast maximum stretching is the dominant strain geometry recorded. Lesser crustal thickening and crustal thinning are recorded as well, and the faults that accommodate these strains are spatially intermixed with the more dominant strike-slip faults that accommodate horizontal shearing. Statistical results at 90% confidence suggest that the horizontal shearing is characterized by prolate strain and non-zero relative vorticity. The former is consistent with transtension and the latter is in accord with clockwise vertical-axis rotation (viewed down; here and throughout this document vertical-axis rotation sense is given looking down) of crustal blocks.

Pliocene lavas and sediments of the Wild Horse Mesa exhibit this clockwise vertical-axis rotation of fault bounded blocks. We measure these finite rotations paleomagnetically, relative to two different reference frames. At two localities we average secular variation through sedimentary sections to reveal rotation or its absence relative to paleogeographic north. Where sediments are lacking we sampled geochemically-identifiable, areally-extensive lavas to measure the rotation of localities relative to one another. In the Coso Wash the fanglomerate member of the Coso formation exhibits approximately  $21.6^{\circ} \pm 10.7^{\circ}$  clockwise vertical-axis rotation since ca. 3 Ma. In the Wild Horse Mesa, 3.1-3.4 Ma lavas exhibit about  $12.0^{\circ} \pm 4.6^{\circ}$  (weighted mean) clockwise vertical-axis rotation relative to outcrops near Dead End Cabin. In aggregate the data suggest that the Wild Horse Mesa and Coso Wash hosts a segment of the Eastern California shear zone which accommodates dextral shear by vertical-axis rotation of blocks above a deep-seated right-lateral fault. Using the measured finite rotation and a pinned block model, we calculate a minimum of 1.5 km of dextral offset across the Wild Horse Mesa oriented N30°W since ca. 3.1 Ma.

At adjoining sites in the greater Coso Geothermal Area and the Darwin Plateau other workers suggest no vertical-axis rotation. However, the former exhibits down to the west tilting. Thus, style of block rotation appears partitioned: vertical-axis rotation in the Wild Horse Mesa and horizontal-axis rotation (tilting) in the geothermal area,



suggesting partitioning of the master faults controlling the near-surface rotation and tilting.

## 2.0 Introduction

### 2.1 Project Background

The overarching goal of this study is to establish an understanding of the kinematic history of the Wild Horse Mesa and adjacent crust in the vicinity of the Coso geothermal field. The approach adopted takes advantage of the fact that the basement of the Wild Horse Mesa is young (late Cenozoic), faulted, well-exposed and actively accommodating seismogenic strain. In particular, we have employed geochemistry, paleomagnetism and geochronology to constrain volcano-stratigraphy, the ages of lava flows and the finite rotation of flows after cooling. Seismic events have been used to characterize active strain and outcrop-scale brittle faults have been used to examine the time-integrated record of shearing deformation. The net result of this work is (1) an understanding of the geometries and ages of the basalt and andesite flows that dominate the volcanic basement of the Wild Horse Mesa, and (2) a comparison between the instantaneous non-recoverable strain reflected in earthquake data and the time-integrated brittle shearing reflected in the faults that deform, and produce finite block rotations of the Wild Horse Mesa.

### 2.2 Tectonic Setting

The Coso geothermal field is approximately centered at a right-releasing step in the diffuse strike-slip boundary between the Sierran microplate and the southern Basin and Range province to the southeast (Unruh et al. 2002). The Wild Horse Mesa lies immediately east of the geothermal field and is well situated to compare seismogenic (i.e., instantaneous) strain with the time-integrated strain recorded by outcrop-scale brittle faults and deflection of paleomagnetic declinations within the late Cenozoic lava flows that compose the mesa. This location is the site of faulting that probably links horizontal shearing (i.e., strike-slip dominated strain) in the Indian Wells Valley with the horizontal shearing north of Wild Horse Mesa. The latter shearing presumably links with the Owen Valley fault zone in the area of the 1872 Owens Valley earthquake rupture.

The lava flows that form Wild Horse Mesa are transected by an anastomosing network of normal fault scarps (i.e., the step-faulted terrane of Duffield et al. 1980) indicating a history of crustal thinning within a strike-slip fault system. The dominant fault scarps are northwest-facing in northern Wild Horse Mesa and merge into east- and west-facing scarps in southern Wild Horse Mesa. The lava flows cut by these faults are ca. 3.6 Ma or younger. Stratigraphic and structural observations (see Monastero et al. 2002 for a review) indicate that significant northwest dextral shearing initiated in this region between ca. 3.5 and 2 Ma, and geodetic data (Dixon et al. 2000) indicate that approximately 22% of Pacific-North America plate motion is presently accommodated here (~11mm/yr). In total, the Wild Horse Mesa provides a unique opportunity to examine the kinematic evolution of a youthful, transtensional system.

#### 2.2.1 Seismicity

Seismicity in the vicinity of the Coso Geothermal field is heterogeneously distributed (focal mechanisms and locations for the seismic events used in this study include events provided by E. Hauksson). Three notable clusters of seismic events, in

the eastern part of the Indian Wells Valley, beneath the southern part of Wild Horse Mesa and immediately north of Wild Horse Mesa, have been used to delineate to a first-order the geometry of the right-releasing stepover that separates the Sierran microplate from the southern Basin and Range Province (Figure 2.1). The geometry of this boundary will no doubt be refined as the catalog of well-located seismic events becomes larger.

The fact that the Wild Horse Mesa occupies a position within the right-releasing stepover in the locus of strike-slip deformation east of the Sierra Nevada is apparent on the basis of seismogenic strain. Seismicity from 0 – 5 km accommodates crustal thinning whereas that from 5 – 8 km accommodates horizontal shearing (Unruh et al. 2002). Additionally, the former seismic events are somewhat spatially disorganized, whereas the latter define a planar seismic source zone that strikes subparallel to the trajectory of Sierran-North America motion (Dixon et al. 2000; Unruh et al. 2002).

### 2.2.2 Volcano-stratigraphy

The Coso volcanic field is composed of multiple generations and centers of late Cenozoic alkalic to subalkalic (Novak and Bacon, 1986) volcanism spanning the last 6 Ma that Duffield, Bacon and coworkers have studied extensively (e.g. Bacon et al., 1982; Duffield and Bacon, 1981). We retain the terminology of Duffield et al. (1980), defined by weight %  $\text{SiO}_2$ : basalt 48-54%, andesite 54-60%, and dacite 60-65%.

Volcanism in the Coso Range began with basaltic through dacitic lavas erupted 5-6 Ma at the present southeastern edge of Owens Lake. The bulk of the rocks studied here derive from the Wild Horse Mesa (Figure 2.2) which is composed of basaltic through dacitic lavas previously thought to have erupted between 3 and 4 Ma into an oblique pull-apart basin. This was the most voluminous phase of eruption in the Coso Range during the late Cenozoic. Following this, dacite flows through rhyolite pyroclastics erupted between 2.5 and 3.5 Ma at the western edge of the range near Haiwee Reservoir. Later, a handful of basalt and andesite eruptions occurred around the Tertiary-Quaternary boundary near Renegade Canyon on the Wildhorse Mesa. Since 1.1 Ma, bimodal basalt and small-volume rhyolite volcanism has dominated the vicinity of the Coso geothermal field, having erupted through a Mesozoic basement highland. This study focuses on the most voluminous and areally extensive units, basalts and andesites of the Wild Horse Mesa. These areally extensive units provide constraints on fault offsets and fault kinematics (vertical-axis block rotation).

### 2.2.3 Shearing history

Wild Horse Mesa provides a time-integrated record of shearing in the form of outcrop-scale brittle faults. Wild Horse Mesa is characterized by a systematic decrease in elevation from east to west. The mesa consists of relatively flat, slightly west-tilting topographic benches that step down in elevation across dominantly west-facing normal-fault scarps. Canyons cut the mesa at high angles to the overall topographic relief, forming relatively deep, largely northeast-trending scars in which the basement of the mesa is well exposed. Topographically the lower reaches of these canyons cut the western and southwestern parts of the mesa, whereas the upper reaches cut the eastern and northeastern parts of the mesa. Outcrop-scale faults have been observed and kinematic constraints measured in lava flows of (1) the lower section of Petroglyph Canyon, (2) Petroglyph Canyon from near the junction with Horse Canyon to its upper reaches near the end of the "Big Petroglyphs" unimproved road, (3) the lower section of Dead End Canyon, (4) the middle section of Black Canyon, and (5) the middle and

upper sections of Sheep Canyon (Figure 2.3). These data have been examined for quality purposes and subsequently divided on the basis of location. Observations from Dead End and Black Canyons were sparse and are not described further.

Data from lower Petroglyph Canyon, and from Sheep Canyon and the upper parts of Petroglyph Canyon provide numerous kinematic constraints on the shearing history of Wild Horse Mesa (Table 2.1 and Figure 2.4). These data have been subdivided on the basis of their distribution in the field. The topographically highest data station in lower Petroglyph Canyon is approximately 300 m lower than the lowest data station from the upper Petroglyph Canyon/Sheep Canyon area. The data from the region of Sheep and upper Petroglyph Canyons have been combined to form the upper Wild Horse Mesa data subset. The data from the area around lower Petroglyph Canyon have been consolidated into the lower Wild Horse Mesa data subset.

The faults examined at the upper and lower Wild Horse Mesa display a wide variety of orientations and accommodate normal, left-lateral, right-lateral and thrust displacements (Figure 2.5). In spite of the transtensional setting, thrust faults make up a substantial fraction of the entire data set. It is noteworthy that the faults examined in the field are not necessarily spatially associated with the major fault scarps that are expressed so vividly across the step-faulted terrane. Field observations suggest that if outcrop-scale faults with readily interpreted kinematic indicators exist in these locations, they are largely covered with talus. High-quality fault data are most readily available in canyon-wall exposures immediately adjacent to the traces of major fault scarps (e.g., within approximately 100 meters of where major scarps crossed canyons).

## 2.3 Technical Approach

### 2.3.1 Micropolar Theory

Partial strain tensors were determined by treating the crust as a micropolar continuum (Twiss et al. 1991; Twiss et al. 1993; Unruh et al. 2002). In essence this entails treating the crust as a granular material in which grains are free to rotate at different rates than the large-scale continuum. The resulting model consists of five parameters, three Euler angles that define the orientations of the principal strain rates (i.e.,  $d_1 \geq d_2 \geq d_3$ ; lengthening is reckoned positive); a deformation-rate parameter  $D \equiv (d_2 - d_3)/(d_1 - d_3)$ , which defines the relative magnitudes of the principal strain rates; and a relative vorticity parameter  $W \equiv (\omega_{13} - w_{13})/0.5(d_1 - d_3)$ , which defines a normalized difference between the local vorticity of individual fault blocks  $\omega_{13}$  and the large-scale vorticity of the deforming continuum  $w_{13}$  about the  $d_2$  axis.

This approach can be used to examine earthquake focal mechanisms (as in Figure 2.1, and in Lewis et al. 2003; Unruh et al. 2003; Unruh et al. 2002; Unruh et al. 1996) or fault-slip data (as in Figures 3.3-3.6, and in Unruh & Twiss 1998). The fundamental difference in these two applications is (1) nodal plane ambiguity in the former and no such ambiguity in the latter, and (2) modeling instantaneous deformation in the former (i.e., essentially strain rate) and modeling part of the time-integrated (i.e., finite) strain in the latter.

The robustness of the best-fitting strain tensors is evaluated using bootstrap statistics to constrain the variation among the five model parameters.  $D$  values statistically less than or greater than 0.5 indicate deviatoric transtension or deviatoric transpression, respectively.  $W$  values statistically different than zero indicate crustal block rotation that is different than that of the large-scale continuum. For seismogenic deformation  $W$  is interpreted in terms of rotation rates because the seismic record essentially provides

constraints on incremental deformation. For the rock record,  $W$  is considered to reflect differences in finite block rotation relative to that of the large-scale continuum.

The seismogenic deformation at Wild Horse Mesa was evaluated starting with the results of Unruh et al. (2002). Two primary analyses were performed: 1) tests of differing depths for the transition from crustal thinning at shallow levels to horizontal shearing at deeper levels, and 2) statistical evaluations of non-plane strain and non-zero relative vorticity.

In determining best-fitting strain tensors to fault-slip data the data were sorted in a variety of ways in order to maximize the possibility that the data reflected homogeneous strain. Given the time-integrated nature of the fault data, this sorting requires multiple approaches. Four primary means of subdividing the data have been used. First the data are examined on the basis of where they occur in the field, that is, spatially. Due to the sparseness of kinematic indicators this approach is somewhat limited. Nonetheless, two stations (203 and 213, see Table 2.1) yielded enough fault-slip data to warrant this approach. Second, pooled data are examined in hopes of finding multiple strain geometries that are viable. These geometries are then used to subdivide that data based on the affinity of a data point for one strain tensor over another using a minimum misfit criterion. This approach is "blind to" the spatial distribution of the fault data. Third, fault data are subdivided on the basis of the style of deformation accommodated. In this approach, for example, normal faults and strike-slip faults are separated. Fourth, clusters of similarly oriented kinematic  $P$  and  $T$  axes are used to subdivide the data. This is typically done using Kamb contour plots of the  $P$  and  $T$  axes.

The primary spatial subdivision of the brittle fault data is based on position within Wild Horse Mesa. The topographically highest observation from lower Wild Horse Mesa is approximately 300 m lower than the lowest observation from upper Wild Horse Mesa. Moreover, the fault traces mapped by Duffield et al. (1980) display distinct patterns in these two areas. Lower Wild Horse Mesa as we have defined it is dominated by north to slightly northeast trending fault traces. Upper Wild Horse Mesa is likewise characterized by this fault trace geometry, but also includes a set of northwest-trending fault traces (Figure 2.3). The fault data from lower Wild Horse Mesa are heterogeneous and only one homogenous subset is apparent, as discussed below.

The data from upper Wild Horse Mesa have been divided using a combination of approaches. The fault slip data from station 203 suggest two primary styles of deformation, crustal thickening and horizontal shearing. These two styles of strain are also apparent in the data from other parts of upper Wild Horse Mesa. Because stations 203 and 213 are within about 1 km of one another and within about 2 km of all of the remaining observations from upper Wild Horse Mesa, it is considered reasonable to initially pool all of the data from the upper Wild Horse Mesa. These data were then subdivided on the basis of the type of faulting, using dip-slip dominated normal faulting, strike-slip dominated horizontal shearing and dip-slip dominated thrust faulting as categories.

### 2.3.2 X-Ray Fluorescence

The intention of this task is to fingerprint eruptive units in order to compare paleomagnetic remanence directions from the same unit at different localities. Separation of units by appearance in the field or in thin section is not sufficiently diagnostic or rigorous. Therefore, we sought geochemical means.



Throughout this report the term eruptive unit signifies a lava flow or flows exhibiting a (within-locality) uniform paleomagnetic remanence direction and, usually, a tightly defined chemistry. These criteria indicate rapid eruption and allow rigorous correlation. Identification of units permits the measurement of relative vertical-axis rotation of fault bounded blocks between localities. In the process a much more detailed understanding of stratigraphic relations has emerged than previous studies have yielded (Novak and Bacon, 1986; Duffield and Bacon, 1981). Our data indicate that previous models of the geochemical evolution of the Pliocene volcanic field at Wild Horse Mesa require amendment.

Using the method of Johnson et al. (1999) we prepared 65 lava samples for major (oxides of Na, Mg, Al, Si, P, K, Ca, Ti, Mn, and Fe) and trace (Rb, Sr, Y, Zr, and Nb) element analysis by X-Ray Fluorescence (XRF) spectroscopy. Table 2.2 shows raw results for these samples. Supplementary data on V, Ni and Cr for selected samples are included in Appendix A. Each sample was processed and analyzed in duplicate to assess reproducibility of preparation procedures. The standard deviation reported is that calculated from measurement of the duplicate samples plus any repeated measurements. The standard deviation of individual measurements should not be confused with the true chemical variability throughout a flow or eruptive unit.

Major elements and trace elements were analyzed using 2 different settings on the same Rh x-ray tube (45 kV, 50 mA for major elements and 90 kV, 30 mA for trace elements). During analysis of a sample batch, several quality assurance/quality control samples were run. International standards BIR-1 and AGV-1 were each analyzed as a calibration check once or twice during each 3-day analysis session. Counting standard RLGM was analyzed at least once each day. Remeasurement of selected samples from previous batches further ensured consistency between sessions. These steps were all taken to ensure the accuracy of XRF analysis.

To gauge the real chemical variation of flows within eruptive units, we typically selected two samples from each eruptive unit at a given locality for analysis. Therefore, the spread on concentrations for a given unit reflects the real chemical variation, both due to initial emplacement conditions and variable (though usually minimal) hydrothermal alteration and weathering. Element concentrations were normalized to 100%, ignoring volatile content (Johnson et al., 1999), usually an indicator of post-emplacement hydrothermal and weathering processes rather than parent magma content.

Geochemistry alone is insufficient to fully distinguish eruptive units. Some lava flows with opposite paleomagnetic polarity exhibit similar geochemistry. Thus, we fingerprint units using combined geochemistry and paleomagnetism. Details of paleomagnetic techniques and results will be discussed in subsequent sections.

Some workers have used geochemistry of major elements (e.g., Monastero et al., 1997) sometimes combined with paleomagnetism (e.g., Wells et al., 1989) to correlate widely separated outcrops of the same lavas. However, we prefer correlation using mainly trace elements (Rb, Sr, Y, Zr, and Nb). This is because major element geochemistry can vary significantly during the course of an eruption due to differentiation processes and zoned magma chambers. Since we require separation of units with similar bulk chemistry (and appearance) their bulk chemistries overlap. For this reason, we move to trace elements. Partition coefficients into basaltic minerals are low in these elements and of similar magnitude, such that their concentration and especially their *ratio* during an individual eruption is likely to be invariant for basalts

(and increase in variability with larger silica content) even in the face of some differentiation.

### 2.3.3 Paleomagnetism

One method for revealing the kinematics of fault blocks in the study area is to measure finite rotations using paleomagnetic techniques. Two methods of measuring block rotation are described. Raw paleomagnetic data are not included here due to space constraints. These data can be found in Pluhar's thesis (Pluhar, 2003)

#### Paleomagnetism of Sediments

In the most simple case, paleomagnetic measurements of vertical-axis rotations are made on sediments. Sampling through a stratigraphic section typically allows averaging of secular variation of Earth's magnetic field. In addition there is no ambiguity on the exact bedding correction to apply, since all but fanglomerate is deposited close to horizontal. Thereby, the mean direction of a group of samples through such a section points to paleogeographic north for the tectonic block on which the sediments ride.

We sampled sediments at three localities (see Figure 2.2 for locations). The Haiwee Reservoir (HR) lacustrine section yielded poor directional results and will be discussed no further. The White Hills section B (WHB) is also lacustrine and thought to be Pleistocene (Duffield et al., 1980). Both of these lacustrine sections were sampled by collection of large, oriented handsamples which were then subdivided into multiple specimens. The Coso Wash (CWA) section spans part of the Coso formation fanglomerate member and is thought to be late Pliocene in age (Duffield et al., 1980). Each sample collected from this locality was individually carved, a plastic box placed over the *in situ* sample, and orientation recorded. This locality is unique in that it contains sediment as the majority of section beneath an angular unconformity capped by pyroclastics and a dacite (Duffield and Bacon, 1981, mapping unit Tdo). This allows a direct radiometric tie point, discussed in the geochronology section, to the magnetic reversal timescale. For the capping dacite, paleomagnetic techniques described in the next section for lavas were applied.

Oriented sediment samples were analyzed by standard paleomagnetic techniques including thermal and/or alternating field (AF) stepwise demagnetization experiments and principal component analysis (PCA) (Kirschvink, 1980; Cogne, 2003) of the resulting demagnetization paths. For sediments, thermal demagnetization was the preferred technique because of the possibility of secondary chemical remanent magnetization components. PCA yields the primary or characteristic remanent magnetization (ChRM) direction for each specimen. Where multiple specimens were derived from a single oriented hand sample, all ChRMs determined for the specimens were averaged to calculate a mean ChRM for the sample. For each locality, the mean of all independently-oriented ChRMs yields paleogeographic north.

For locality WHB, standard tilt corrections were applied to restore beds to original horizontality. However, for CWA, the fanglomerate locality, the assumption of original horizontality is erroneous. Alluvial fans typically exhibit slopes (i.e., original dips) of 5°-10° as do the modern fans in Coso Wash. Thus at CWA we restore beds tilting 25° southeastward to either 5° or 10° southeastward, the minimum restoration required that is still geologically reasonable given no change in paleo-drainage direction. Restoration to original dips in some other direction for the most part result in even larger clockwise rotations than those observed for the minimum corrections (see results section).

### Paleomagnetism of Lavas

The major Cenozoic rock types available in the study area are basalt and andesite. Lavas are often less than ideal for averaging secular geomagnetic variation because many flows can be emplaced in a very short period, yielding a thick stratigraphic section representing the same geologic instant, and therefore, paleomagnetic direction. However, we utilize such rocks because they present other advantages for paleomagnetic studies. Lavas very faithfully record Earth's magnetic field, and generally this paleomagnetic signal can be measured more accurately and precisely than that in sediments. Therefore, if a laterally-extensive lava flow can be identified, measuring the directional differences from one locality to another reveals the relative rotation between localities to within about  $\pm 5^\circ$ .

In this discussion we refer to individual cooling units as lava flows, and groups of lava flows which exhibit strong evidence of rapid emplacement as eruptive units (called flow fields by some workers). Evidence of rapid emplacement are: statistically indistinguishable remanence direction between successive flows and/or identical geochemical "fingerprint" (see preceding section).

We sampled 22 localities of late Pliocene and early Pleistocene lavas. Localities varied in character, representing anywhere from one to twenty-one individual lava flows. At most localities (BC, CWA, UDC, LB, PC, HS, HSB, HSD, SP, CF, CHS, RCB, RCC, RCD, RCE) six or more oriented drill cores were collected from each lava flow. At a few localities (AL, RC, BD) as few as three samples per flow were collected due to time constraints or logistical limitations. At one locality we collected oriented hand samples for reconnaissance purposes (LDC). These data are identified as such in subsequent sections. Results from localities CMA, CMC, and MSA, yielded data of minor importance which will be discussed in passing only. For all lava samples except handsamples, sun compass or sight point corrections were applied to account for local magnetic anomalies.

Lava specimens drawn from the samples were stepwise thermal or AF demagnetized. Specimens typically exhibited univectorial decay to the origin unless affected by lightning strikes. Since AF demagnetization is far more effective than thermal for isolating magnetization components in lightning-affected samples, it was the favored method for lavas. Demagnetization data were analyzed using PCA, and mean directions were calculated for each lava flow from the sample ChRMs for that flow. For eruptive units that contain multiple lava flows and for which flow means are statistically indistinguishable from one another, the flow mean directions were averaged to yield a unit mean direction for that locality. Thus for the tectonic analysis we compare unit mean directions between localities.

Attitude of lava flow tops were recorded as an estimate for paleohorizontal at flow emplacement. These attitudes were measured in the field where possible or taken from aerial photographs using a parallax bar by standard methods. However, the assumption of original horizontality of flow tops is obviously a simplification, since lava flows downslope. For tilt corrections in this study we restore flow tops to horizontal unless otherwise noted.

In addition to lavas, we collected and analyzed airfall pumice samples from two localities (RHT and RDT). These samples appear to have acquired much of their magnetization during flight or before achieving a final position in the aggrading pumice pile and thus carry many components and appear unstable at moderate to high demagnetization steps. In addition, thermal demagnetization tends to break samples



apart by differential expansion of the large micas contained therein. Thus, these low quality data will be discussed no further.

### 2.3.4 Geochronology

Radiometric dating was undertaken in order to better constrain the time spanned by the finite rotation determined paleomagnetically and by fault-slip inversion. Sebastien Nomade under the supervision of Paul Renne at Berkeley Geochronology Center (BGC) conducted 6 analyses for  $^{40}\text{Ar}/^{39}\text{Ar}$  geochronology in accordance with the statement of work. Techniques and many of the details of this effort can be found in BGC's attached report (Appendix B). Also presented are data for eight additional analyses conducted by Jonathan M.G. Glen and Sebastien Nomade at BGC (raw data, Appendix B) which have not yet been published elsewhere.

In conducting the six analyses in satisfaction of our contract, it was found that quartz and perhaps plagioclase xenocryst contamination of these samples was widespread in the Pliocene lavas. For this reason groundmass separates were favored. This fact should be kept in mind when judging the reliability of previous K/Ar whole rock ages (e.g., Duffield et al., 1980).

## 3.0 Results

### 3.1 Seismogenic Strain

The seismogenic deformation at Wild Horse Mesa was evaluated starting with the results of Unruh et al. (2002). Two primary analyses were performed: (1) tests of differing depths for the transition from crustal thinning at shallow levels to horizontal shearing at deeper levels, and (2) statistical evaluations of non-plane strain and non-zero relative vorticity. The results of the first analyses indicate that 5 km indeed represents the transition from crustal thinning to horizontal shearing. The results of the second analyses reveal that seismogenic deformation reflects plane strain partitioned in depth (i.e.,  $D = 0.5$ ) and that block rotation occurs at rates different than those for the large-scale continuum (i.e.,  $W$  is non-zero). For the shallow events (Figure 3.1),  $W = 0.456 (+0.283/-0.232)$ , at 95% confidence here and throughout, except if noted otherwise) and for the deeper events (Figure 3.2),  $W = 0.647 (+0.200/-0.426)$ . For deformation at shallow levels this value is consistent with north-viewed counterclockwise rotation, or clockwise rotation at a rate slower than the macrovorticity. Given the geometry of the well-developed west-facing fault scarps across Wild Horse Mesa, clockwise block rotation is the preferred interpretation. For deformation at deeper levels, the  $W$  value is consistent with counterclockwise vertical-axis rotation, or clockwise vertical-axis rotation at a rate slower than the macrovorticity. Considering that the seismic events define a northwest trending planar source zone, and that the boundary conditions are dominated by dextral shear, the latter interpretation is preferred.

Seismogenic strain at both structural levels is consistent with expectations given the transtensional setting. For shallower and deeper seismicity,  $d_1$  is subhorizontal and west southwest-east northeast trending. Crustal thinning at shallow levels is characterized by a subvertical  $d_3$ , whereas horizontal dextral shearing at deep levels is characterized by subvertical  $d_2$ .

### 3.2 Exposed Outcrop-Scale Brittle Faults

The lower Wild Horse Mesa faults that we examined are characterized by heterogeneously distributed kinematic P and T axes as well as diverse fault plane and

lineation orientations (Figure 2.5): To date, our attempts to parse these data into homogeneous subsets have yielded limited success. Inversion of the collective fault data for which we have high confidence yields an oblique strain tensor that indicates shallow south-plunging extension and shallow west-plunging shortening (not shown). The south-trending maximum stretching direction ( $d_1$ ) is quite different than the subhorizontal, nearly east-west trend that is characteristic of  $d_1$  for seismogenic deformation in the region (Figures 3.1 and 3.2). Nonetheless, the dominant solution geometries suggest that the shallow west northwest plunging P axis cluster apparent in Figure 2.5 reflects the existence of a homogeneous subset of fault slip data. Using this P axis maximum as a means of subdividing the data set results in the isolation of a fairly well-behaved data subset (Figure 3.3). In spite of the fact that this subset appears statistically homogeneous (i.e., the final positions for principal axes are clustered in Figure 3.3c), the resulting strain tensor is difficult to interpret in the context of the regional tectonics.

The upper Wild Horse Mesa faults display a less heterogeneous distribution of kinematic P and T axes than do the faults of lower Wild Horse Mesa. Moreover, the fault planes are somewhat organized with two sets apparent. The first set is dominated by subvertical faults that are either west or northwest striking. The second set is dominated by faults that strike north and dip moderately eastward. Nonetheless, these faults accommodate crustal thinning, crustal thickening and horizontal shearing. Generally speaking, these faults display lineations that are either approximately down dip or approximately strike parallel. As a consequence the faults have been subdivided into subsets on the basis of style; that is, normal faults, thrust faults and strike-slip faults.

Inverse modeling of the faults for which we have high confidence in our field observations yields three strain tensors. The results for the normal faults (Figure 3.4) and for the thrust faults (Figure 3.5) are statistically less robust than for the strike-slip faults (Figure 3.6) owing to the smaller numbers of observations. As a consequence, it is not possible to constrain non-plane strain or non-zero relative vorticity. In contrast, at 95% confidence the strike-slip faults suggest a strong bias toward a prolate strain tensor and non-zero relative vorticity (Figure 3.6, c and e). Accepting 90% confidence, it can be argued that these faults indeed accommodate prolate strain, consistent with transtension, and non-zero relative vorticity, consistent with counterclockwise vertical-axis rotation, or clockwise vertical-axis rotation at a rate slower than the macrovorticity. Given the regional history of dextral transtension, the latter interpretation of the relative vorticity result is preferred.

The inversion results for the upper Wild Horse Mesa faults are internally consistent and in general agreement with results for contemporary strain. The orientation of  $d_1$  is consistent for the strike-slip and normal faults; namely subhorizontal and west southwest-east northeast trending (compare Figures 3.4 and 3.6). Similarly, for the strike-slip faults and the thrust faults,  $d_3$  is consistently subhorizontal and north-south trending (compare Figures 3.5 and 3.6). Although these three fault subsets indicate strain that has partitioned at sub-km scales, the overall geometries of strain are in accord with the seismogenic strain (compare Figures 3.1 and 3.2 with Figures 3.4-3.6). The only noteworthy exception is the thrust faults, which reveal crustal thickening that is not apparent in the seismogenic deformation. The existence of crustal thickening, however, is not unexpected because of kinematic compatibility requirements during vertical-axis block rotation (Dewey 2002).

### 3.3 Unit Correlation from X-Ray Fluorescence Geochemistry

In order to map the pattern of block rotation it is necessary first to define laterally extensive eruptive units on which to perform paleomagnetic analyses. Duffield and Bacon (1981) defined much of the greater Wild Horse Mesa as a single unit called Basalt of Petroglyph Canyon. We subdivide this gross compositional unit into multiple new eruptive units each spanning a period shorter than that necessary for noticeable secular variation of Earth's magnetic field (about 200 years) and sharing a similar geochemistry. Each newly defined unit probably represents the outpouring from a single vent during a geologically short-lived eruption.

As stated previously, trace element concentrations are more likely to be invariant during an eruption than major elements, because they are little affected by differentiation. Figure 3.7 depicts Sr/Zr versus Rb/Nb ratios combined with paleomagnetic polarity for Pliocene Wild Horse Mesa volcanics. These ratios are chosen because, of all combinations of the five trace elements analyzed, they provide the best separation of units into discrete fields. This separation into distinct fields suggests a unique chemical fingerprint for each. Magnetic polarity is indicated on the figures as open symbols for reversed polarity, solid symbols for normal, and characters (asterisk, cross, etc.) for unknown polarity (e.g. for samples composed of drillhole cuttings). Using the diagram, we assign new eruptive unit names based on the probable eruptive source area of each unit. Classification into basalt, andesite, and dacite anticipates major element data presented in Figures 3.9-3.22.

We subdivide the former Basalt of Petroglyph Canyon into a redefined Petroglyph Canyon basalt, Silver Peak basalt, Cole Flat basalt, Haiwee Spring basalt, and Black Canyon flows (some of which were lumped into Duffield and Bacon's Petroglyph Canyon unit). Petroglyph Canyon basalt is easily distinguished from Black Canyon flows by polarity but not geochemistry. On the other hand, Petroglyph Canyon basalt is separated from Silver Peak basalt by trace element chemistry but not paleomagnetism. As this example shows, both geochemistry and paleomagnetism are required to separate the units studied here.

It should be noted that within the Black Canyon unit, a dacite intercalated (and not intruded) amongst 11 basalts, while visually and geochemically distinguishable, shares the same unusual remanence direction (see section 3.4). Accordingly it could be separated as a distinct stratigraphic unit. Due to its localized nature and contemporaneity with flows above and below based on remanence, we refrain from doing so.

Another important result is the separation of the Coso Basin andesite (previously dubbed Basalt of Coso Basin by Whitmarsh, 1996) from any other unit sampled, using both geochemistry and paleomagnetic remanence direction. Field evidence also suggests that the only surficial locality of this eruptive unit is also the source region (local dikes and intrusions of the same polarity are found at the locality).

In addition, geochemistry suggests correlation of lavas penetrated at 1300' and 1000' below grade by drill hole 35-2 (Figure 3.7) with Black Canyon flows and Petroglyph Canyon basalt respectively. This tentative correlation is discussed further, below.

In the Renegade Canyon area we analyzed lavas designated Basalt of Renegade Canyon (QTbr) and divided into subunits by Duffield and Bacon (1981). Figure 3.8 shows trace element data for lavas of this area, and refines the previous subunit definition geochemically, allowing widespread correlation of these units across the area. Most of these units are reversed polarity with very similar remanence directions and thus they are defined largely on the basis of geochemistry. Results from Renegade

Canyon suggest that the geochemistry of eruptive units there varies significantly within eruptive units and even within individual lava flows. For example, samples of QTbr<sub>8</sub> from a single locality and QTbr<sub>4</sub> from two different localities vary significantly. This introduces some uncertainty into correlations around the Renegade Canyon. Question marks enclosing QTbr<sub>1</sub> on Figure 3.8 indicate the uncertainty due to trace and major element geochemical variation as well as paleomagnetic results.

Major element and trace element geochemistry are plotted versus MgO on Figures 3.9-3.22 and strongly support units defined for Wild Horse Mesa lavas (Figure 3.7) by the tight grouping of data points within each eruptive unit. These data also support units QTbr<sub>2</sub> and QTbr<sub>4</sub> as defined (Figure 3.8). However, QTbr<sub>1</sub> is a questionable grouping because of the lack of paleomagnetic data and the spread on major element geochemistry for locality RC lava flow 3 and the bottom flows, compared to the QTbr<sub>1</sub> type locality. As will be shown in section 3.4 this uncertainty is immaterial because there appears to be no measurable relative rotation among localities of Renegade Canyon over the age of the lavas.

Results from major element analysis also call into question possible correlations of cuttings samples from drill hole 35-2 from which no paleomagnetic analyses are possible. These geochemical data, for the most part, fall far off the trend of data from all surface samples. The proximity of this drill hole to the geothermal area and the detection in nearby drillholes of geothermal waters suggests that the unusual geochemistry of these lavas results from hydrothermal alteration. Such alteration is known to strongly deplete samples of Mg at mid-ocean ridges. Therefore, while geothermal water appears to have depleted these units in Mg and probably other mobile major elements, we suggest that their trace element concentrations may be largely unperturbed. Furthermore, the ratio of trace elements analyzed would be even more stable because of their similar chemical behavior. Ergo, we retain correlation of the 1000' and 1300' samples of hole 35-2 with Petroglyph Canyon basalt and Black Canyon flows.

The lateral extent of major new or redefined units described here are depicted in map view in Appendix C.

### 3.4 Paleomagnetism

#### 3.4.1 Sedimentary Sections

Sedimentary localities offer the opportunity to measure vertical axis rotation relative to paleo-geographic north, i.e. absolute rotation. Figure 3.23 shows data for localities CWA and WHB. The dispersion of individual sample ChRMs about the mean is the result of secular variation of Earth's magnetic field plus any infidelity in remanence recording by the sediments.

Reliable data from the WHB (Figure 3.23A) are all of reversed polarity, consistent with previous age constraints placing it in the early Pleistocene (Duffield et al., 1980). The tilt-corrected mean direction of D (declination) = 175.5°, I (inclination) = -21.4° and  $\alpha_{95}$  (region that is 95% likely to enclose the true mean direction) = 10.1° for 13 independently oriented hand samples (N=13) is statistically indistinguishable from geographic south but is significantly shallowed in inclination. This shallowing from an expected mean inclination of -55.5° is likely due to two factors: 1) shallowing due to the tendency of magnetized tabular hematite, which is ordinarily magnetized in the plane of the grain, to lie flat. Hematite is the main remanence carrier in the most shallowed



samples. 2) post-sedimentation compaction as corroborated by a horizontally-foliated fabric in anisotropy of magnetic susceptibility measurements of these sediments.

The CWA section is entirely normal polarity, consistent with the inferred age of Coso Wash fanglomerate of around 3 Ma (Duffield et al., 1980). Figure 3.23b depicts ChRMs for independently-oriented fanglomerate samples, a mean ChRM for multiple specimens from an oriented hand sample of pyroclastics immediately beneath the dacite and the mean direction of the capping dacite based on four independently-oriented (and averaged prior to inclusion into a locality mean) drill core. We apply two possible tilt corrections in Figure 3.23B, restoring the fanglomerate to original dips of  $10^\circ$  or  $5^\circ$ . We err on the conservative side (less correction) and choose the former as the best tilt correction. The proximity of Mesozoic basement suggests the Pliocene mountain front producing this fanglomerate was similarly proximal and thus the steep original dip is warranted.

Thus, the CWA locality mean direction is  $D = 21.6^\circ$ ,  $I = 62.1^\circ$ ,  $\alpha_{95} = 5.0^\circ$  for  $N = 16$ , having been corrected from a bedding attitude of strike =  $050^\circ$  dip =  $20^\circ$  to original dip of strike =  $050^\circ$  dip =  $10^\circ$  (strike given as azimuth clockwise from north such that the dip direction is to the right; right-hand rule). This indicates  $21.6^\circ \pm 8.6^\circ$  clockwise vertical-axis rotation (method of Demarest, 1983) of the fault block on which these sediments lie. We expect these sediments to average secular variation because the thickness spanned (12m) contains evidence of many separate depositional events each being a few tens of centimeters thick. As previously stated, the fanglomerate is separated from the overlying pyroclastics and dacite by an angular unconformity. Given that both parts of the section are of similar age, we lump them together in determination of locality mean direction. Separation of the two parts of the section results in an even larger vertical axis rotation for the fanglomerate.

### 3.4.2 Lava Localities

We sampled 22 localities of basalts, andesites, and dacites of the Wild Horse Mesa spanning ages of 1.4 – 3.6 Ma (see Geochronology section). Of this group several were composed of many separate lava flows with up to 21 flows represented. The hallmark of these thick sections however, is the repetition of remanence directions and geochemistry for many flows within stratigraphically bounded zones. These have been interpreted to be single eruptive units, emplaced in a short span of decades or less time. As many as 19 flows are observed to compose a single eruptive unit (HS locality, Figure 3.24), usually where the flows pile up at a break in paleo-slope, within paleovalleys, or near the eruptive source for vents located on low paleoslopes. This results in only one or a few remanence directions being represented at any given locality. Therefore, averaging secular variation is very difficult for the lavas of this region. To sufficiently average secular variation, a combination of data from many localities would be necessary, and the resulting loss of spatial resolution might mean lumping rotated with unrotated blocks. For these reasons comparison of remanence directions of individual eruptive units between localities yields more information about the tectonics of the region.

Data in Figure 3.24 and 3.25 illustrate the previous points. Depicted are flow mean ChRMs on one stereonet for each sampling locality or eruptive unit. For example, the HS locality spans nineteen lava flows but the mean flow directions of these nineteen are statistically indistinguishable, indicating eruption in a period shorter than that necessary for significant secular variation, about two centuries. Even at PC, the locality

representing the most eruptive units (four), this is insufficient to average secular variation. Only the AL locality, exhibiting seven distinct remanence directions within the Coso Basin andesite unit, may sufficiently average secular variation.

Without the possibility of averaging secular variation, we use the spatial extent of eruptive units and the high precision with which their remanence direction can be measured to detect differences in remanence. Figure 3.26 shows comparisons between localities of unit mean ChRMs of eruptive units shared in common. Figure 3.26a depicts mean ChRM by locality of Petroglyph Canyon basalt and Black Canyon flows for localities BC, PC, LDC, UDC, FS. In the geographic reference frame (without tilt correction) locality ChRMs for new Basalt of Petroglyph Canyon are mostly statistically indistinguishable at 95% confidence while remanence directions from Black Canyon flows at two of these localities are indistinguishable when confidence levels are raised to 98%. On the other hand with tilt corrections applied (the largest being only  $10^\circ$ ), within-unit directions diverge, indicating that at least part of the tilt of lava flow tops results from original dips at the time of emplacement. Therefore, if we retain the directions with no tilt correction and assume that some of these flow-top attitudes stem from original emplacement on slopes, there is no relative vertical axis rotation of these 5 localities relative to one another. Thus if one locality has experienced rotation, all must have.

Figure 3.26b shows data from the Cole Flat basalt found at the CF and FS localities. In geographic and tilt-corrected coordinates there is a declination difference between locality mean directions. In geographic coordinates FS is rotated  $11.6^\circ \pm 6.9^\circ$  (method of Demarest, 1983) clockwise about a vertical axis relative to CF, while tilt-corrected this rotation is  $12.0^\circ \pm 7.0^\circ$  (with a misfit of inclination as well). As will be shown later, this suggestion that FS has rotated with respect to a "fixed" CF makes most sense. Remanence data from Silver Peak basalt, which crops out at SP and PC localities, are depicted in Figure 3.26c. PC is clockwise rotated about a vertical axis relative to SP  $12.3^\circ \pm 6.2^\circ$  (geographic) or  $13.0^\circ \pm 6.2^\circ$  (tilt-corrected).

To summarize, using Cole Flat basalt we measure  $11.6^\circ$  clockwise vertical-axis rotation of FS relative to CF locality. Using Petroglyph Canyon basalt, FS is unrotated relative to PC (as well as relative to BC, UDC, and LDC). Using Silver Peak basalt, PC is  $12.3^\circ$  clockwise rotated, about a vertical axis, relative to SP locality. Thus, we have two corroborative measures, in sense and magnitude, of clockwise relative rotation of five Wild Horse Mesa localities relative to two at its margins.

The CHS locality, on a mountaintop just southwest of Coso Hot Springs, is composed of poorly-preserved outcrop of Black Canyon flows. This locality is on the west side of the Coso Wash fault zone and thus perhaps in a separate tectonic domain from the Wild Horse Mesa and Coso Wash. Further west there is abundant evidence of down to the west tilting and Whitmarsh et al., (1996) found no net vertical-axis rotation since the Cretaceous. Figure 3.26d depicts mean unit ChRMs from all localities containing Black Canyon flows. There is no available tilt correction for CHS because of poor preservation. However, it is clear from the difference in mean locality ChRM for CHS that some tilt correction is required. Therefore, we use the directional difference between CHS and Black Canyon flows at BC to determine the tilt of the fault block on which the former locality sits. Given the ChRM for CHS presented here it makes little difference whether CHS and BC have both rotated about a vertical axis, or only BC has. In either case the tilt required to restore directional correspondence is about  $30^\circ \pm 5^\circ$  about an axis with azimuth of  $132^\circ$  and a plunge of between  $15^\circ$  and  $33^\circ$ . The presence of tilt at this locality is the significant thing, whereas the amount of tilt, tilt axis, and

discerning whether BC rotated about a vertical axis independently of CHS is uncertain due to the poor preservation of outcrop at CHS. Unlike all other lava localities described in this report, CHS specimen ChRMs exhibited a large dispersion. The small  $\alpha_{95}$  is possible for the site because of a large number of samples collected ( $N=35$ ), with rejection of a few samples exhibiting ChRMs suggesting out-of-place blocks on the outcrop scale. Therefore, accuracy of the precise locality direction is compromised. In short CHS is clearly tilted down to the west, by anywhere from  $30^\circ$  to  $50^\circ$  (the latter magnitude if a few samples are rejected)

In the area around Haiwee Spring, we have sampled three localities of Haiwee Spring basalt (localities HS, HSB, and HSD). Figure 3.26e presents the data, but neither the geographic nor simplistic tilt-corrected coordinates result in correspondence in directions for these localities. For this to be evidence of relative vertical-axis rotation they must at least exhibit similar inclinations. This is only the case for HS and HSD in the uncorrected case.

There are several possible explanations for this. It is possible that although geochemically the same, these flows may record different times in Earth's secular variation in magnetic field. This is improbable because of the thickness of the unit (nineteen flows at HS), close proximity of the localities and the absence of remanence variation within a locality. These all suggest rapid voluminous eruption that simultaneously covered the small vicinity of these localities. It is possible that unaccounted-for original dips cause part of the mismatch with the additional possibility of relative rotation of localities. For example, simplistic tilt-correction of HS and correction of HSB to an original dip of about  $10^\circ$  southwards results in equivalent inclinations and a clockwise rotation of HSB relative to HS. The number of degrees of freedom on such solutions is infinite – one must solve for original dip of each pair of localities plus relative vertical-axis rotation between them given the hard constraint of the remanence directions and the guideline of flow "attitudes". More information about the flow direction from knowledge of the eruptive source would help in constraining the solution. In short Haiwee Spring localities suggest original dips and perhaps relative vertical-axis rotation, but a quantitative measure is premature pending additional data.

Coso Basin andesites first recognized by Whitmarsh (1996) to be Pliocene (map unit Tbb "basalt" of Coso Basin,  $3.58 \pm 0.86$  Ma) in age are the only lavas in the field area having any possibility of yielding an absolute rotation through averaging of secular variation. Along the Coso Wash fault zone, the AL locality, 1.5 km north of Airport Lake's western end, contains 5 flows, a dike, and a sill (Figure 3.26f) each recording a different remanence direction. The flows have been tilted to the west back toward the presumed eruptive source, a near-surface intrusive body of andesite. When tilt-corrected to yield an assumed original dip of  $10^\circ$  to the southeast the locality yields a mean remanence direction indistinguishable from geographic south though somewhat shallow. The shallow inclination indicates that either the tilt correction is inappropriate or that secular variation was not fully averaged out.

Several Plio-pleistocene lavas indicate no relative rotation between the localities where they occur. These negative results constrain the spatial pattern or timing of vertical-axis rotation and tilting in the study area. Duffield and Bacon (1981) mapped Basalt of Renegade Canyon and subdivided it into multiple subunits, QTbr<sub>1</sub>-QTbr<sub>8</sub>. We have sampled QTbr<sub>2</sub> and QTbr<sub>4</sub> at two localities each and found no statistically distinguishable directional difference within each pair of directions (Figures 3.26g, h).



Either differential rotation between these localities has been insufficient during the period measured for each subunit or no differential rotation has occurred in this region. Note that QTbr<sub>2</sub> at the Renegade Canyon locality exhibits two distinct directions for different distal lava flows. This suggests either a sampling error, that secular variation was very fast during their emplacement or that long hiatuses occurred between emplacement of the two flows.

We sampled Basalt of Coso Wash (localities CMA and CMC from Qbc, Duffield and Bacon, 1981), in order to place constraints on the differential tilting rate across the Coso Wash fault zone. Four kilometers north of this unit is the Coso Hot Spring/Black Canyon locality pair with its 30°-50° differential tilt since 3.4 Ma. Two kilometers south is the Airport Lake andesite which has tilted 10°-20° since 3.6 Ma. We sampled Qbc (dated at 1.1 Ma by Duffield et al, 1980, ca. 0.97 Ma according to our geochronology) with the intent of measuring some intermediate amount of relative tilt across the Coso Wash fault zone. We found no tilt (or vertical-axis rotation) within an uncertainty of only a few degrees. This constrains initiation of tilting on the Coso Wash to have predated 1 Ma. Otherwise a relative tilt would probably be observed between localities CMA and CMC

### 3.5 Geochronology

A summary of our geochronologic data is presented in Table 3.1. Two of the analyses provided poor results because of the character of the lavas. The remainder of lavas sampled yielded satisfactory and sometimes unexpected results. For example, a sample from RC locality which correlates paleomagnetically and geochemically with QTbr<sub>2</sub> was determined to be  $1.37 \pm 0.04$  Ma, while Duffield et al (1980) assigned an age of  $1.75 \pm 0.1$  Ma based on K/Ar dating on samples from locality RCE. In addition <sup>40</sup>Ar/<sup>39</sup>Ar geochronology from the base of RC locality yielded an age of about 2.6 Ma, substantially older than the other radiometric constraints for rocks around Renegade Canyon. Remaining geochronologic determinations are of good quality and yielded ages similar to those expected.

The most significant result of our new geochronologic data is that they suggest that eruption of Wild Horse Mesa lavas spanned a shorter period than previously thought. Duffield et al. (1980) considered these eruptions to have spanned 3-4 Ma, though they acknowledge most eruptions postdated 3.7 Ma. Some of their K/Ar dating included ages older than 4 Ma (e.g. their localities numbered 38 and 47). Our combined geochronology and stratigraphic constraints show that eruptions in the Wild Horse Mesa began around 3.6 Ma and were largely completed by 3.0 Ma (Figure 3.27), when volcanic activity shifted to the Haiwee Reservoir area. Whereas Wild Horse Mesa volcanics were voluminous and of a "short" duration, volcanic activity in the Renegade Canyon area was of smaller volume and much more distributed in time, spanning 2.6 to 1.4 Ma. The short-duration, voluminous Wild Horse Mesa volcanics suggest relationship with regional extensive volcanism from around the same period, now being attributed to foundering of an eclogite root from beneath the Sierra Nevada (Manley et al., 2000).

### 4.0 Discussion

The Pliocene lavas and sediments sampled in Wild Horse Mesa and Coso Wash all indicate clockwise vertical-axis rotation of the fault-bounded blocks sampled. The Coso Wash fanglomerate locality reveals absolute rotation relative to paleo-geographic north. The five Wild Horse Mesa lava localities (BC, PC, LDC, UDC, and FS) are little changed

relative to one another but clockwise rotated relative to CF and SP. The uncertainties on the measurements presented here are not small enough to discern whether there is spatial variability in clockwise rotation within the clockwise-rotated region.

Figure 4.1 shows a simplified map of the geometry of rotated blocks relative to boundaries of the rotating region. The geometry of the rotating region is more complex than models for block rotation usually presented in the scientific literature (e.g., Luyendyk, 1991; Nur et al., 1993, Unruh et al. 1996), because the boundaries of the rotating zone are not parallel. These boundaries are the Coso Wash (normal) fault zone and the herein defined Wild Horse Mesa fault zone. The geometry of this latter structure is estimated using (1) the geometry of mapped fault traces, (2) the edge of mapped Mesozoic basement of the Cole Flat area, and (3) the fact that this feature separates a domain of vertical-axis rotation from a larger domain that has not experienced similar rotation to the east (Schweig, 1989; Ron and Nur, 1996). As defined above it appears as a right-stepping, northwest-striking string of faults nearly optimally oriented to accomodate regional dextral shear. In fact, the M 5.2, March 1998 earthquake occurred sub-parallel to and nearby this structure.

We hypothesize that block rotation at the near-surface at Wild Horse Mesa and Coso Wash accommodates regional dextral shearing. Block long-axes are oriented between due north and N20°E while geodetically-determined dextral motion across the Eastern California shear zone at this latitude (Airport Lake fault zone) is oriented at about N40°W (McClusky et al., 2001). Similarly, the geodetically-determined azimuth of motion of the Sierra Nevada microplate relative to stable North America is N43°W at this latitude (Dixon et al. 2000). Consequently, fault-bounded blocks of the Wild Horse Mesa are oriented more favorably for accomodating the regional shear by rotation than either pure dextral slip or pure dip-slip on the faults between them (e.g., Dewey 2002).

The orientation of the Wild Horse Mesa and Coso Wash fault zones and the fact that these boundaries are not parallel requires net thinning in between as part of the regional dextral shearing. Early pinned block models of rotation required opening perpendicular to the parallel basin bounding faults during transtension (e.g. Luyendyk, 1991). At Wild Horse Mesa opening of the basin is accomplished passively by the basin geometry. Furthermore, in pinned block models finite rotation requires oblique slip with either a component of normal or reverse faulting between blocks, depending upon the geometry. In the Wild Horse Mesa only dip-slip offsets are apparent because of the lack of horizontal offset markers. This crustal thinning, as demonstrated by inverse modeling of seismogenic strain at shallow crustal levels (Figure 3.1), is therefore compatible with vertical axis rotation. Moreover, the outcrop-scale brittle faults exposed on Wild Horse Mesa record components of crustal thinning and horizontal shearing, both of which are characterized by subhorizontal, west southwest-east northeast maximum stretching ( $d_1$ ). These strain geometries are consistent with the seismogenic strain geometries as well as expectations of transtension in the regional-scale right releasing step in the dextral faults that mark the eastern California shear zone in this area (e.g., Figure 2.1, and Unruh et al. 2002). Therefore, these data present a unified picture of kinematic behavior of the Wild Horse Mesa.

Block models are useful simplifications because they permit calculation of the minimum total dextral slip necessary to produce the observed rotations. Across such a region, more direct measurements of displacement are often impossible. Figure 4.2 depicts such a calculation of minimum dextral slip on the basin-bounding faults for the observed rotations, assuming blocks pinned to the boundary faults. Typically, such calculations require block length, width and orientation relative to strike-slip boundary

faults. Assuming that the blocks are much longer than they are wide, which is consistent with the mapped fault traces, the exact width of the blocks becomes less important to this calculation. This is especially so in the Wild Horse Mesa case because normal faulting results in apparent widening of blocks in map view as block footwalls are exhumed across inclined faults. In addition, we allow the blocks to deform internally by slip on faults of the type examined in this study (i.e., we treat the shallow crust as a micropolar continuum). This view is supported by the fact that closely-spaced outcrop-scale faults have accommodated crustal thinning, horizontal shearing and crustal thickening. Using an estimated block length of 10 km obtained by using crust bounded by only the largest normal faults in the study area, we calculate a minimum dextral offset of 1.5 km along the Wild Horse Mesa basin-bounding fault zone. The calculated minimum offset is easily achievable given the current geodetically-determined slip rates across the basin of 5.3 mm/yr (the rate of Airport Lake fault zone, McClusky et al., 2001). The total minimum offset is accounted for in only a few hundred thousand years, given this as a steady rate, despite current understanding that dextral shear initiated in the region as recently as ca. 2 Ma (Monastero et al. 2002). This implies additional slip not accounted for in our calculation arising either from unpinning the rotated blocks or from other structures outside the Wild Horse Mesa.

It is important to understand that rotating blocks of Wild Horse Mesa are an upper-crustal feature probably riding above one or a few dextral master faults at depth, as indicated by the differing character of seismogenic strain with depth. In addition, significant complexity is not accounted for in the model, such as the possibility of curved faults, varying tilt magnitude on different blocks and block rotation in the area west of Coso Wash fault zone. Nonetheless, our block model is instructive and retains the most important features of the study area.

Within the Wild Horse Mesa, field observations indicate that some fault-bounded blocks have tilted. In particular some lava flow tops, which parallel the ground surface across most of the area, display substantial topographic slopes. Adjacent blocks tilt in different directions and back toward eruptive sources from which lavas emanated in some cases. Our sampling localities have inadvertently avoided such blocks for the most part. The little tilt present at PC, BC, UDC, and FS can be attributed to original dip of the lavas as they were emplaced on a paleoslope, as supported by the correspondence of remanence directions for these localities despite the apparent tilt. This is a common phenomenon in other studies. In the case of the three Haiwee Springs localities (HS, HSB, HSD), correction for large tilts results in great discrepancies in remanence direction within a single eruptive unit. This is probably best attributed to steep original dips coupled with differential rotation between localities. We suggest that the tilting of fault blocks in the Wild Horse Mesa is not a significant feature. For example the tilts in opposite directions (some east, some west) in southern Wild Horse Mesa suggest a net canceling out of at least some this horizontal axis rotation in that region. Our paleomagnetic sampling of large stable blocks within the mesa indicates little net tilt. Sandbox modeling (Dooley and McClay, 1997) of step overs in strike slip fault systems supports this and indicates that net vertical-axis rotation is the more significant and regional feature.

However tilt on the west side of the Coso Wash fault zone appears to be generally down to the northwest. Coso formation between Haiwee Reservoir and the geothermal field is mostly tilted in this sense. Paleomagnetic data from CHS and lava flow attitudes from AL and HSD indicate large tilts of 20° to 35° or more along the west side

of the Coso Wash fault zone. Whitmarsh et al. (1996) suggested similar tilting of  $30^\circ$  or more near Rose Valley since the Cretaceous. Altogether this indicates widespread tilting down to the northwest of Mesozoic basement blocks between the Coso Wash fault zone and Rose Valley/Haiwee Reservoir. Whether vertical axis rotation has occurred in this region is still debatable though Whitmarsh's unpublished data are to the contrary.

## 5.0 Conclusion

The Wild Horse Mesa exhibits  $12.0^\circ \pm 4.6^\circ$  to  $21.6^\circ \pm 10.7^\circ$  of clockwise vertical-axis rotation since about 3 Ma of fault bounded blocks as demonstrated paleomagnetically. Abundant, probably oblique sinistral-normal, north-northeast striking faults accommodate block rotation near the surface between the left-stepping Coso Wash normal fault zone and the newly-defined, right-stepping, dextral Wild Horse Mesa fault zone. Clockwise block rotation is consistent with our results of inverse modeling of fault slip data. Moreover, statistically-significant relative vorticity is suggested by our inverse modeling of earthquakes from 5-8 km at Wild Horse Mesa (Figure 3.2). Given the predominance of regional right slip, and the fact that the earthquake hypocenters define a northwest striking seismic source zone, the sense of block rotation for these seismic events is interpreted to be clockwise. Absolute vertical axis rotations of  $12^\circ$  yield a minimum dextral offset across the Wild Horse Mesa of 1.5 km along a strike of  $N30^\circ W$ , subparallel to the Wild Horse Mesa fault zone.

The dextral fault(s) at depth merge with or step over to the Airport Lake fault zone to the south. We suggest that to the north this strike-slip fault steps across Upper Centennial Flat to Lower Centennial Flat and the east side of Owens Lake where subsurface faults have been mapped by seismic reflection (Neponset Geophysical and Aquila Geosciences, 1997). This semi-continuous structure is one strand of the Eastern California shear zone linking the Owens Valley fault zone with the Airport Lake fault zone, and ultimately with structures south of the Garlock fault. The Mesozoic basement high to the west of this localized strand of the Eastern California shear zone is tilted as many separate blocks to the northwest. This tilting could be the result of upper plate disruption above a master Sierra Nevada frontal or other fault zone (e.g., Monastero 1997). Alternatively, a through-going structure may not be necessary or even possible beneath the geothermal field since the magma chamber there probably accommodates extension.

In summary we have shown that careful mapping and geochemical fingerprinting of lava flows, in conjunction with paleomagnetic analyses and radiometric dating, provide important constraints on volcano-stratigraphy. These constraints have been integrated with analyses of contemporary non-recoverable strain (i.e., earthquakes) and time-integrated non-recoverable strain (i.e., exposed faults), to derive a better understanding of the kinematic evolution of the Wild Horse Mesa and adjoining Coso geothermal field. The result is (1) a conceptual model for the geometry of some of the major structures that accommodate transtension in the region, and (2) an estimate of the magnitude of slip required to account for the observed finite rotations of crustal blocks, the geometry of contemporary strain and the geometry of long-term fault-related strain.

## Tables

Table 1.1 Activity Summary By Task

Task	Description	Activity during quarter (yes/no)
1	Inversion/evaluation of earthquake data	No
2	Micropolar inversion of field-measured fault data	Yes
3	Radiometric/Paleomagnetic analyses	Yes
4	Integration and interpretation	Yes

Table 2.1 Field-measured shear plane/slip data from Wild Horse Mesa.

Location on Mesa <sup>†</sup>	Shear plane Strike	Shear plane Dip	Lineation Trend	Lineation Plunge	Slip Sense <sup>‡</sup>	Data quality poor = c <sup>†</sup>	Station <sup>†</sup>
I	333	64	118	55	2		
I	162	75	167.1	18.3	4		
I	271	76	269	5	6		
I	325	20	328	10	6		
I	13	55	22	22	8		
I	309	74	131	22	4		
I	239	76	260	56	6		
I	207	77	311	70	8		8
I	135	65	288.3	44	8		8
I	333	63	130	45	2		8
I	18	60	159	47	2		8
I	225	70	349	66.3	2		8
I	223	71	4.1	61.2	2		8
I	181	80	183.3	12.8	6		
I	263	62	16	57	2		
I	28	83	55.8	75.3	2		
I	66	76	93.4	61.6	2		
I	269	76	41	72	8		
I	129	64	229	62	8		
I	1	57	91	57	8		
I	149	42	226	41	8		
I	35	57	171.7	46.6	2		
I	31	33	56	14	8		
I	315	67	349.1	52.9	8		
I	66	37	162	36	8		
I	146	82	322	25	4		
I	188	86	350	62	8		
I	188	86	5	33	4		
I	38	19	55	11	6		
I	173	83	342	55	8		
I	140	48	157	27	8		
I	0	74	173	30	4		
I	35	41	120	38	8		
I	55	47	223	13	2		
I	160	88	339.1	25	4		
I	270	69	354.4	68.9	8		
I	77	82	227.8	73.9	2		
I	351	88	169	45	8		
I	131	75	145	51	2		
I	333	52	345.6	15.6	4		
I	240	86	240.7	10	4		
I	196	9	349	6	2		
I	157	81	172.2	58.8	2		
I	305	50	310	7	4		



l	63	83	239	29.8	6		
u	354	87	126	86	2	c	
u	180	78	215	68	2	c	
u	91	86	181	86	2		203
u	91	86	114.8	80.2	2		203
u	91	86	98.2	60.7	2		203
u	84	84	88	33.8	2		203
u	274	82	93	6.9	6		203
u	96	69	268	20	6		203
u	96	69	103	18	6		203
u	286	80	61.4	75.9	8		203
u	333	83	151.8	9.9	4		203
u	333	83	334.1	8.9	6		203
u	287	67	97	22	2		203
u	273	63	82	22	2		203
u	273	90	93	12	6		203
u	118	88	118	12	6		203
u	346	80	163	16	4		203
u	347	78	167	17	4		203
u	329	76	147	6	4		203
u	104	90	104	3	6		203
u	335	72	157	5	4		203
u	334	73	156	8	6		203
u	340	73	345	15	4		203
u	284	64	98	11	6		203
u	251	78	69	10	4		203
u	180	79	181	3	4		
u	282	70	99	8	6		
u	320	84	140	3	4		
u	342	65	343	2	6	c	
u	339	86	339	1	6	c	
u	75	70	81	15	6		
u	352	88	171	11	4		
u	229	56	22	37	2	c	
u	328	79	33.4	77.9	2		
u	161	87	337	52	6	c	
u	347	36	27	26	2		
u	125	81	285	64	2		
u	133	59	215	58	2		
u	309	64	49	64	2		
u	105	72	280.3	14.2	6		
u	14	77	58	71	2		
u	2	72	57	64	2		213
u	61	30	151	32	8		213
u	47	34	149	34	8		213
u	8	24	159	12	8		213
u	64	38	167	36	8		213
u	18	53	162	38	8		213

u	232	75	282.6	70.9	2	213
u	35	73	138.5	72.5	8	213
u	19	30	118.2	29.7	8	213
u	6	88	156	86	8	213
u	349	32	67	30	8	213
u	50	66	178.6	60.3	8	213
u	255	69	336.7	68.8	8	213
u	45	77	49	16	4	
u	300	74	12.39	73.26	2	
u	2	80	34	72	2	
u	149	43	326	4	2	
u	2	82	48	79	2	

\* lower Wild Horse Mesa, u=upper Wild Horse Mesa

\* normal, 4=left lateral, 6=right lateral, 8=thrust

\* "a" and "b" quality not differentiated, see text for discussion of use of "c" quality data

† coordinates of indicated stations as follows:

Station	UTM north	UTM east	Latitude north	Longitude
8	3983794.67	436553.29	35.99834361	242.2960767
203	3986485.61	440389.67	36.02284611	242.3384353
213	3987168.24	439215.46	36.02892778	242.3253519

Table 2.2 - X-ray Fluorescence Geochemical Analyses

Eruptive Unit		Haiwee Springs Basalt										Silver Peak Basalt			
Locality /Flow #	HS Flow 1	HS Flow 10	HS Flow 18	HSB Flow 1	HSB Flow 7	HSD Flow 1		SP Flow 1	SP flow "2"	PC Flow 21					
Sample ID	Mean	Mean	Mean	Mean	Mean	Mean	Mean	Mean	Mean	Mean	Mean	Mean			
HS0107A	54.01	53.75	54.02	53.96	53.86	53.98	54.27	49.30	49.36	50.31	49.97				
SiO <sub>2</sub>	0.12	0.11	0.16	0.06	0.29	0.10	0.10	0.13	0.01	0.14	0.07				
standard dev.	1.57	1.50	1.38	1.48	1.56	1.54	1.50	1.49	1.37	1.35	1.33				
TiO <sub>2</sub>	0.002	0.005	0.001	0.006	0.010	0.010	0.001	0.017	0.006	0.011	0.001				
standard dev.	17.52	17.33	16.86	17.40	17.24	17.55	17.18	16.33	16.43	16.60	17.01				
Al <sub>2</sub> O <sub>3</sub>	0.12	0.02	0.02	0.19	0.21	0.10	0.07	0.15	0.04	0.17	0.09				
standard dev.	8.11	8.00	7.68	7.76	8.19	8.00	7.80	10.48	10.23	9.88	9.76				
Fe <sub>2</sub> O <sub>3</sub>	0.02	0.11	0.12	0.02	0.04	0.07	0.21	0.06	0.04	0.13	0.11				
standard dev.	0.13	0.13	0.13	0.13	0.13	0.12	0.13	0.17	0.16	0.16	0.15				
MnO	0.000	0.002	0.001	0.001	0.000	0.001	0.001	0.003	0.000	0.001	0.001				
standard dev.	4.88	5.45	5.87	5.41	5.23	4.39	4.97	7.90	7.91	7.96	7.67				
MgO	0.01	0.02	0.03	0.01	0.05	0.05	0.04	0.15	0.01	0.06	0.08				
standard dev.	7.77	7.90	8.37	8.06	7.67	8.47	8.56	9.93	10.27	9.49	9.74				
CaO	0.02	0.02	0.01	0.05	0.02	0.02	0.02	0.03	0.02	0.02	0.00				
standard dev.	4.14	4.13	3.95	4.02	4.22	4.10	3.85	3.53	3.42	3.36	3.48				
Na <sub>2</sub> O	0.01	0.01	0.03	0.04	0.01	0.04	0.03	0.06	0.02	0.05	0.04				
standard dev.	1.48	1.44	1.35	1.40	1.50	1.42	1.36	0.58	0.56	0.62	0.62				
K <sub>2</sub> O	0.003	0.006	0.008	0.005	0.017	0.003	0.011	0.003	0.000	0.005	0.000				
standard dev.	0.40	0.38	0.39	0.39	0.41	0.44	0.38	0.29	0.30	0.27	0.26				
P <sub>2</sub> O <sub>5</sub>	0.001	0.007	0.000	0.000	0.007	0.000	0.001	0.021	0.003	0.008	0.011				
standard dev.	0.50	0.46	0.28	0.65	0.24	1.61	1.49	0.01	0.39	0 (-0.345)	0 (-0.04)				
volatiles (LOI)															
Nb	13.13	12.63	12.01	12.92	12.97	13.09	12.87	8.88	8.76	9.14	8.73				
standard dev.	0.39	0.47	0.17	0.08	0.28	0.14	0.11	0.46	0.04	0.24	0.32				
Zr	242.81	229.46	207.93	225.90	245.35	231.66	227.84	150.33	145.83	151.71	150.15				
standard dev.	0.18	0.44	1.14	1.63	2.25	0.41	1.44	1.29	0.16	2.30	1.30				
Y	28.48	27.26	25.20	26.48	28.57	27.82	28.36	28.76	27.34	26.29	26.61				
standard dev.	0.15	0.09	0.64	0.59	0.58	0.25	0.34	0.45	0.03	0.36	0.12				
Sr	648.82	636.66	642.54	629.31	641.02	663.18	659.32	424.70	433.94	455.22	467.37				
standard dev.	0.89	3.29	2.34	1.27	5.58	2.88	5.95	4.14	2.45	6.26	4.14				
Rb	24.69	24.14	21.81	22.71	26.18	23.55	21.36	6.59	6.90	7.69	6.97				
standard dev.	0.61	0.34	0.65	0.09	0.19	0.25	0.33	0.85	0.21	0.52	0.96				

Values shown are percentages for SiO<sub>2</sub> through volatiles and parts per million for Nb through Rb. Standard deviations result from comparison of duplicate samples and refers to the data row just above it. Negative values in parentheses for volatiles indicates absorption during heating, i.e. initially zero.

Table 2.2 (cont.) - X-ray Fluorescence Geochemical Analyses

Eruptive Unit/ Locality /Flow #	Cole Flat Basalt				Tdo		Drill Hole 35-2						LB Flow 1
	FS Flow 6	FS Flow 8	FS Flow 12	CF Site 3	CWA top flow		Mean 35-2 180' *	Mean 35-2 380' *	Mean 35-2 800' *	Mean 35-2 1000' *	Mean 35-2 1300' *	Mean LB01	
Sample ID	Mean BD0603A	Mean BD0802B	Mean BD1202B	Mean CF0303A	Mean Tdo0102A								
SiO <sub>2</sub>	51.72	51.55	51.38	50.75	60.01		56.62	63.77	51.27	52.07	53.67	54.96	
standard dev.	0.29	0.16	0.17	0.04	0.18		0.14	0.16	0.74	0.05	0.12	0.06	
TiO <sub>2</sub>	1.50	1.56	1.48	1.48	0.79		1.25	0.77	1.38	1.70	1.37	1.16	
standard dev.	0.005	0.006	0.001	0.001	0.008		0.004	0.005	0.015	0.012	0.004	0.016	
Al <sub>2</sub> O <sub>3</sub>	16.41	16.38	16.60	16.46	15.65		15.96	15.70	16.60	18.02	18.28	17.98	
standard dev.	0.02	0.19	0.30	0.05	0.03		0.15	0.12	0.11	0.01	0.03	0.36	
Fe <sub>2</sub> O <sub>3</sub>	9.05	9.40	8.89	9.22	5.74		7.78	4.91	10.80	9.95	9.63	7.13	
standard dev.	0.15	0.02	0.01	0.06	0.14		0.02	0.02	0.18	0.07	0.05	0.23	
MnO	0.15	0.15	0.15	0.15	0.08		0.11	0.06	0.10	0.09	0.07	0.10	
standard dev.	0.001	0.001	0.000	0.000	0.001		0.001	0.000	0.002	0.000	0.000	0.003	
MgO	7.33	6.96	7.32	7.08	5.25		4.80	2.66	3.88	3.59	2.81	4.76	
standard dev.	0.02	0.05	0.04	0.01	0.03		0.02	0.00	0.01	0.01	0.01	0.07	
CaO	9.13	9.30	9.58	10.14	6.05		6.75	4.24	11.58	9.20	8.56	7.62	
standard dev.	0.06	0.06	0.03	0.00	0.10		0.00	0.02	0.62	0.03	0.01	0.02	
Na <sub>2</sub> O	3.63	3.57	3.59	3.63	3.77		4.25	4.47	3.13	3.74	3.72	4.34	
standard dev.	0.06	0.01	0.08	0.02	0.00		0.02	0.01	0.01	0.03	0.00	0.00	
K <sub>2</sub> O	0.80	0.83	0.73	0.78	2.46		2.13	3.20	0.86	1.19	1.51	1.67	
standard dev.	0.012	0.003	0.002	0.003	0.004		0.000	0.004	0.010	0.004	0.003	0.010	
P <sub>2</sub> O <sub>5</sub>	0.29	0.30	0.28	0.31	0.20		0.34	0.20	0.40	0.44	0.38	0.28	
standard dev.	0.001	0.002	0.006	0.003	0.000		0.005	0.010	0.005	0.013	0.005	0.011	
volatiles (LOI)	0 (-0.16)	0.67	0.64	0.90	0.80		1.42	1.44	3.86	3.43	3.62	0.65	
Nb	9.57	9.51	8.98	9.65	9.52		17.19	11.87	9.42	11.92	11.29	8.94	
standard dev.	0.02	0.33	0.44	0.48	0.16		0.33	0.22	0.12	0.41	0.01	0.30	
Zr	176.55	177.87	163.94	170.81	163.00		197.16	182.34	159.24	194.59	185.70	142.17	
standard dev.	1.30	0.68	0.16	2.18	0.14		0.93	2.53	2.33	0.72	1.86	0.11	
Y	26.82	27.44	25.66	26.35	16.17		21.02	16.05	25.12	27.32	25.42	19.62	
standard dev.	0.18	0.26	0.11	0.53	0.57		0.54	0.55	0.60	0.18	0.73	0.71	
Sr	546.12	542.24	539.90	556.54	650.77		625.81	611.64	746.52	771.71	741.79	707.93	
standard dev.	7.31	2.08	2.12	7.18	0.54		2.05	3.23	6.79	2.98	4.11	1.03	
Pb	10.94	13.10	10.33	10.85	46.48		42.90	67.90	17.85	14.60	24.54	29.80	
standard dev.	1.01	0.13	0.34	0.87	0.44		0.24	0.75	0.22	0.02	0.35	0.35	

Values shown are percentages for SiO<sub>2</sub> through volatiles and parts per million for Nb through Pb. Standard deviations result from comparison of duplicate samples and refers to the data row just above it. Negative values in parentheses for volatiles indicates absorption during heating. i.e. initially zero.

\* - These data may be problematic because 35-2 samples could be contaminated with material from the borehole sidewall.

Table 2.2 (cont.) - X-ray Fluorescence Geochemical Analyses

Eruptive Unit		Petroglyph Canyon Basalt																	
Locality /Flow #		PC Flow 22		BC Flow 6	DC Flow 2	DC Flow 1	UDC Flow 3		FS Flow 2		FS Flow 3	FS Flow 14		FS Flow 4					
Sample ID	Mean	Mean	Mean	Mean	Mean	Mean	Mean	Mean	Mean	Mean	Mean	Mean	Mean	Mean	Mean				
PC2206A	PC2208A	99BC0603A	OC0204A	OC0102A	UOC0301A	UOC0302A	BD0201C	BD0303B	BD1401C	BD0403B									
SiO <sub>2</sub>	49.02	49.51	50.19	50.68	49.93	49.83	50.05	49.57	50.05	49.52	49.94								
standard dev.	0.05	0.08	0.18	0.18	0.05	0.02	0.05	0.15	0.08	0.22	0.12								
TiO <sub>2</sub>	1.27	1.31	1.23	1.24	1.24	1.19	1.18	1.20	1.28	1.19	1.25								
standard dev.	0.005	0.002	0.000	0.001	0.000	0.005	0.000	0.001	0.002	0.010	0.005								
Al <sub>2</sub> O <sub>3</sub>	16.04	16.20	16.04	16.71	15.96	15.63	15.81	16.20	16.21	16.06	16.38								
standard dev.	0.14	0.11	0.30	0.21	0.10	0.04	0.00	0.13	0.02	0.16	0.06								
Fe <sub>2</sub> O <sub>3</sub>	9.46	9.62	9.55	9.49	10.16	10.44	9.86	9.79	9.61	9.76	9.39								
standard dev.	0.00	0.06	0.04	0.05	0.02	0.06	0.06	0.07	0.01	0.16	0.00								
MnO	0.16	0.16	0.15	0.15	0.16	0.16	0.16	0.16	0.16	0.16	0.15								
standard dev.	0.001	0.000	0.000	0.001	0.001	0.001	0.001	0.001	0.001	0.003	0.000								
MgO	8.41	8.13	8.51	7.45	8.17	8.43	9.15	8.89	8.56	8.33	8.51								
standard dev.	0.09	0.08	0.05	0.06	0.03	0.00	0.04	0.04	0.03	0.07	0.01								
CaO	10.96	10.70	10.05	10.06	10.31	10.31	9.79	9.99	9.85	10.77	10.10								
standard dev.	0.02	0.04	0.00	0.01	0.06	0.08	0.04	0.04	0.07	0.02	0.03								
Na <sub>2</sub> O	3.51	3.22	3.33	3.30	3.15	3.10	3.13	3.19	3.34	3.26	3.28								
standard dev.	0.08	0.00	0.02	0.03	0.05	0.02	0.01	0.03	0.16	0.11	0.02								
K <sub>2</sub> O	0.75	0.73	0.66	0.64	0.65	0.60	0.60	0.64	0.65	0.63	0.67								
standard dev.	0.004	0.006	0.003	0.001	0.002	0.004	0.001	0.005	0.009	0.003	0.001								
P <sub>2</sub> O <sub>5</sub>	0.43	0.42	0.30	0.28	0.29	0.31	0.27	0.37	0.29	0.31	0.33								
standard dev.	0.001	0.004	0.001	0.004	0.007	0.001	0.002	0.003	0.002	0.027	0.010								
volatiles (LOI)	0.64	3.36	0 (-0.03)	0.37	0.66	0.45	0 (-0.26)	0.61	0 (-0.33)	1.74	0.14								
Nb	9.68	10.06	8.08	7.43	7.02	9.08	6.78	8.11	8.25	8.11	8.40								
standard dev.	0.35	0.16	0.56	0.14	0.31	0.34	0.18	0.08	0.09	0.24	0.25								
Zr	150.98	156.95	138.34	144.59	134.03	177.29	129.59	138.19	138.97	135.12	142.39								
standard dev.	0.62	1.38	0.81	0.62	0.15	1.09	0.44	0.11	1.28	0.81	0.10								
Y	25.08	25.78	25.04	26.43	23.00	30.22	22.40	25.93	24.98	24.64	24.67								
standard dev.	0.42	0.58	0.73	0.64	0.47	0.40	0.39	1.26	0.39	0.09	0.65								
Sr	692.30	705.68	565.20	556.04	544.97	714.25	509.31	583.81	541.06	572.27	612.04								
standard dev.	4.87	4.51	4.38	5.50	0.72	1.71	3.57	0.21	6.32	8.09	3.80								
Rb	9.58	8.16	8.64	8.28	6.45	9.16	7.28	7.98	8.72	8.93	8.17								
standard dev.	0.23	0.19	0.08	0.34	0.39	0.78	0.21	1.25	0.16	0.70	0.82								

Values shown are percentages for SiO<sub>2</sub> through volatiles and parts per million for Nb through Rb. Standard deviations result from comparison of duplicate samples and refers to the data row just above it. Negative values in parentheses for volatiles indicates absorption during heating, i.e. initially zero.

Table 2.2 (cont.) - X-ray Fluorescence Geochemical Analyses

Eruptive Unit	Tan (Duffield&Bacon, 1981)		Black Canyon Flows												Coso Basin Andesite	
	BC Flow 1B	BC Flow 1	CHS Site 1	CHS Site 5	PC Flow 19	PC Flow 18	BC Flow 10	BC Flow 12	BC Flow 14A	BC Flow 18	Mean	Mean	AL Flow 3	AL Flow 5		
Locality /Flow #	Mean	Mean	Mean	Mean	Mean	Mean	Mean	Mean	Mean	Mean	Mean	Mean	Mean	Mean		
Sample ID	BC01B01A	BC0102A	CHS0103A	CHS0505A	PC1907A	PC1805A	BC1003A	BC12	BC14A02A	BC1806A			AL0303B	AL0501A		
SiO <sub>2</sub>	57.31	53.69	51.07	51.78	51.35	51.73	53.82	60.04	52.25	50.93			57.35	58.71		
standard dev.	0.36	0.25	0.06	0.10	0.07	0.06	0.39	0.13	0.08	0.26			0.24	0.01		
TiO <sub>2</sub>	1.04	1.24	1.34	1.28	1.34	1.27	1.22	0.84	1.41	1.47			1.06	1.00		
standard dev.	0.007	0.006	0.002	0.002	0.002	0.001	0.006	0.005	0.009	0.004			0.002	0.002		
Al <sub>2</sub> O <sub>3</sub>	15.61	15.71	16.41	16.27	16.48	15.77	16.73	16.16	16.12	16.28			15.85	15.87		
standard dev.	0.17	0.01	0.25	0.02	0.02	0.22	0.42	0.02	0.00	0.12			0.36	0.04		
Fe <sub>2</sub> O <sub>3</sub>	7.31	8.31	9.10	8.47	8.46	8.21	7.90	5.31	8.25	7.95			6.66	6.05		
standard dev.	0.01	0.10	0.04	0.12	0.04	0.20	0.13	0.04	0.11	0.03			0.04	0.05		
MnO	0.11	0.13	0.14	0.14	0.14	0.13	0.13	0.08	0.14	0.13			0.10	0.09		
standard dev.	0.001	0.001	0.001	0.000	0.001	0.001	0.006	0.000	0.000	0.001			0.000	0.001		
MgO	4.83	7.33	6.87	6.92	6.97	6.28	6.19	3.27	6.11	6.23			5.18	4.74		
standard dev.	0.06	0.04	0.11	0.01	0.02	0.04	0.31	0.07	0.03	0.00			0.02	0.03		
CaO	7.84	8.75	10.17	9.83	9.77	9.83	8.64	5.95	9.35	9.19			7.32	6.88		
standard dev.	0.20	0.02	0.01	0.01	0.01	0.02	0.19	0.02	0.02	0.07			0.01	0.01		
Na <sub>2</sub> O	3.85	3.56	3.66	3.72	3.51	3.62	3.74	4.03	3.60	3.31			3.83	3.79		
standard dev.	0.06	0.08	0.02	0.00	0.05	0.06	0.16	0.11	0.02	0.01			0.03	0.07		
K <sub>2</sub> O	1.84	1.04	0.88	0.88	0.80	0.97	1.14	2.50	1.39	1.24			2.07	2.19		
standard dev.	0.014	0.003	0.011	0.004	0.001	0.006	0.021	0.010	0.002	0.003			0.013	0.007		
P <sub>2</sub> O <sub>5</sub>	0.26	0.25	0.35	0.32	0.32	0.28	0.30	0.23	0.43	0.48			0.24	0.22		
standard dev.	0.012	0.003	0.011	0.004	0.006	0.012	0.004	0.002	0.007	0.004			0.004	0.003		
volatiles (LOI)	0.28	0.37	0 (-0.2)	0.39	0.86	1.92	0.20	1.61	0.94	2.88			0.35	0.46		
Nb	10.20	6.96	8.90	8.40	8.82	7.96	9.05	10.84	10.84	12.07			11.15	11.10		
standard dev.	0.27	0.14	0.13	0.03	0.10	0.08	0.27	0.28	0.36	0.41			0.53	0.55		
Zr	162.97	144.35	153.68	154.62	156.35	155.20	159.50	169.94	175.47	176.21			173.66	177.69		
standard dev.	1.71	0.17	1.57	1.40	0.09	2.11	2.43	1.38	1.05	1.29			0.25	1.13		
Y	20.07	22.64	23.94	22.81	23.80	22.84	22.16	17.54	24.49	24.35			20.80	19.26		
standard dev.	1.25	0.22	0.55	0.37	0.16	0.20	0.86	0.15	0.17	0.17			0.01	0.61		
Sr	527.33	465.23	677.53	694.56	670.20	606.36	630.17	644.48	754.19	759.69			560.20	572.34		
standard dev.	4.07	1.61	6.97	6.62	0.06	7.67	13.12	1.45	1.84	4.27			0.44	2.50		
Pb	38.78	16.72	11.27	11.04	9.79	13.09	17.61	47.94	17.44	16.46			35.10	38.78		
standard dev.	1.47	0.78	0.18	0.26	0.37	0.58	0.34	0.38	0.25	0.35			0.74	0.30		

Values shown are percentages for SiO<sub>2</sub> through volatiles and parts per million for Nb through Rb. Standard deviations result from comparison of duplicate samples and refers to the data row just above it. Negative values in parentheses for volatiles indicates absorption during heating. i.e. initially zero.

\* - Large differences in elemental concentrations between samples of unit Tan suggests that these data may be problematic.



Table 2.2 (cont.) - X-ray Fluorescence Geochemical Analyses

Eruptive Unit	QTbr <sub>2</sub> (Duffield&Bacon, 1981)										QTbr <sub>1</sub> ??		QTbr <sub>1</sub> (Duffield&Bacon, 1981)											
	RCE Locality		RC Flow 1		RC Flow 2		RC Flow 3				RC Flow 4		RC Flow 5		RC Flow 12		RCF Locality							
Locality /Flow #	Mean	RCE0101A	Mean	RCE0105A	Mean	RC0106D	Mean	RC0201B	Mean	RC0301A	Mean	RC0303A	Mean	RC0401A	Mean	RC0402A	Mean	RC0503A	Mean	RC1203A	Mean	RCF5	Mean	RCF7
Sample ID	56.77	56.48	56.51	56.41	56.41	56.41	56.41	56.41	56.41	56.41	56.41	56.41	56.41	56.41	56.41	56.41	56.41	56.41	56.41	56.41	56.41	56.41	56.41	56.41
SiO <sub>2</sub>	0.41	0.02	0.07	0.08	0.08	0.08	0.08	0.08	0.08	0.08	0.08	0.08	0.08	0.08	0.08	0.08	0.08	0.08	0.08	0.08	0.08	0.08	0.08	0.08
standard dev.	0.97	0.97	0.98	0.95	0.95	0.95	0.95	0.95	0.95	0.95	0.95	0.95	0.95	0.95	0.95	0.95	0.95	0.95	0.95	0.95	0.95	0.95	0.95	0.95
TiO <sub>2</sub>	0.009	0.002	0.008	0.008	0.008	0.008	0.008	0.008	0.008	0.008	0.008	0.008	0.008	0.008	0.008	0.008	0.008	0.008	0.008	0.008	0.008	0.008	0.008	0.008
standard dev.	18.40	18.81	17.99	18.71	18.71	18.71	18.71	18.71	18.71	18.71	18.71	18.71	18.71	18.71	18.71	18.71	18.71	18.71	18.71	18.71	18.71	18.71	18.71	18.71
Al <sub>2</sub> O <sub>3</sub>	0.16	0.00	0.10	0.35	0.35	0.35	0.35	0.35	0.35	0.35	0.35	0.35	0.35	0.35	0.35	0.35	0.35	0.35	0.35	0.35	0.35	0.35	0.35	0.35
standard dev.	6.04	5.96	5.98	5.65	5.65	5.65	5.65	5.65	5.65	5.65	5.65	5.65	5.65	5.65	5.65	5.65	5.65	5.65	5.65	5.65	5.65	5.65	5.65	5.65
Fe <sub>2</sub> O <sub>3</sub>	0.21	0.06	0.03	0.06	0.06	0.06	0.06	0.06	0.06	0.06	0.06	0.06	0.06	0.06	0.06	0.06	0.06	0.06	0.06	0.06	0.06	0.06	0.06	0.06
standard dev.	0.08	0.08	0.08	0.08	0.08	0.08	0.08	0.08	0.08	0.08	0.08	0.08	0.08	0.08	0.08	0.08	0.08	0.08	0.08	0.08	0.08	0.08	0.08	0.08
MnO	0.000	0.000	0.000	0.000	0.000	0.000	0.000	0.000	0.000	0.000	0.000	0.000	0.000	0.000	0.000	0.000	0.000	0.000	0.000	0.000	0.000	0.000	0.000	0.000
standard dev.	3.99	3.89	4.03	3.83	3.83	3.83	3.83	3.83	3.83	3.83	3.83	3.83	3.83	3.83	3.83	3.83	3.83	3.83	3.83	3.83	3.83	3.83	3.83	3.83
MgO	0.02	0.01	0.03	0.07	0.07	0.07	0.07	0.07	0.07	0.07	0.07	0.07	0.07	0.07	0.07	0.07	0.07	0.07	0.07	0.07	0.07	0.07	0.07	0.07
standard dev.	7.96	7.95	8.64	8.95	8.95	8.95	8.95	8.95	8.95	8.95	8.95	8.95	8.95	8.95	8.95	8.95	8.95	8.95	8.95	8.95	8.95	8.95	8.95	8.95
CaO	0.04	0.00	0.06	0.11	0.11	0.11	0.11	0.11	0.11	0.11	0.11	0.11	0.11	0.11	0.11	0.11	0.11	0.11	0.11	0.11	0.11	0.11	0.11	0.11
standard dev.	3.86	3.84	3.80	3.61	3.61	3.61	3.61	3.61	3.61	3.61	3.61	3.61	3.61	3.61	3.61	3.61	3.61	3.61	3.61	3.61	3.61	3.61	3.61	3.61
Na <sub>2</sub> O	0.08	0.02	0.05	0.18	0.18	0.18	0.18	0.18	0.18	0.18	0.18	0.18	0.18	0.18	0.18	0.18	0.18	0.18	0.18	0.18	0.18	0.18	0.18	0.18
standard dev.	1.74	1.78	1.77	1.59	1.59	1.59	1.59	1.59	1.59	1.59	1.59	1.59	1.59	1.59	1.59	1.59	1.59	1.59	1.59	1.59	1.59	1.59	1.59	1.59
K <sub>2</sub> O	0.011	0.001	0.016	0.019	0.019	0.019	0.019	0.019	0.019	0.019	0.019	0.019	0.019	0.019	0.019	0.019	0.019	0.019	0.019	0.019	0.019	0.019	0.019	0.019
standard dev.	0.21	0.22	0.21	0.21	0.21	0.21	0.21	0.21	0.21	0.21	0.21	0.21	0.21	0.21	0.21	0.21	0.21	0.21	0.21	0.21	0.21	0.21	0.21	0.21
P <sub>2</sub> O <sub>5</sub>	0.000	0.012	0.005	0.003	0.003	0.003	0.003	0.003	0.003	0.003	0.003	0.003	0.003	0.003	0.003	0.003	0.003	0.003	0.003	0.003	0.003	0.003	0.003	0.003
standard dev.	0.25	0.11	0.59	1.83	1.83	1.83	1.83	1.83	1.83	1.83	1.83	1.83	1.83	1.83	1.83	1.83	1.83	1.83	1.83	1.83	1.83	1.83	1.83	1.83
volatiles (LOI)																								
Nb	9.86	10.15	10.36	9.73	9.73	9.73	9.73	9.73	9.73	9.73	9.73	9.73	9.73	9.73	9.73	9.73	9.73	9.73	9.73	9.73	9.73	9.73	9.73	9.73
standard dev.	0.45	0.64	0.21	0.00	0.00	0.00	0.00	0.00	0.00	0.00	0.00	0.00	0.00	0.00	0.00	0.00	0.00	0.00	0.00	0.00	0.00	0.00	0.00	0.00
Zr	158.87	159.23	160.71	153.89	153.89	153.89	153.89	153.89	153.89	153.89	153.89	153.89	153.89	153.89	153.89	153.89	153.89	153.89	153.89	153.89	153.89	153.89	153.89	153.89
standard dev.	1.63	0.38	0.63	1.68	1.68	1.68	1.68	1.68	1.68	1.68	1.68	1.68	1.68	1.68	1.68	1.68	1.68	1.68	1.68	1.68	1.68	1.68	1.68	1.68
Y	17.03	17.44	16.99	15.64	15.64	15.64	15.64	15.64	15.64	15.64	15.64	15.64	15.64	15.64	15.64	15.64	15.64	15.64	15.64	15.64	15.64	15.64	15.64	15.64
standard dev.	0.00	0.98	0.18	0.55	0.55	0.55	0.55	0.55	0.55	0.55	0.55	0.55	0.55	0.55	0.55	0.55	0.55	0.55	0.55	0.55	0.55	0.55	0.55	0.55
Sr	794.17	800.29	803.09	807.79	807.79	807.79	807.79	807.79	807.79	807.79	807.79	807.79	807.79	807.79	807.79	807.79	807.79	807.79	807.79	807.79	807.79	807.79	807.79	807.79
standard dev.	8.08	2.46	4.47	9.60	9.60	9.60	9.60	9.60	9.60	9.60	9.60	9.60	9.60	9.60	9.60	9.60	9.60	9.60	9.60	9.60	9.60	9.60	9.60	9.60
Pb	38.10	36.52	36.95	31.65	31.65	31.65	31.65	31.65	31.65	31.65	31.65	31.65	31.65	31.65	31.65	31.65	31.65	31.65	31.65	31.65	31.65	31.65	31.65	31.65
standard dev.	0.07	0.65	0.17	0.03	0.03	0.03	0.03	0.03	0.03	0.03	0.03	0.03	0.03	0.03	0.03	0.03	0.03	0.03	0.03	0.03	0.03	0.03	0.03	0.03

Values shown are percentages for SiO<sub>2</sub> through volatiles and parts per million for Nb through Pb. Standard deviations result from comparison of duplicate samples and refers to the data row just above it. Negative values in parentheses for volatiles indicates absorption during heating, i.e. initially zero.

\* - Large differences in elemental concentrations between samples within RC flow 3 and RC flow 4 suggests that these data may be problematic.



Table 2.2 (cont.) -X-ray Fluorescence Geochemical Analyses

Erupitive Unit	QTbr <sub>3</sub> (Duffield&Bacon, 1981)				QTbr <sub>4</sub> (Duffield&Bacon, 1981)				QTbr <sub>8</sub> (Duffield&Bacon, 1981)						
Locality /Flow #	RCC Locality				RCD Locality				RCB Locality				MSA Top Flow		MSA Bottom Flow
Sample ID	Mean	Mean	Mean	Mean	Mean	Mean	Mean	Mean	Mean	Mean	Mean	Mean	Mean	Mean	Mean
SiO <sub>2</sub>	RCC0103B	RCC0107C	RCD0104C	RCD0108C	RCB0105A	RCB0102A									
standard dev.	55.04	54.64	52.03	51.81	52.62	52.17	54.79	57.33							
TiO <sub>2</sub>	0.11	0.18	0.12	0.00	0.04	0.05	0.06	0.09							
standard dev.	1.23	1.25	1.69	1.72	1.85	1.82	1.61	1.10							
Al <sub>2</sub> O <sub>3</sub>	0.007	0.004	0.003	0.002	0.024	0.010	0.016	0.003							
standard dev.	16.63	16.57	17.43	17.76	17.32	17.52	16.74	16.24							
Fe <sub>2</sub> O <sub>3</sub>	0.00	0.02	0.01	0.01	0.11	0.04	0.06	0.01							
standard dev.	7.41	7.64	8.08	8.43	8.51	8.63	7.78	6.77							
MnO	0.05	0.40	0.01	0.07	0.23	0.04	0.08	0.09							
standard dev.	0.12	0.12	0.13	0.13	0.13	0.14	0.13	0.10							
MgO	0.001	0.001	0.001	0.001	0.000	0.000	0.002	0.000							
standard dev.	6.01	5.13	5.18	5.38	4.98	5.23	5.40	5.19							
CaO	0.03	0.08	0.04	0.05	0.11	0.02	0.05	0.02							
standard dev.	8.19	9.30	9.72	8.91	8.16	8.46	6.73	6.56							
Na <sub>2</sub> O	0.01	0.01	0.01	0.01	0.03	0.01	0.04	0.02							
standard dev.	3.65	3.56	4.03	4.11	4.34	4.05	4.33	4.13							
K <sub>2</sub> O	0.03	0.17	0.04	0.04	0.04	0.06	0.09	0.06							
standard dev.	1.45	1.51	1.24	1.25	1.52	1.44	2.03	2.26							
P <sub>2</sub> O <sub>5</sub>	0.001	0.004	0.003	0.005	0.003	0.005	0.004	0.014							
standard dev.	0.27	0.28	0.48	0.49	0.56	0.54	0.46	0.31							
volatiles (LOI)	0.014	0.009	0.001	0.011	0.012	0.005	0.002	0.006							
	0 (-0.06)	0.09	0.98	1.91	0.98	1.25	0 (-0.23)	0.62							
Nb	14.80	15.40	15.52	15.56	17.74	17.12	23.39	16.55							
standard dev.	0.55	0.56	0.21	0.56	0.59	0.50	0.05	0.42							
Zr	166.02	167.06	199.69	202.07	223.44	216.42	249.89	229.07							
standard dev.	0.42	2.48	0.13	2.05	3.95	1.89	1.87	2.41							
Y	20.76	20.48	25.64	24.54	26.35	26.86	26.00	22.84							
standard dev.	0.18	0.50	0.05	1.32	0.40	0.32	0.11	0.62							
Sr	622.54	615.04	933.16	925.89	887.76	872.67	614.07	584.13							
standard dev.	0.49	5.07	0.39	6.76	14.42	9.75	4.23	6.89							
Pb	25.73	27.14	17.17	17.72	22.78	20.94	28.26	41.27							
standard dev.	0.11	0.21	0.87	0.68	0.61	0.09	0.39	0.05							

Values shown are percentages for SiO<sub>2</sub> through volatiles and parts per million for Nb through Rb. Standard deviations result from comparison of duplicate samples and refers to the data row just above it. Negative values in parentheses for volatiles indicates absorption during heating, i.e. initially zero.

Table 3.1  $^{40}\text{Ar}/^{39}\text{Ar}$  Geochronology.

Eruptive Unit	Location	Sample Name, Flow #	Method and Material	Comments	Age (Ma) and 2 $\sigma$ error	Weighted Mean Age
Haiwee Springs basalt	HS	HS 19, flow 19*	Isochron, Groudmass	Argon recoil, age is a minimum	$>2.96 \pm 0.03$	
Older Dacite of Coso Hot Springs	CWA	Tdo, Duffield & Bacon unit Tdo	Isochron, Groudmass	Excess Argon, age is a maximum	$<2.83 \pm 0.02$	
QTbr <sub>1</sub> (?)	RC	RC14, flow 14†	Plateau, Groudmass		$2.62 \pm 0.03$	$2.62 \pm 0.02$
QTbr <sub>1</sub> (?)	RC	RC14, flow 14†	Plateau, Plagioclase		$2.63 \pm 0.04$	
QTbr <sub>2</sub>	RC	RC01, flow 1†	Plateau, Groudmass		$1.37 \pm 0.04$	
Black Canyon flows	BC	BC18, flow 18	Plateau, Groudmass		$3.41 \pm 0.04$	
Basalt of Coso Wash	CMA	CMA, Duffield & Bacon unit Qbc	Isochron, Whole Rock	Previously mis-dated or mis-identified	c.a. 0.97	
Petroglyph Canyon basalt	FS	BD0201A, flow 2 ‡	Isochron, Whole Rock		$3.19 \pm 0.04$	$3.22 \pm 0.02$
Petroglyph Canyon basalt	FS	BD0301A, flow 3 ‡	Isochron, Whole Rock		$3.20 \pm 0.04$	
Petroglyph Canyon basalt	FS	BD0303A, flow 3 ‡	Isochron, Whole Rock		$3.20 \pm 0.03$	
Petroglyph Canyon basalt	FS	BD0403A, flow 4 ‡	Isochron, Whole Rock		$3.25 \pm 0.03$	
Petroglyph Canyon basalt	FS	BD1403A, flow 14 ‡	Isochron, Whole Rock		$3.25 \pm 0.05$	
Petroglyph Canyon basalt	FS	BD1103A, flow 11 ‡	Isochron, Whole Rock		$3.26 \pm 0.04$	
Cole Flat basalt	FS	BD0802A, flow 8 ‡	Isochron, Whole Rock		$3.51 \pm 0.04$	$3.50 \pm 0.03$

Cole Flat basalt	FS	BD1204A, flow 12 ‡	Isochron, Whole Rock		3.49±0.05	
---------------------	----	-----------------------	----------------------------	--	-----------	--

\* numbered from bottom of stratigraphic section, † numbered from top of stratigraphic section, ‡ numbered irregularly

## Figures

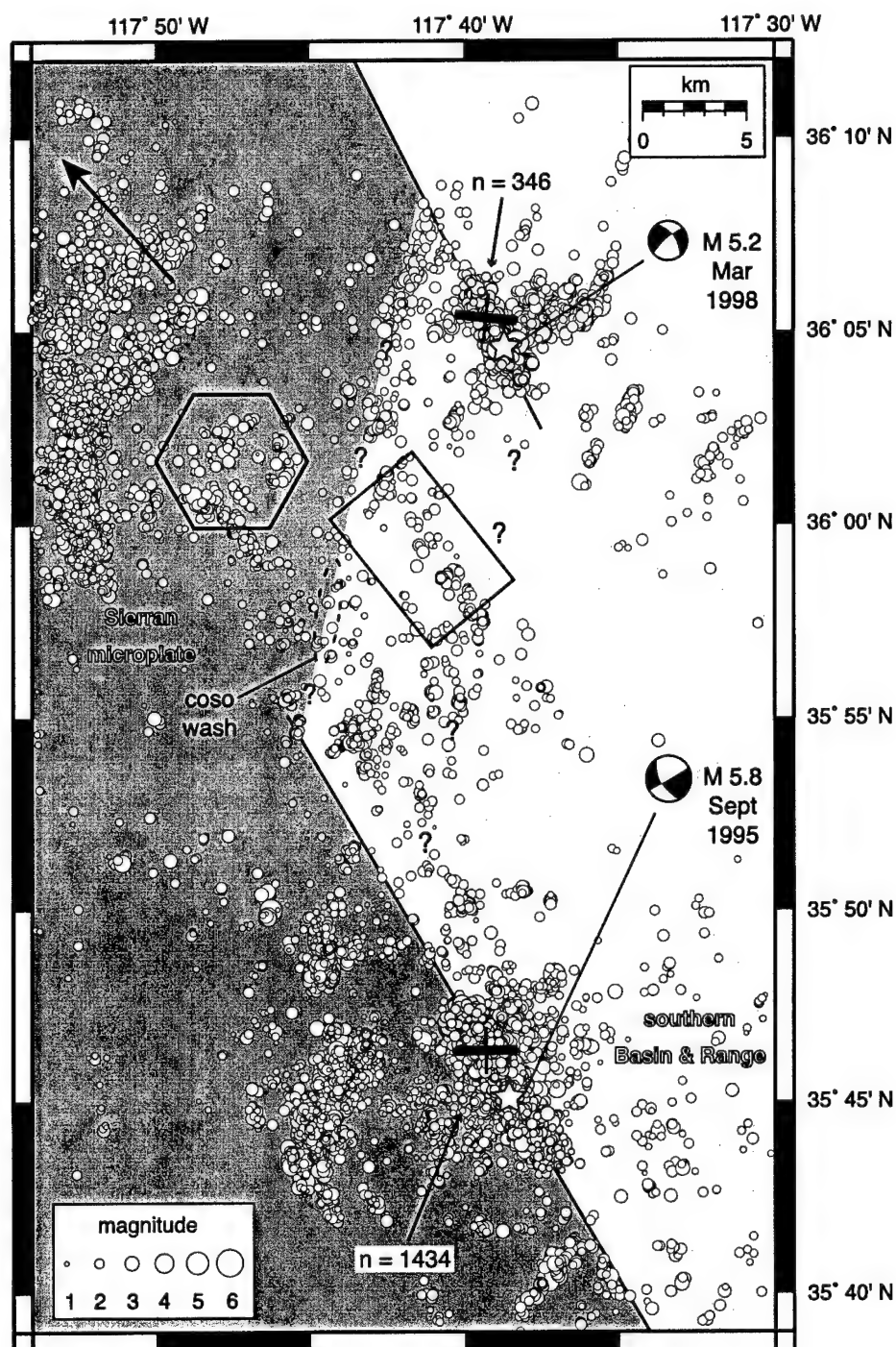
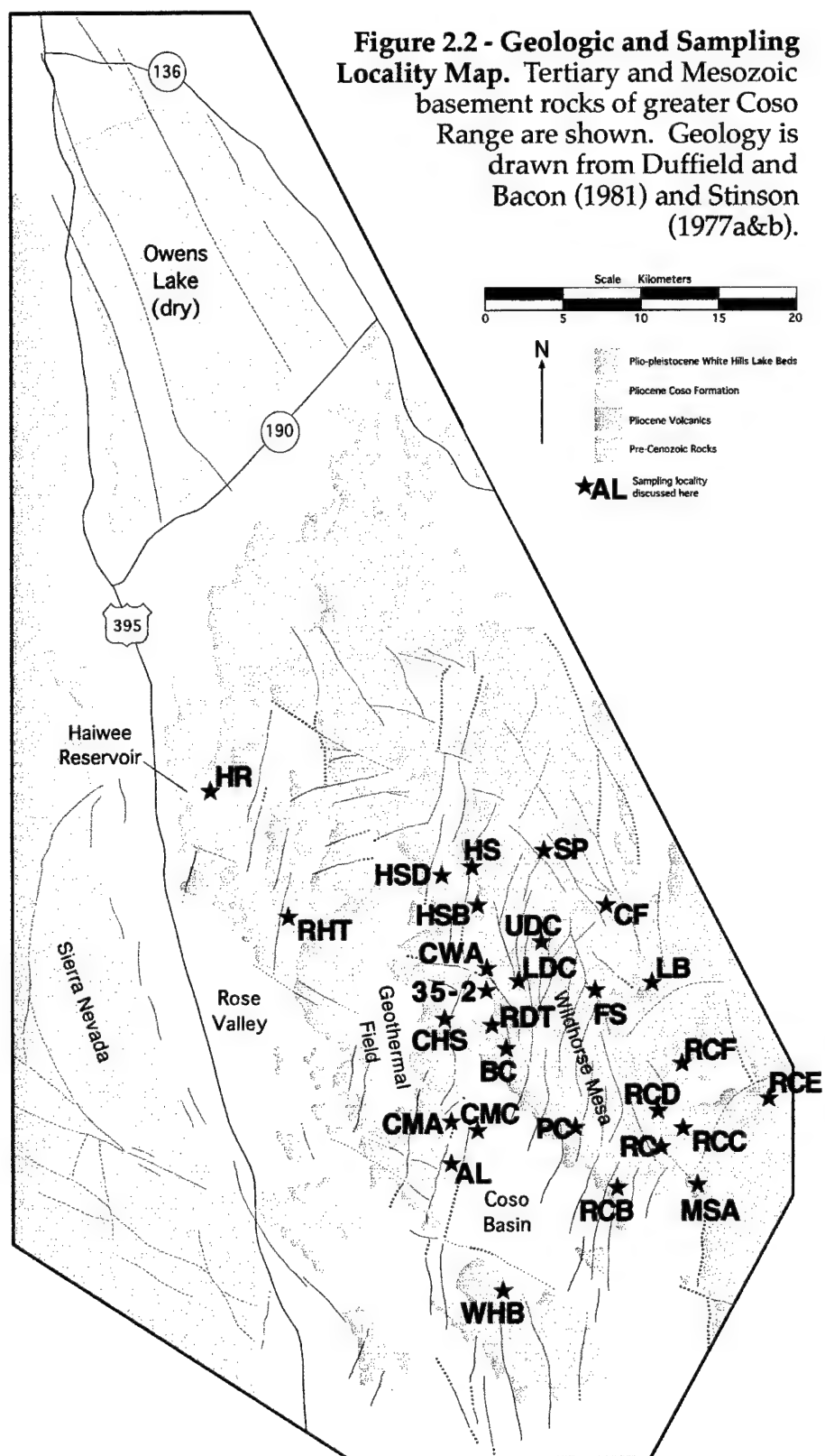


Figure 2.1. Seismically-defined right-releasing step in the boundary between the Sierran microplate and the southern Basin and Range Province in the area of the Wild Horse Mesa and Coso Geothermal Field (indicated by the six-sided figure). The rectangle approximately outlines the seismic events described in Figures 3.1 and 3.2. The trend of subhorizontal  $d_1$  and  $d_3$  for best-fitting models for events shown in light grey are indicated by heavy and light lines, respectively. The best-fitting great circles for these event epicenters are subparallel to the trajectory of the Sierran microplate with respect to North America (Dixon et al., 2000) shown with the large arrow.





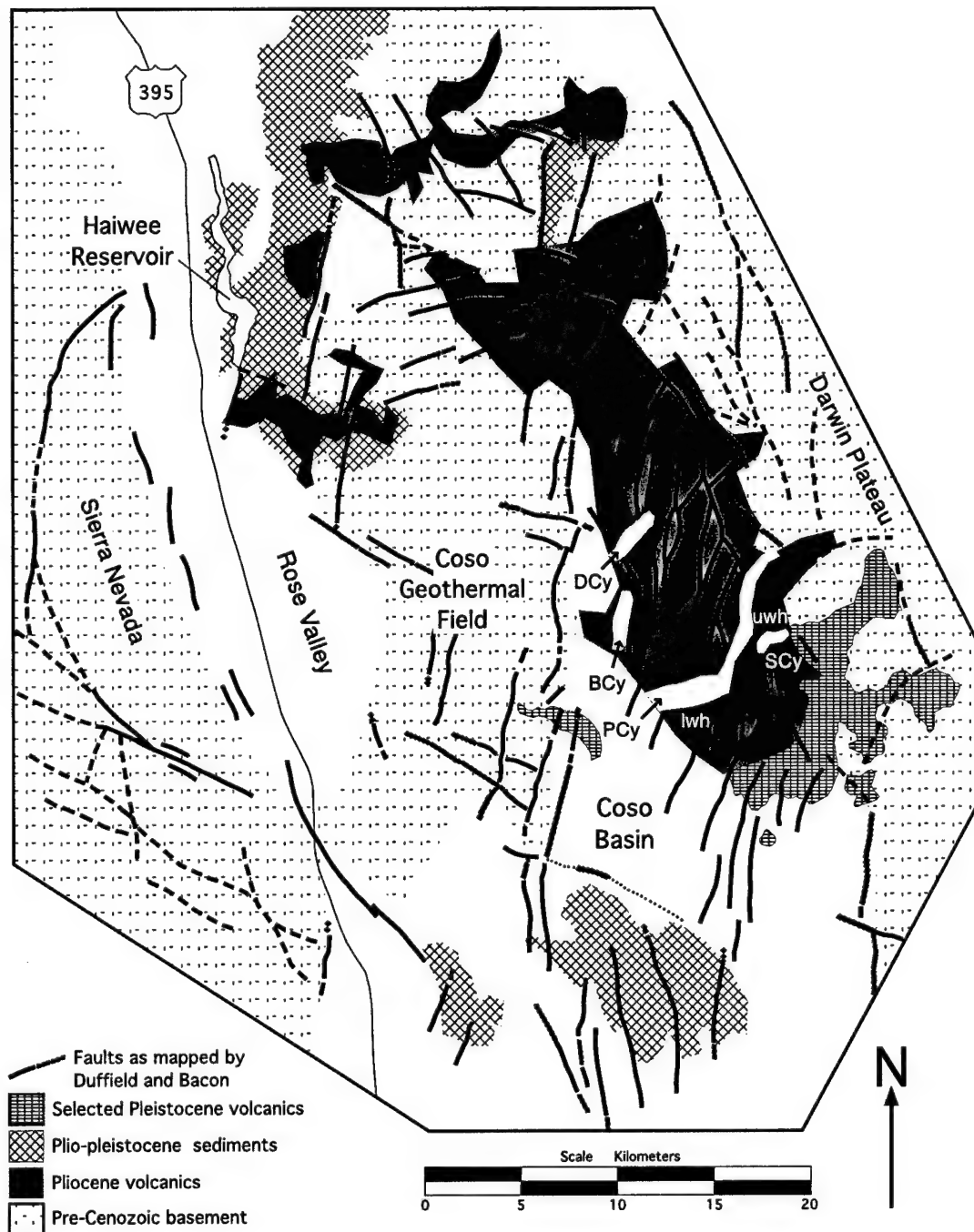


Figure 2.3 - Geologic map of the Coso Volcanic field showing approximate locations where brittle faults were examined as white bands within the Pliocene volcanics (solid grey). Canyons labeled as follows: BCy = Black Canyon, DCy = Dead End Canyon, lwh = lower Wild Horse Mesa, PCy = Petroglyph Canyon and SCy = Sheep Canyon, uwh = upper Wild Horse Mesa.

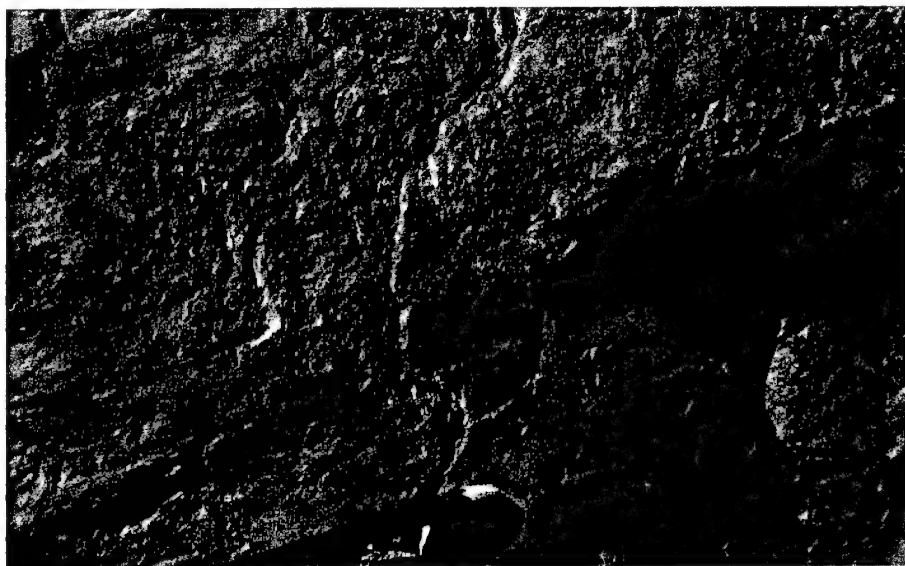


Figure 2.4. Example of shear-sense indicators preserved on outcrop-scale fault surfaces. Pencil at bottom points in the direction of the missing block. Lineated subsidiary shear surfaces (R planes) intersect this primary slip surface (Y shear) creating two lunate features above and to the right of the pencil tip (both somewhat shaded).

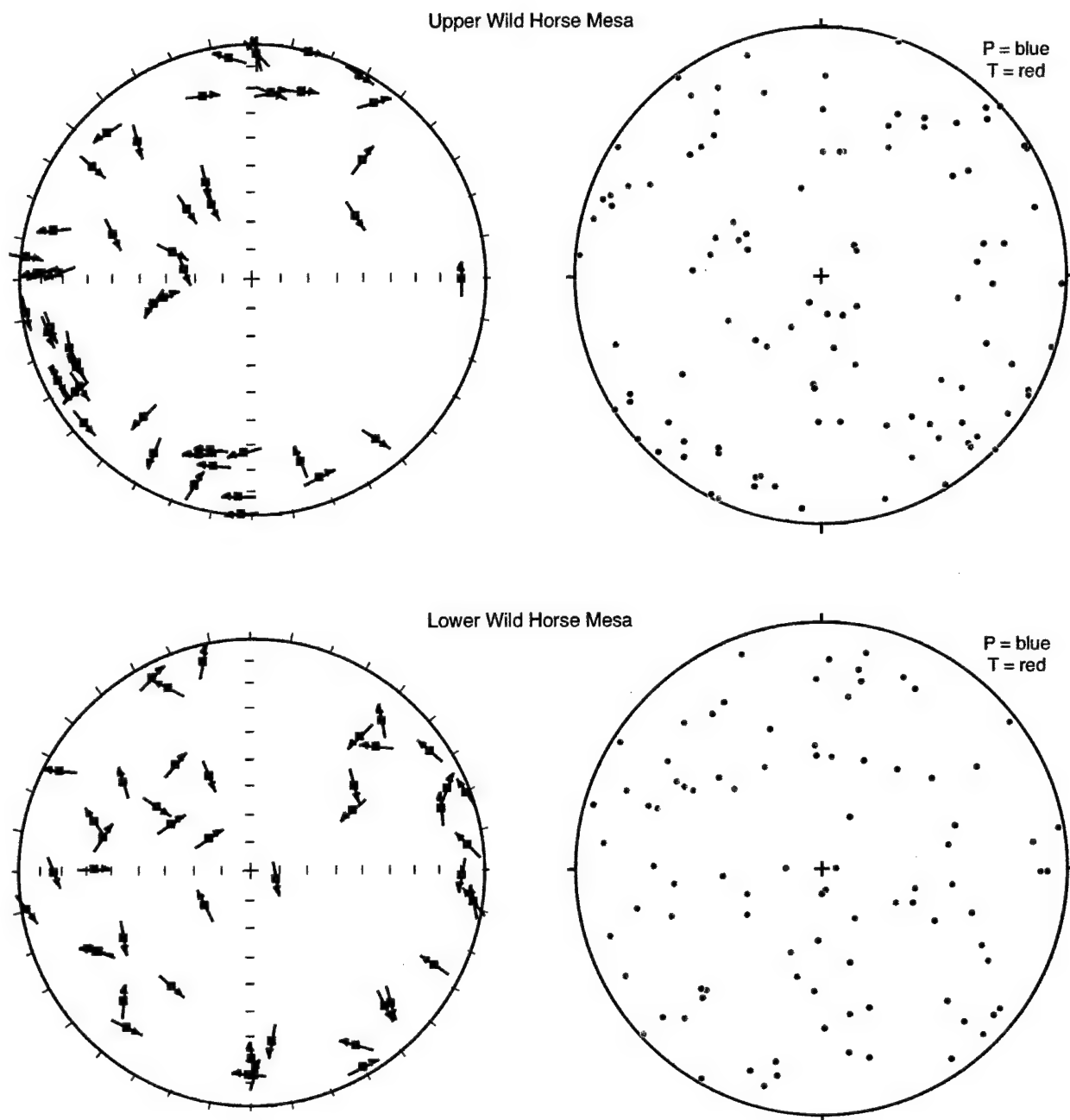


Figure 2.5. Tangent lineations (left) and kinematic P and T axes (right) for outcrop-scale brittle faults at upper and lower Wild Horse Mesa (top and bottom, respectively). All plots are lower-hemisphere, equal-area projections. The tangent lineation plots show poles fault planes with arrows indicating the direction of motion of the footwall blocks.

# Wild Horse Mesa Seismogenic Strain Events 0-5 km deep

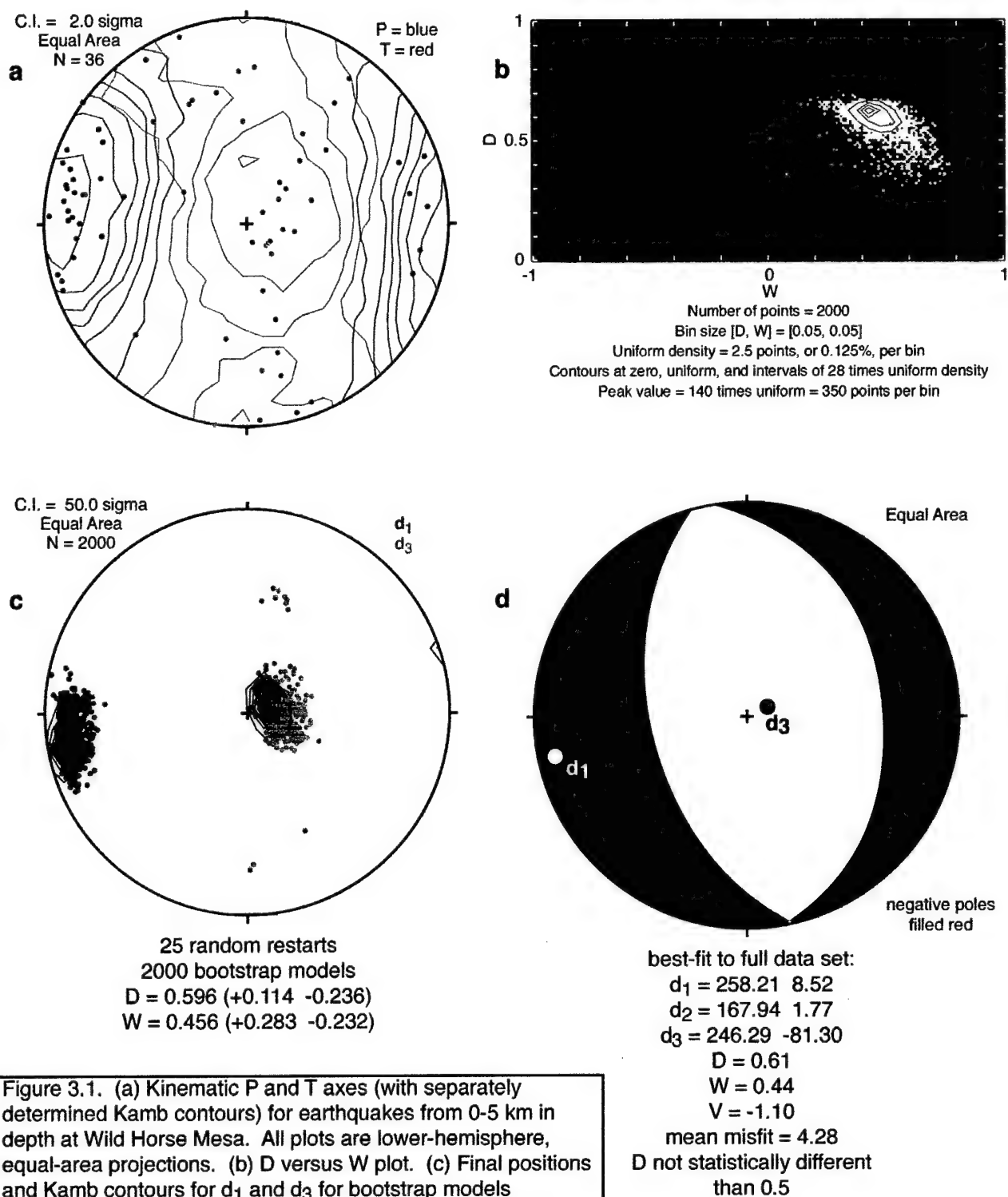


Figure 3.1. (a) Kinematic P and T axes (with separately determined Kamb contours) for earthquakes from 0-5 km in depth at Wild Horse Mesa. All plots are lower-hemisphere, equal-area projections. (b) D versus W plot. (c) Final positions and Kamb contours for d<sub>1</sub> and d<sub>3</sub> for bootstrap models (contoured separately. (d) Strainball plot of the best-fitting strain tensor for the full data set.

# Wild Horse Mesa Seismicity Strainball Events 5-8 km deep

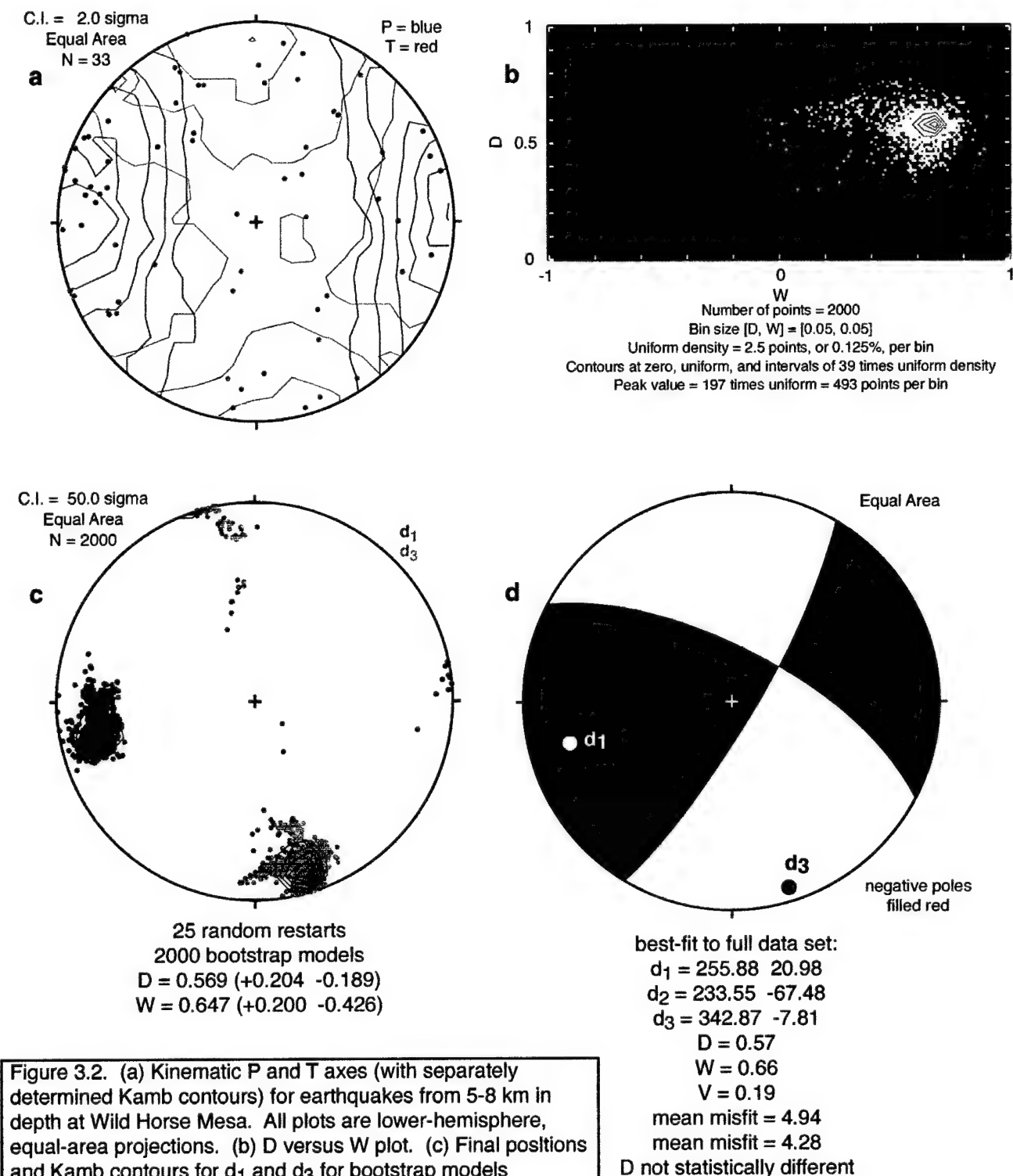


Figure 3.2. (a) Kinematic P and T axes (with separately determined Kamb contours) for earthquakes from 5-8 km in depth at Wild Horse Mesa. All plots are lower-hemisphere, equal-area projections. (b) D versus W plot. (c) Final positions and Kamb contours for d<sub>1</sub> and d<sub>3</sub> for bootstrap models (contoured separately). (d) Strainball plot of the best-fitting strain tensor for the full data set.

Lower Wild Horse Mesa  
WNW-plunging P Axis Maximum

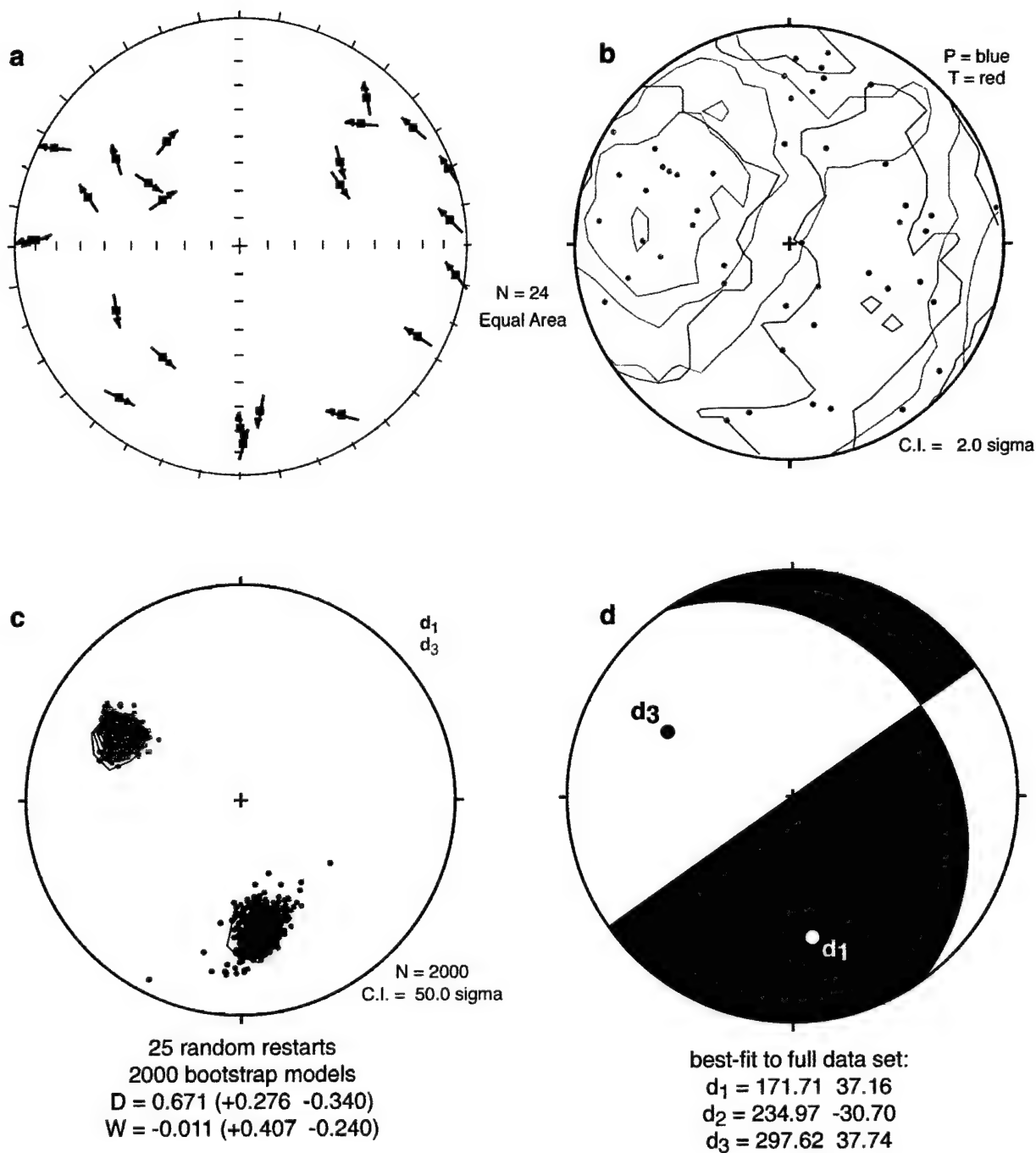


Figure 3.3. (a) Tangent lineations and (b) kinematic P and T axes for outcrop-scale brittle faults at lower Wild Horse Mesa that display a shallow west northwest-plunging P axis maximum. All plots are lower-hemisphere, equal-area projections. (c) Final positions and Kamb contours for  $d_1$  and  $d_3$  for bootstrap models (contoured separately). (d) Strainball plot of the best-fitting strain tensor for the full data set.



# Upper Wild Horse Mesa Crustal Thinning

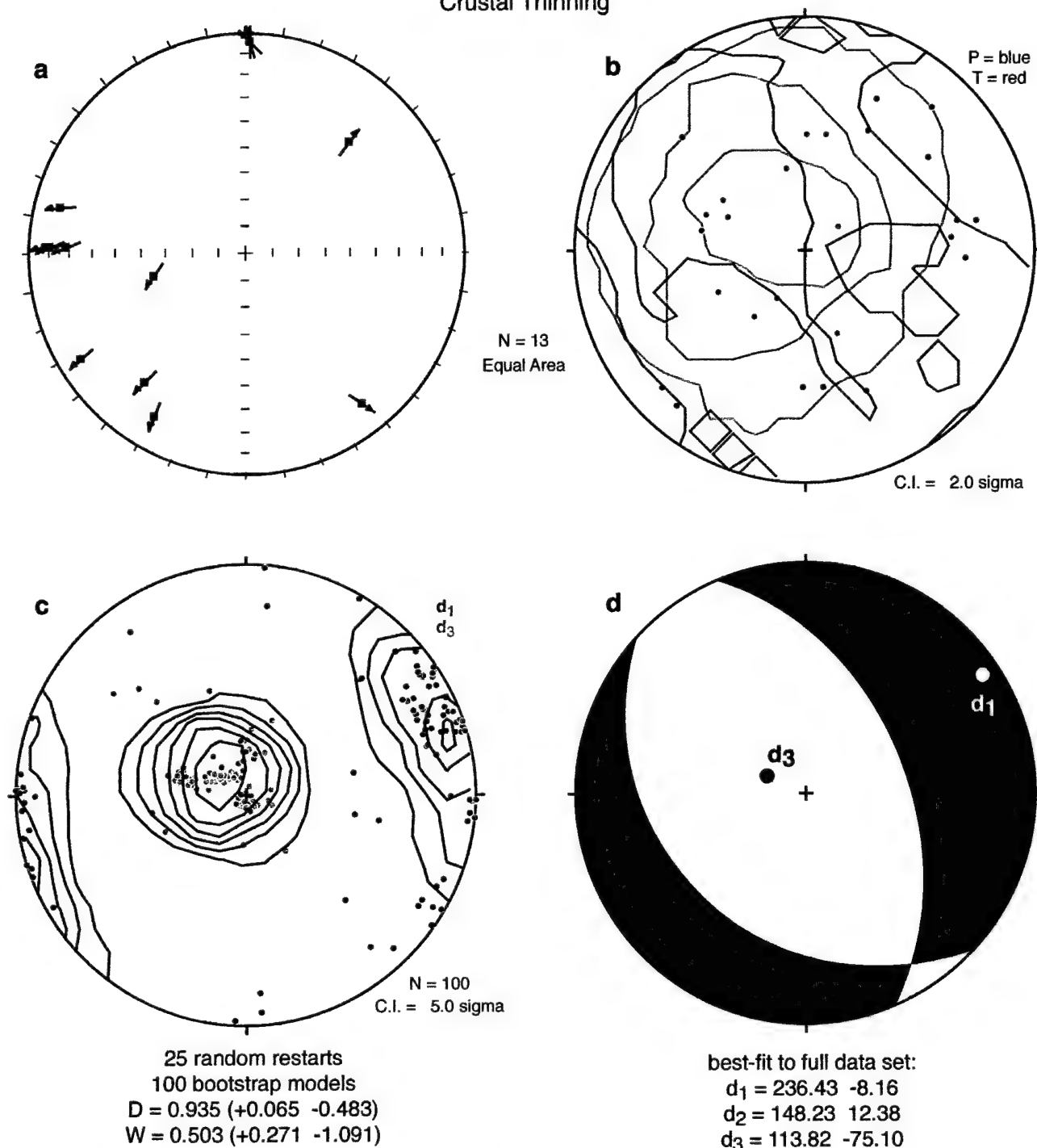


Figure 3.4. (a) Tangent lineations and (b) kinematic P and T axes (with separately determined Kamb contours) for outcrop-scale brittle faults at upper and lower Wild Horse Mesa that accommodate normal faulting. All plots are lower-hemisphere, equal-area projections. (c) Final positions and Kamb contours for  $d_1$  and  $d_3$  for bootstrap models (contoured separately). (d) Strainball plot of the best-fitting strain tensor for the full data set.

# Upper Wild Horse Mesa Crustal Thickening

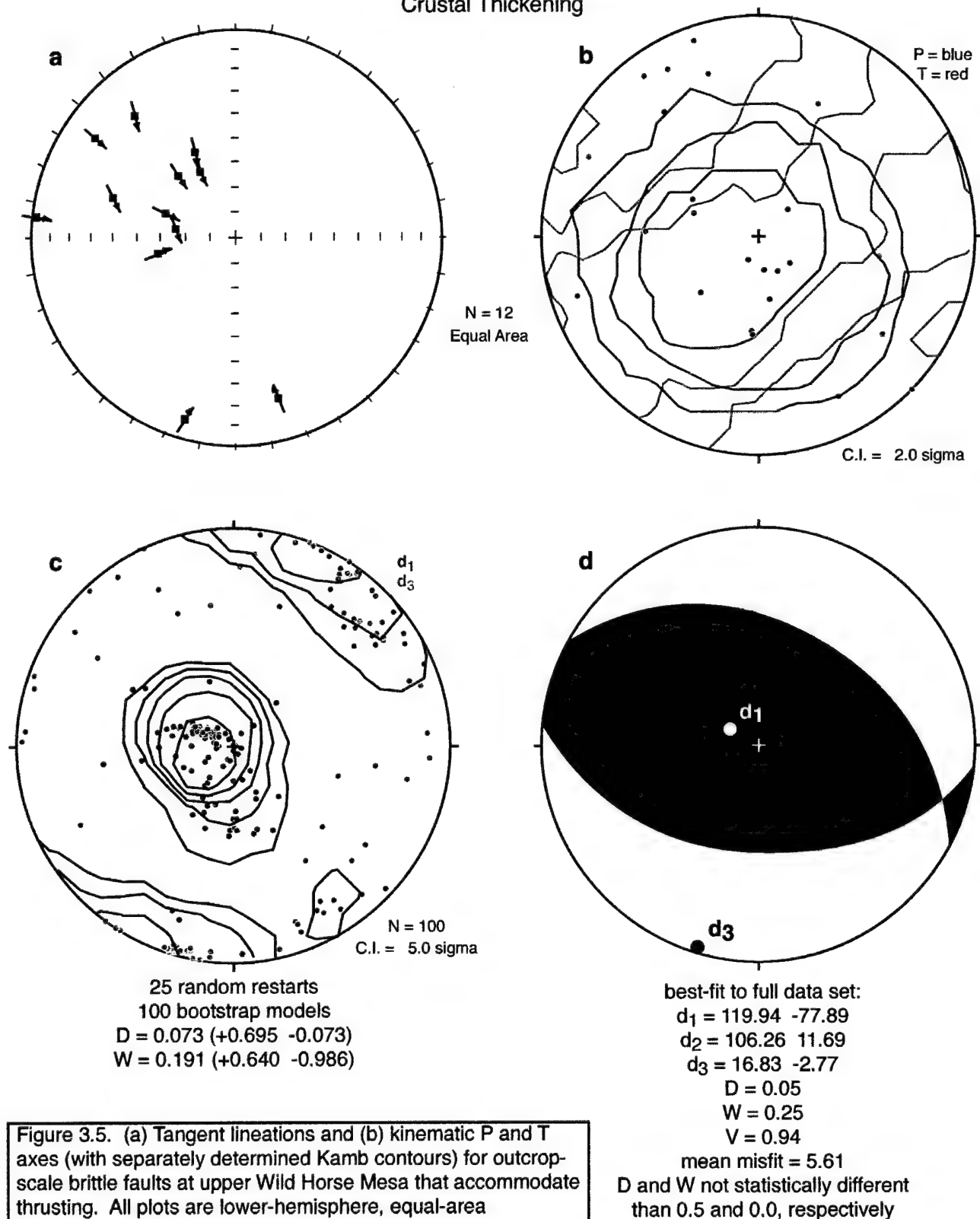


Figure 3.5. (a) Tangent lineations and (b) kinematic P and T axes (with separately determined Kamb contours) for outcrop-scale brittle faults at upper Wild Horse Mesa that accommodate thrusting. All plots are lower-hemisphere, equal-area projections. (c) Final positions and Kamb contours for  $d_1$  and  $d_3$  for bootstrap models (contoured separately). (d) Strainball plot of the best-fitting strain tensor for the full data set.

# Upper Wild Horse Mesa Horizontal Shearing

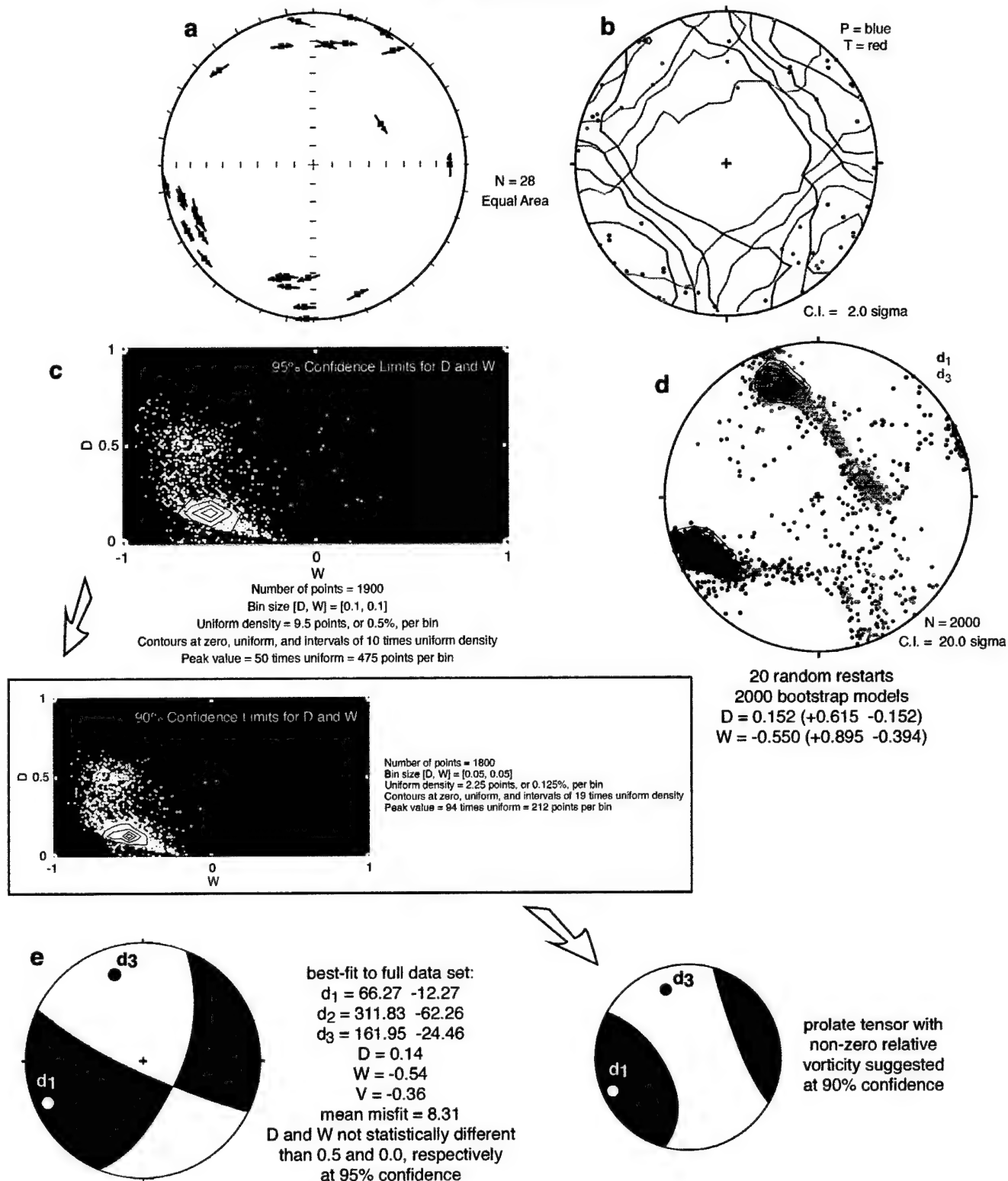
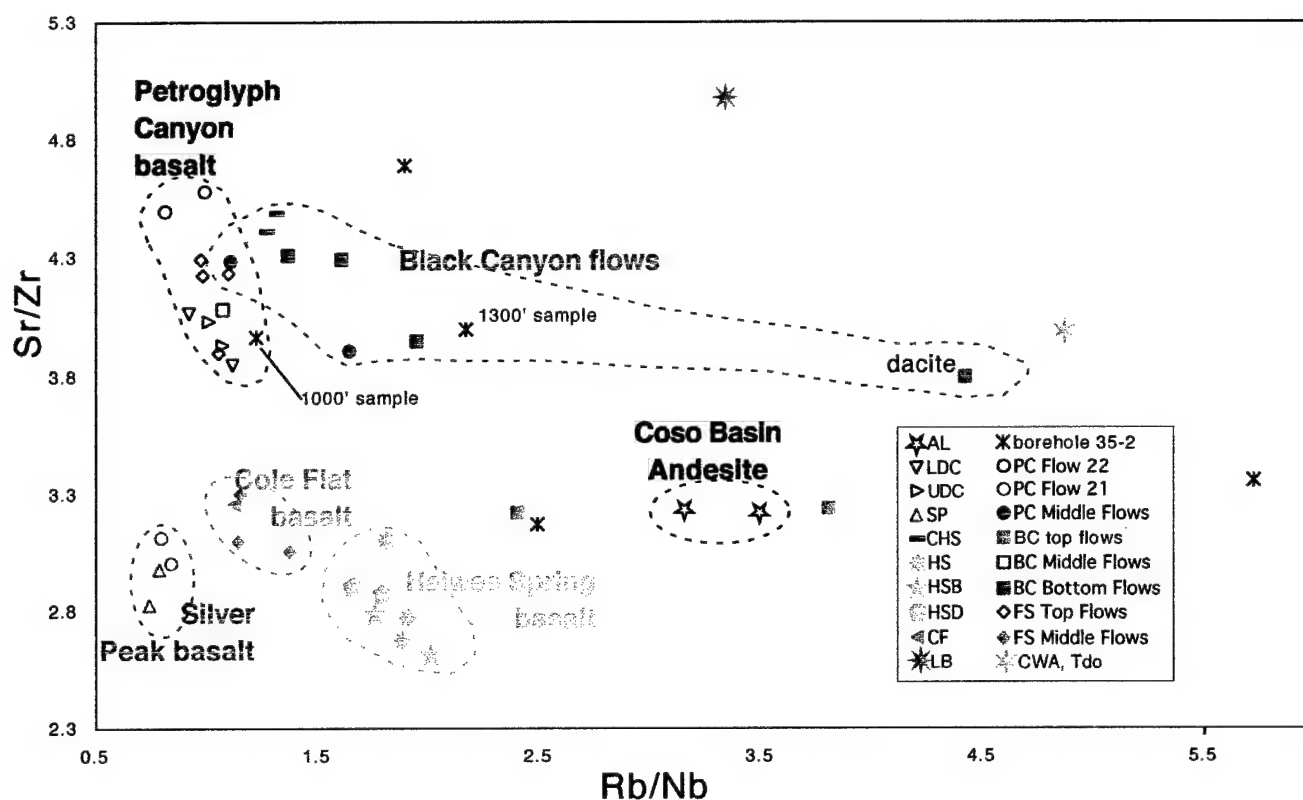
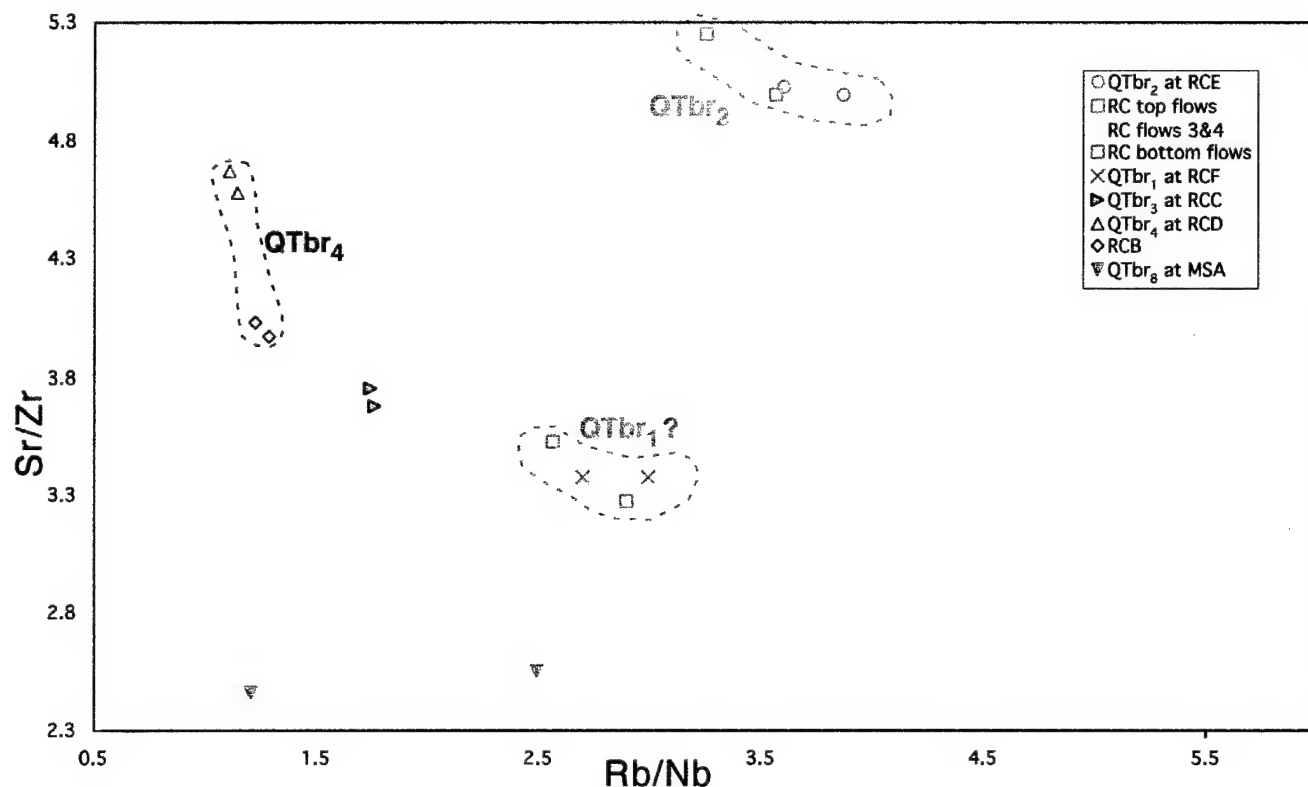


Figure 3.6. Results for outcrop-scale brittle faults at upper Wild Horse Mesa that accommodate horizontal shearing. Same plots as Figures 3.4 and 3.5 except that plots of D versus W are included for the 95% and 90% (in box) confidence levels (c). See text for discussion of statistics and interpretation of statistics at 90% confidence (plot at right).

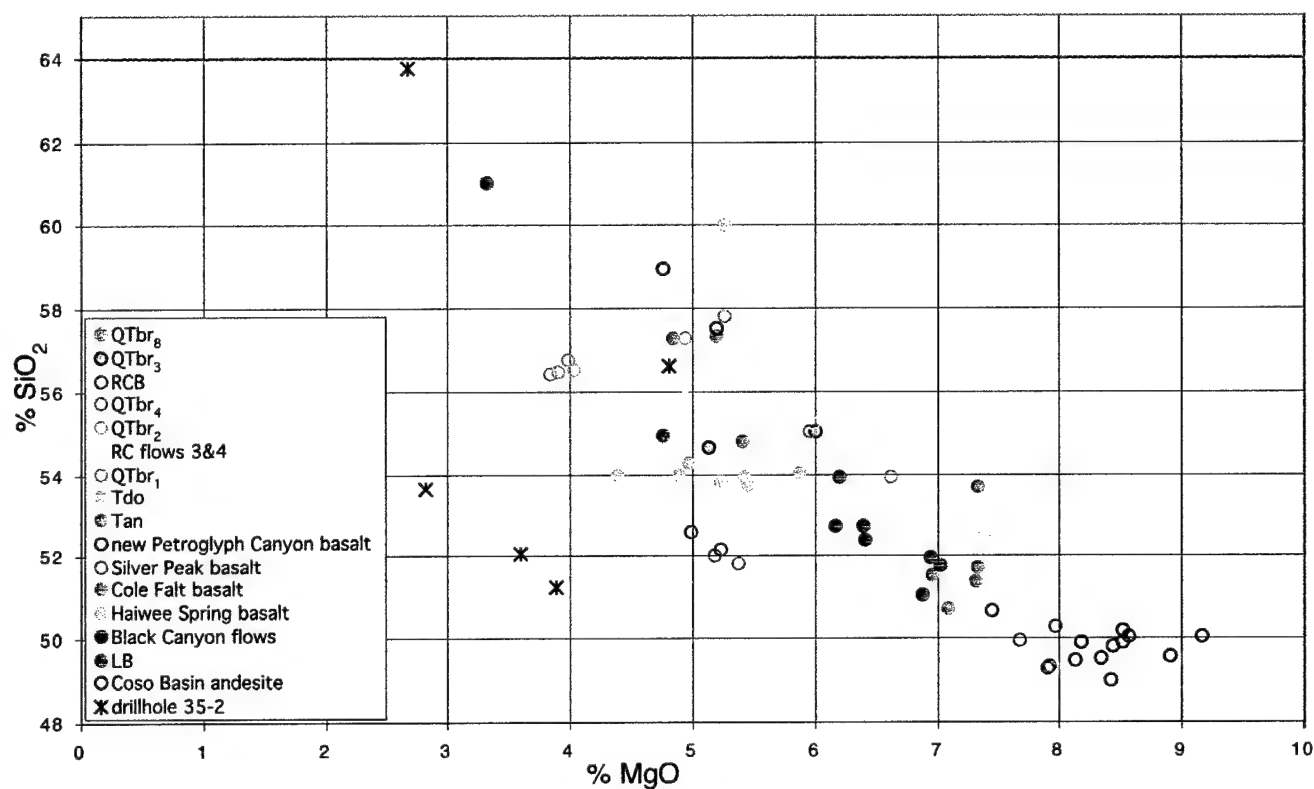


**Figure 3.7 - Combined Trace Element XRF and Paleomagnetic Fingerprinting, Pliocene Wild Horse Mesa and Drillhole 35-2.** Magnetic polarity is indicated by solid symbols for normal, open symbols for reversed, characters for unknown polarity. The use of paleomagnetism and geochemistry allows rigorous separation of units, as indicated

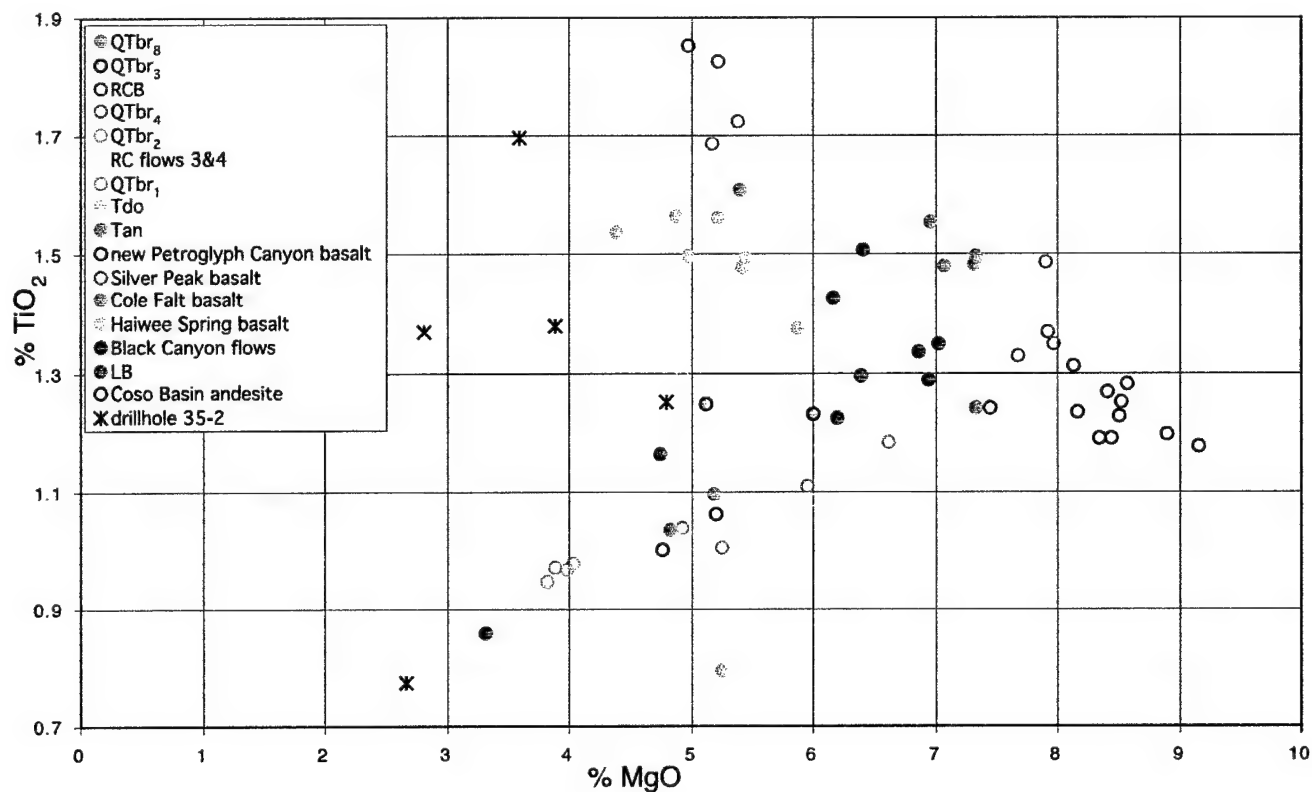


**Figure 3.8 - Combined Trace Element XRF and Paleomagnetic Fingerprinting, Plio-Pleistocene Lavas of Renegade Canyon Area.** Magnetic polarity is indicated by solid symbols for normal, open symbols for reversed, characters for unknown polarity. The use of paleomagnetism and geochemistry allows rigorous separation of units, as indicated. RC bottoms flows are tentatively correlated with QTbr<sub>1</sub> without paleomagnetic data.

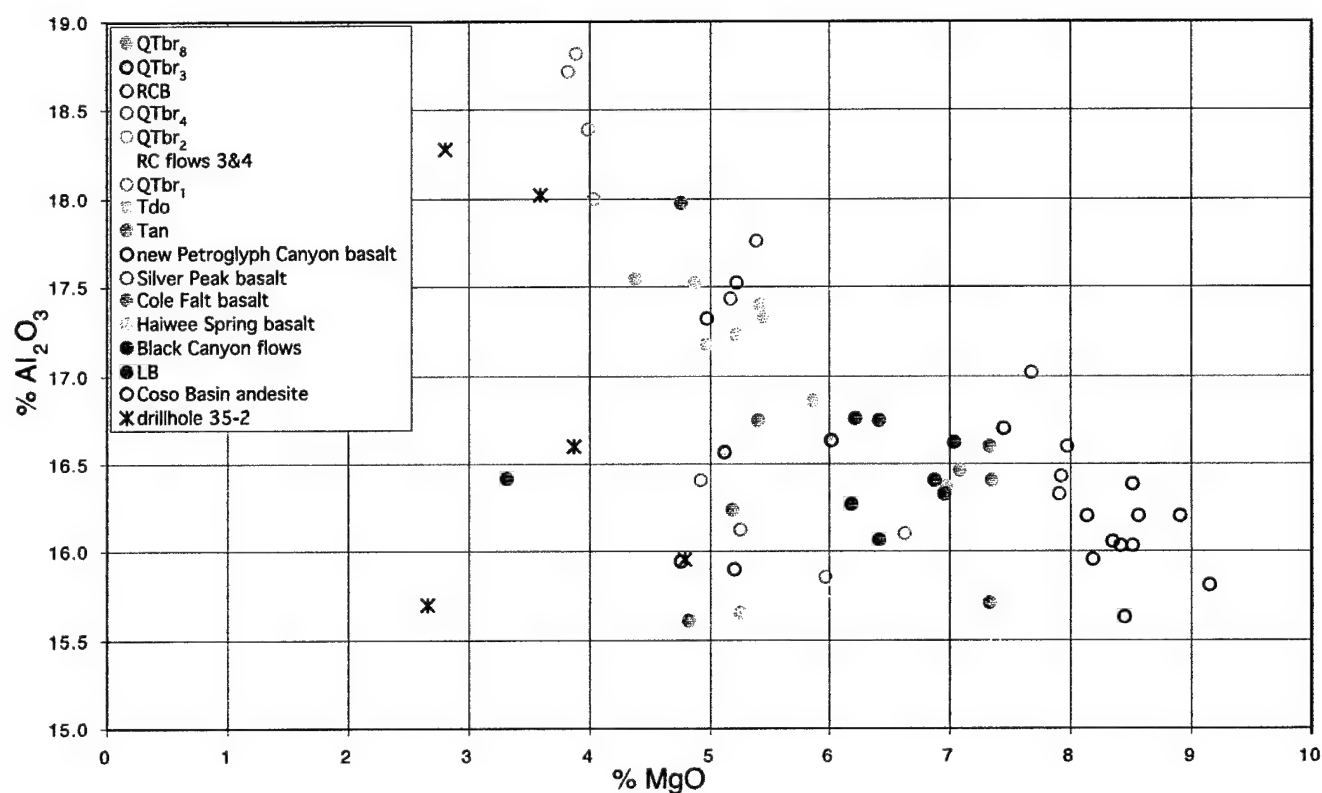




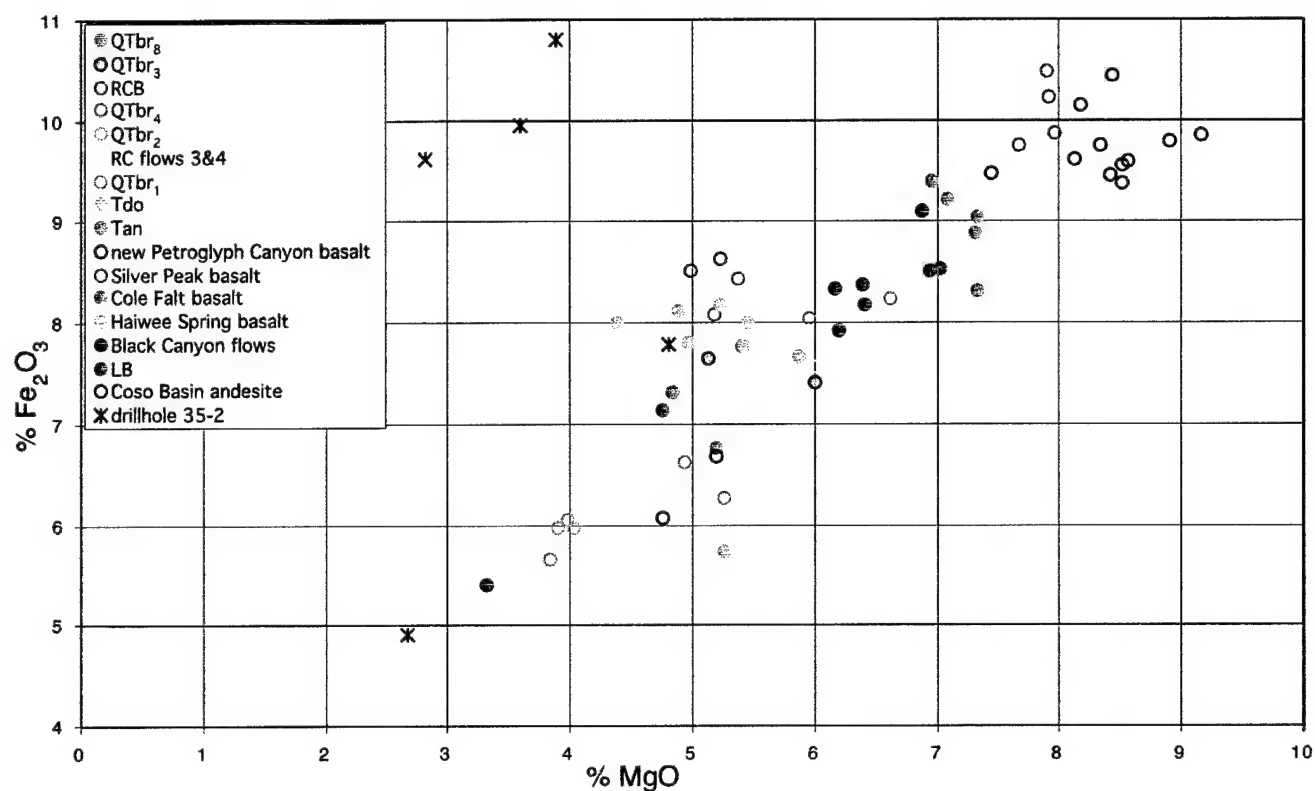
**Figure 3.9 - Combined XRF and Paleomagnetic Fingerprinting, Silica vs. Mg.** Magnetic polarity is indicated by solid symbols for normal, open or lightly filled symbols for reversed, and characters for unknown polarity. These data corroborate eruptive unit correlations except for samples deriving from drillhole 35-2 which probably have been hydrothermally altered.



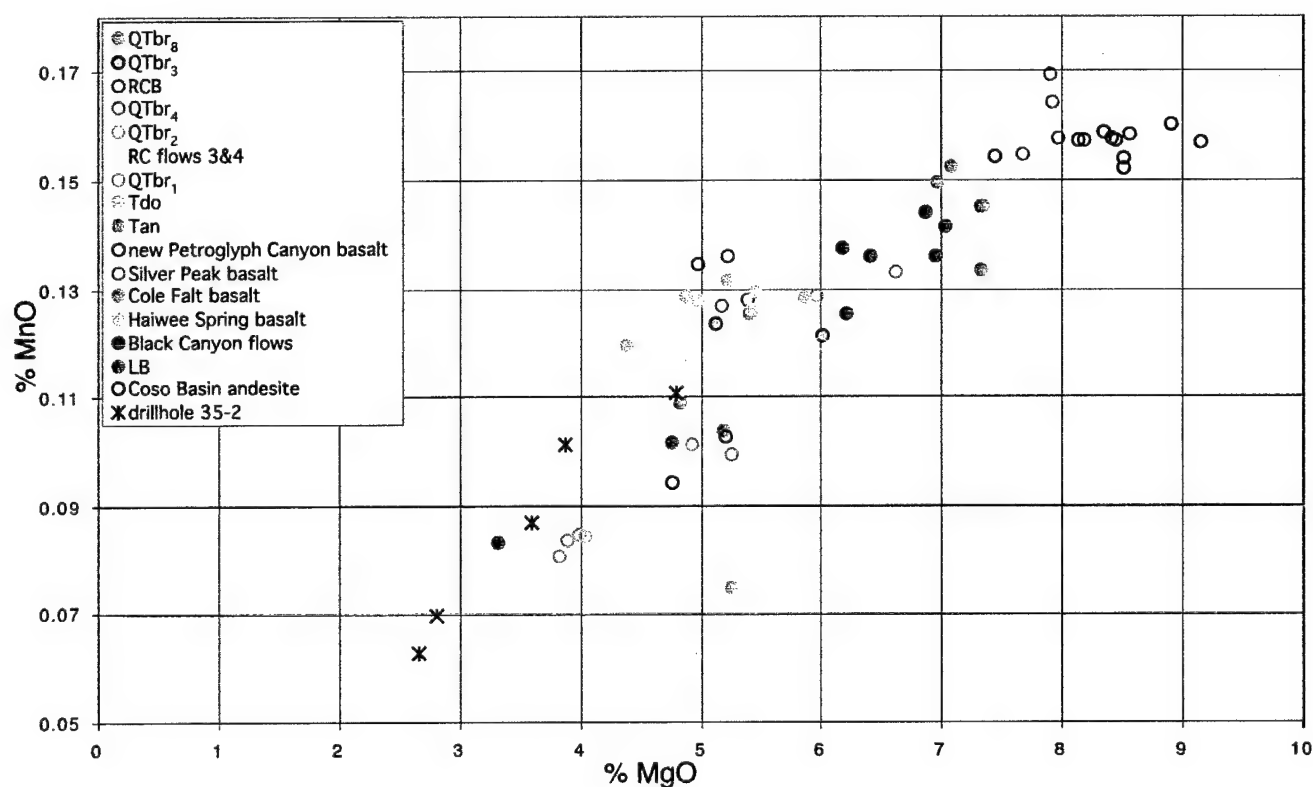
**Figure 3.10 - Combined XRF and Paleomagnetic Fingerprinting, Ti vs. Mg.** Magnetic polarity is indicated by solid symbols for normal, open or lightly filled symbols for reversed, and characters for unknown polarity. These data corroborate eruptive unit correlations except for samples deriving from drillhole 35-2 which probably have been hydrothermally altered.



**Figure 3.11 - Combined XRF and Paleomagnetic Fingerprinting, Al vs. Mg.** Magnetic polarity is indicated by solid symbols for normal, open or lightly filled symbols for reversed, and characters for unknown polarity. These data corroborate eruptive unit correlations except for samples deriving from drillhole 35-2 which probably have been hydrothermally altered.

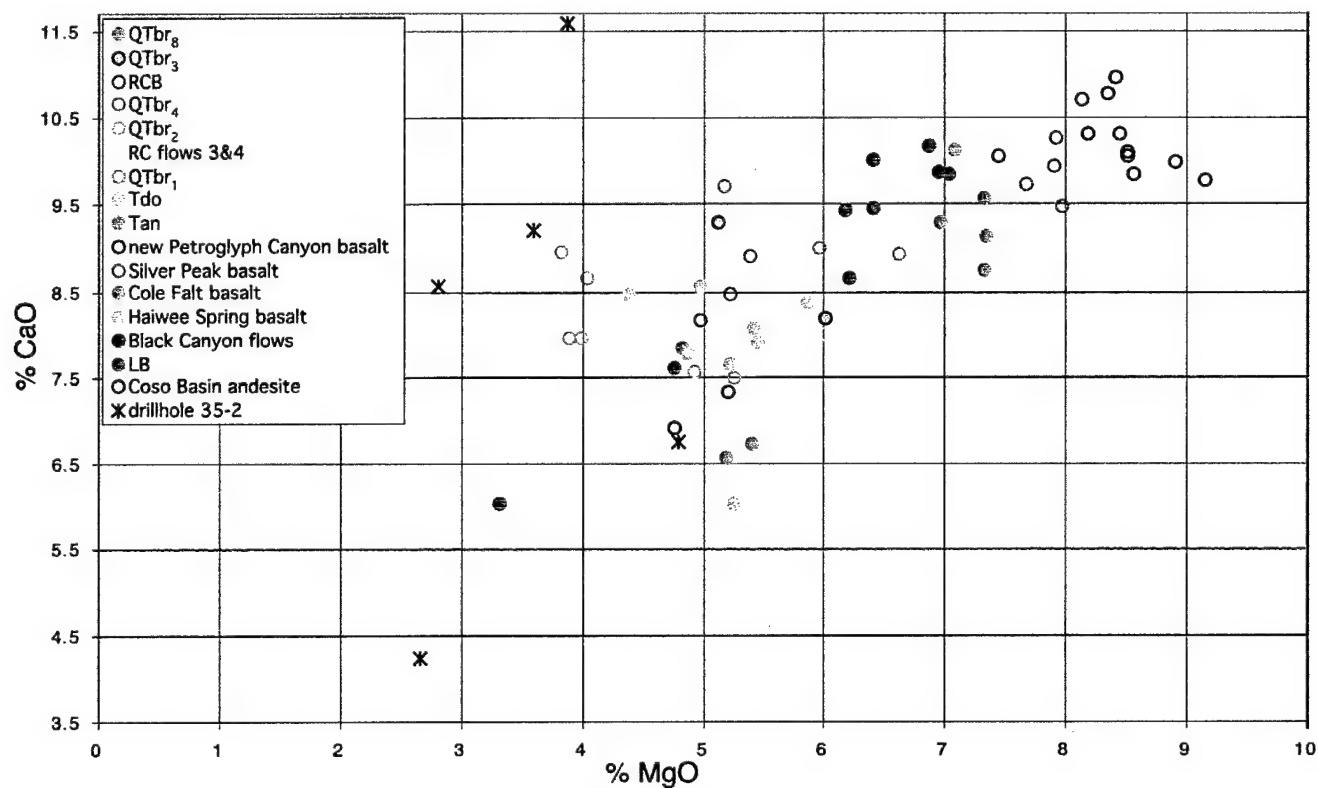


**Figure 3.12 - Combined XRF and Paleomagnetic Fingerprinting, Fe vs. Mg.** Magnetic polarity is indicated by solid symbols for normal, open or lightly filled symbols for reversed, and characters for unknown polarity. These data corroborate eruptive unit correlations except for samples deriving from drillhole 35-2 which probably have been hydrothermally altered.

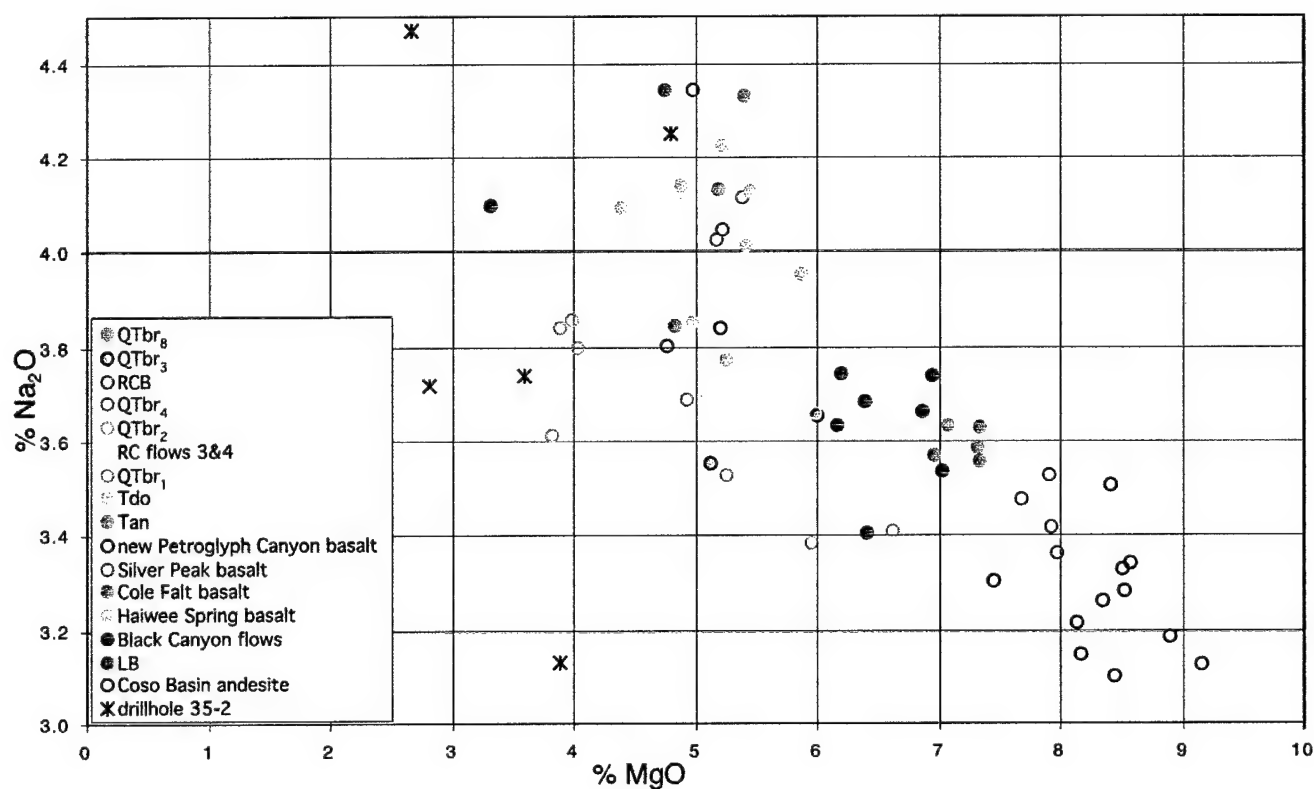


**Figure 3.13 - Combined XRF and Paleomagnetic Fingerprinting, Mn vs. Mg.** Magnetic polarity is indicated by solid symbols for normal, open or lightly filled symbols for reversed, and characters for unknown polarity. These data corroborate eruptive unit correlations except for samples deriving from drillhole 35-2 which probably have been hydrothermally altered.

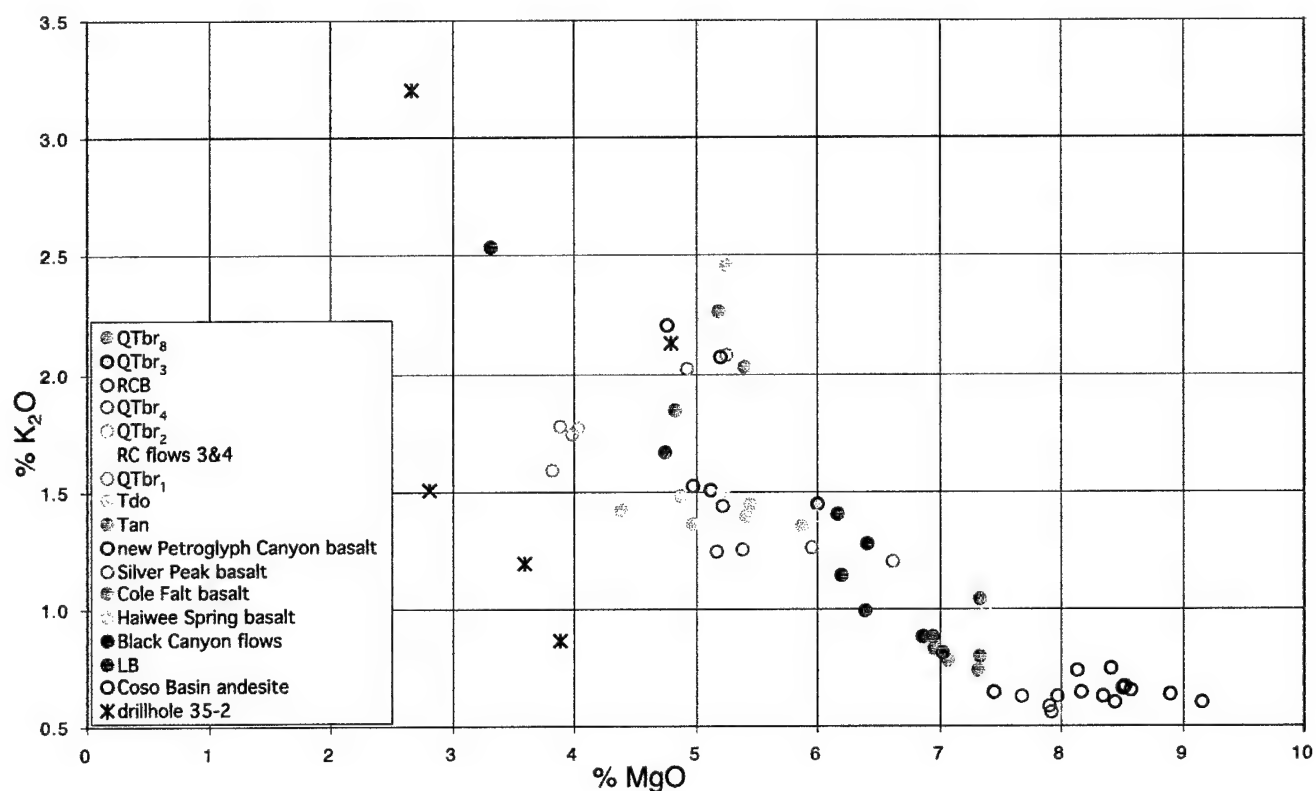




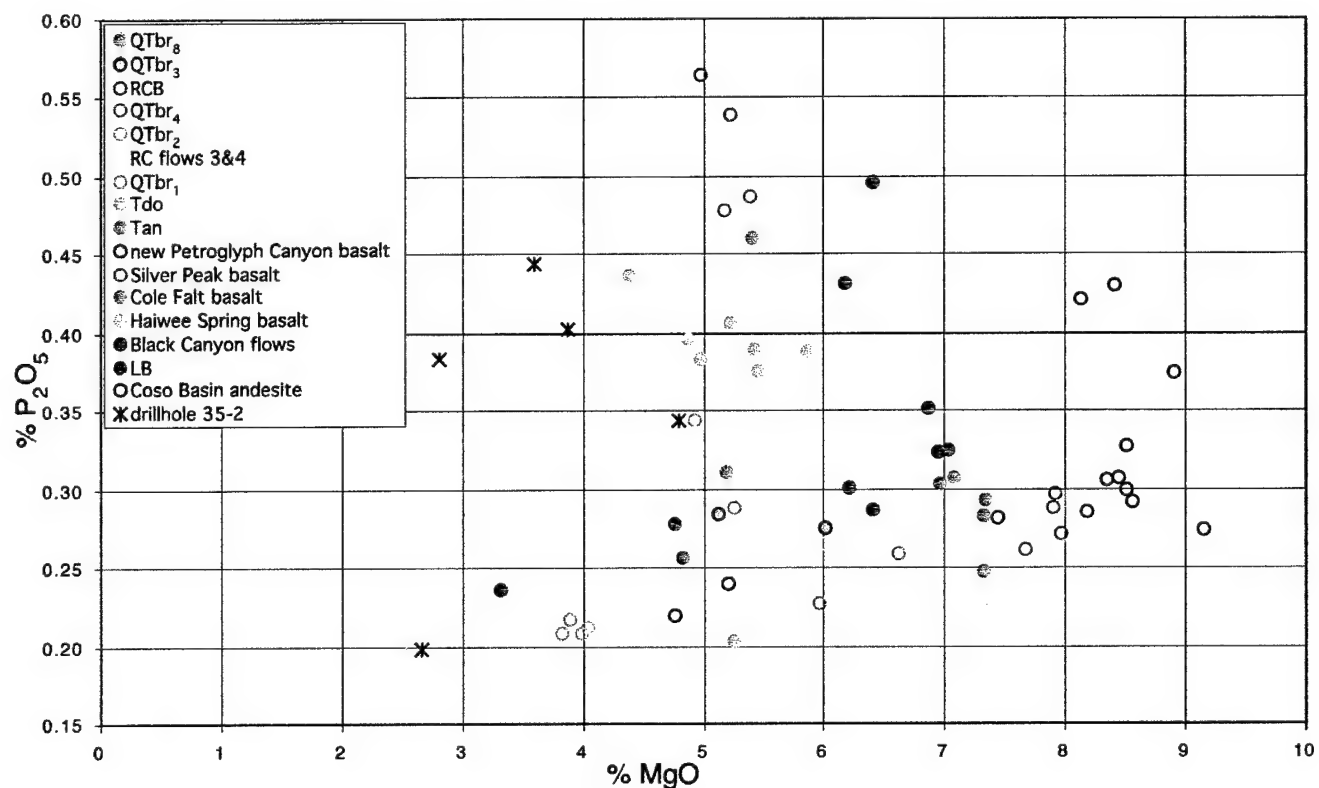
**Figure 3.14 - Combined XRF and Paleomagnetic Fingerprinting, Ca vs. Mg.** Magnetic polarity is indicated by solid symbols for normal, open or lightly filled symbols for reversed, and characters for unknown polarity. These data corroborate eruptive unit correlations except for samples deriving from drillhole 35-2 which probably have been hydrothermally altered.



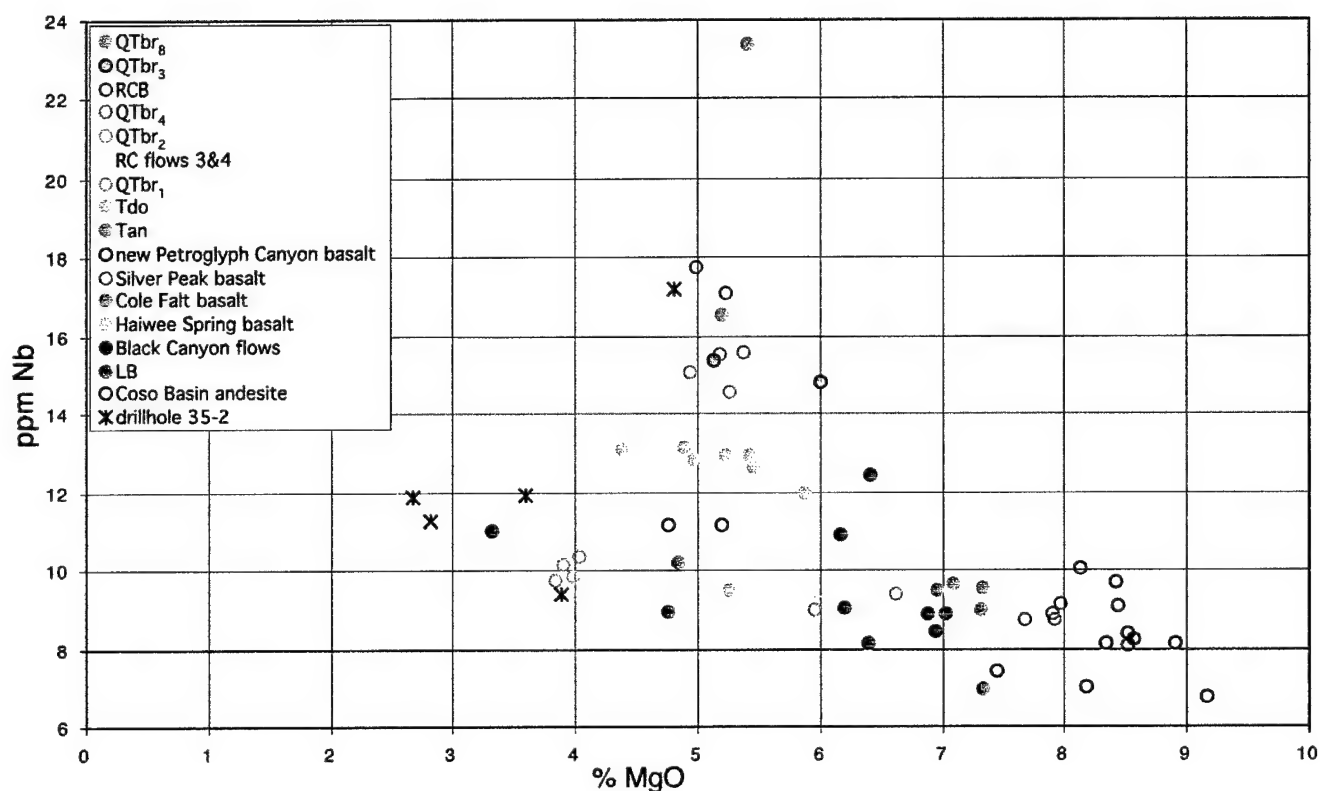
**Figure 3.15 - Combined XRF and Paleomagnetic Fingerprinting, Na vs. Mg.** Magnetic polarity is indicated by solid symbols for normal, open or lightly filled symbols for reversed, and characters for unknown polarity. These data corroborate eruptive unit correlations except for samples deriving from drillhole 35-2 which probably have been hydrothermally altered.



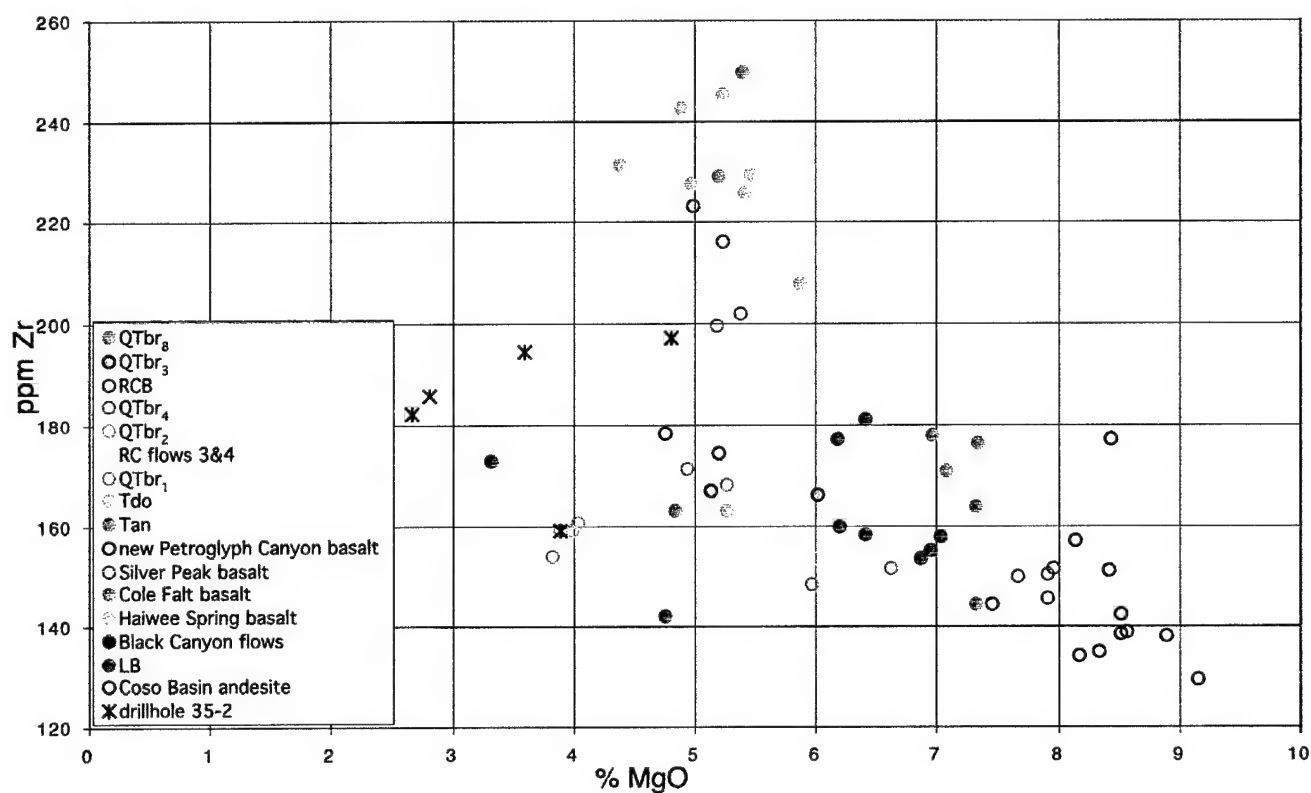
**Figure 3.16 - Combined XRF and Paleomagnetic Fingerprinting, K vs. Mg.** Magnetic polarity is indicated by solid symbols for normal, open or lightly filled symbols for reversed, and characters for unknown polarity. These data corroborate eruptive unit correlations except for samples deriving from drillhole 35-2 which probably have been hydrothermally altered.



**Figure 3.17 - Combined XRF and Paleomagnetic Fingerprinting, Phosphate vs. Mg.** Magnetic polarity is indicated by solid symbols for normal, open or lightly filled symbols for reversed, and characters for unknown polarity. These data corroborate eruptive unit correlations except for samples deriving from drillhole 35-2 which probably have been hydrothermally altered.

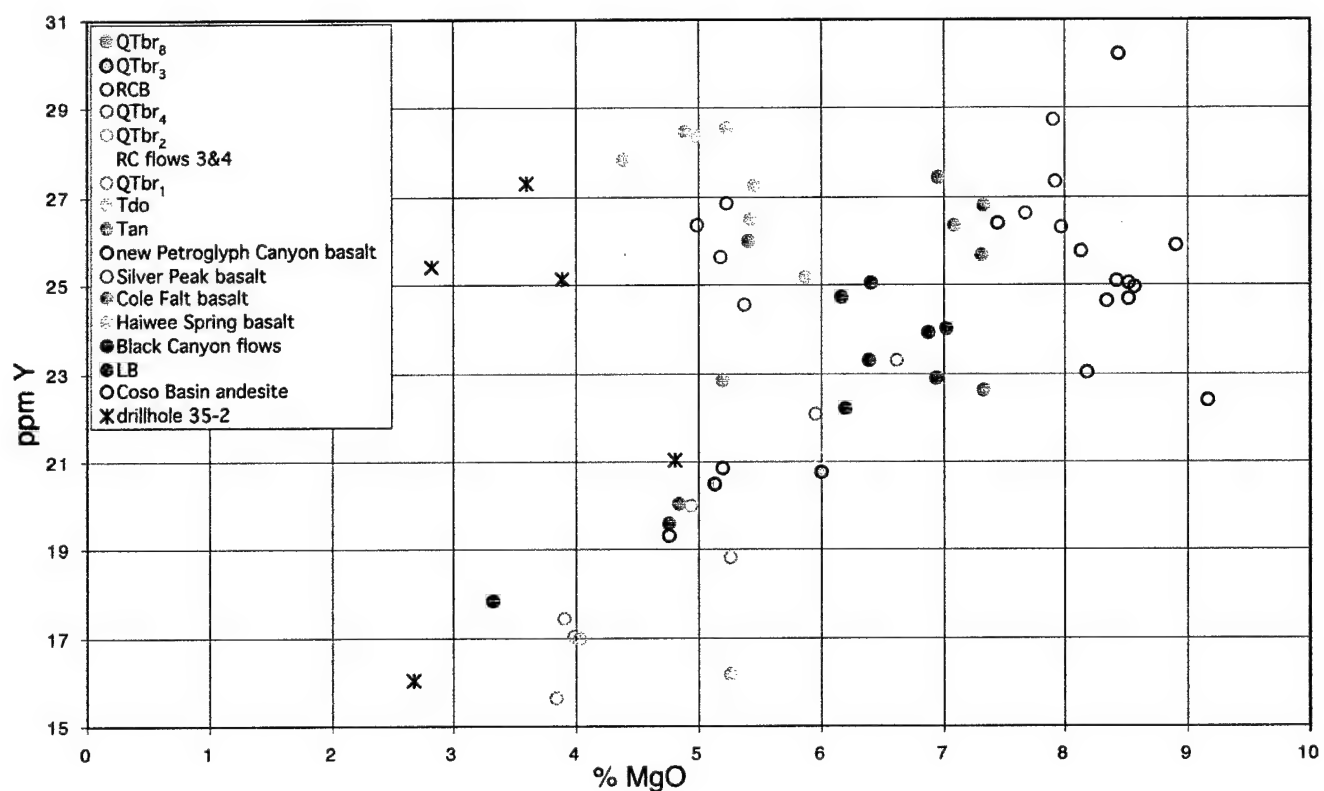


**Figure 3.18 - Combined XRF and Paleomagnetic Fingerprinting, Nb vs. Mg.** Magnetic polarity is indicated by solid symbols for normal, open or lightly filled symbols for reversed, and characters for unknown polarity. These data corroborate eruptive unit correlations except for samples deriving from drillhole 35-2 which probably have been hydrothermally altered.

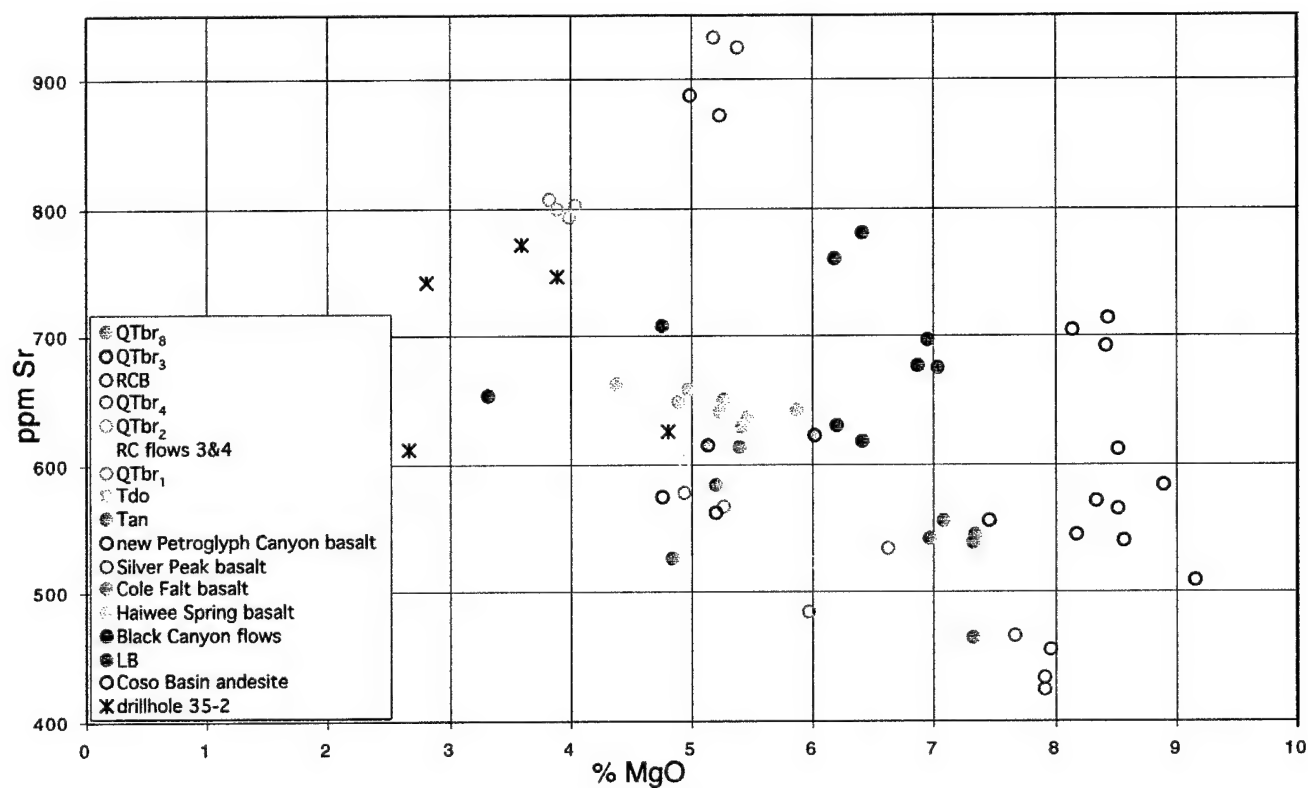


**Figure 3.19 - Combined XRF and Paleomagnetic Fingerprinting, Zr vs. Mg.** Magnetic polarity is indicated by solid symbols for normal, open or lightly filled symbols for reversed, and characters for unknown polarity. These data corroborate eruptive unit correlations except for samples deriving from drillhole 35-2 which probably have been hydrothermally altered.

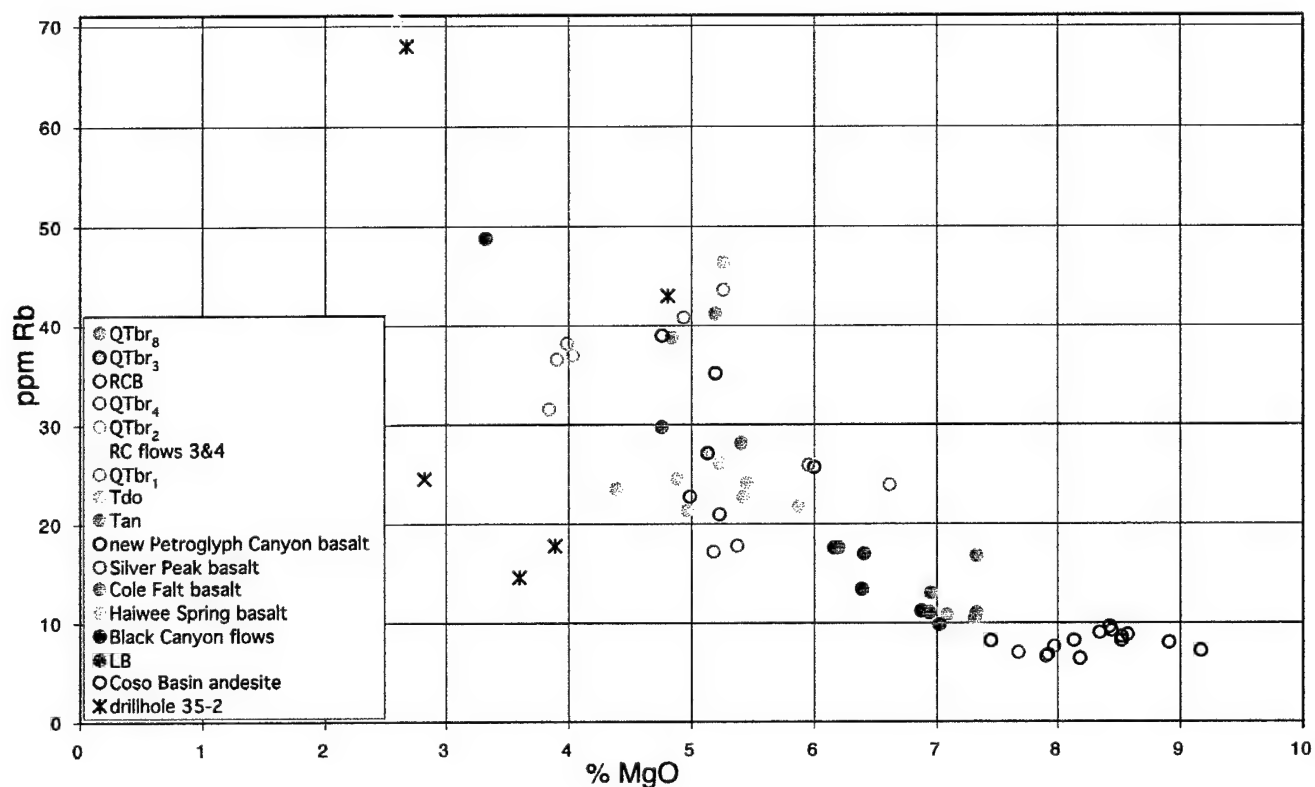




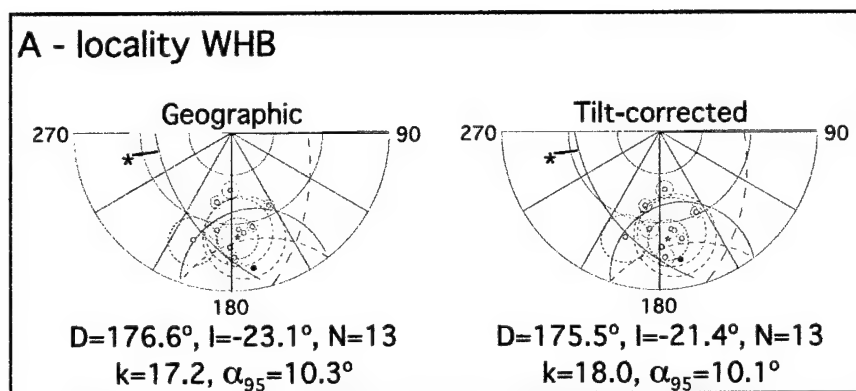
**Figure 3.20 - Combined XRF and Paleomagnetic Fingerprinting, Y vs. Mg.** Magnetic polarity is indicated by solid symbols for normal, open or lightly filled symbols for reversed, and characters for unknown polarity. These data corroborate eruptive unit correlations except for samples deriving from drillhole 35-2 which probably have been hydrothermally altered.



**Figure 3.21 - Combined XRF and Paleomagnetic Fingerprinting, Sr vs. Mg.** Magnetic polarity is indicated by solid symbols for normal, open or lightly filled symbols for reversed, and characters for unknown polarity. These data corroborate eruptive unit correlations except for samples deriving from drillhole 35-2 which probably have been hydrothermally altered.



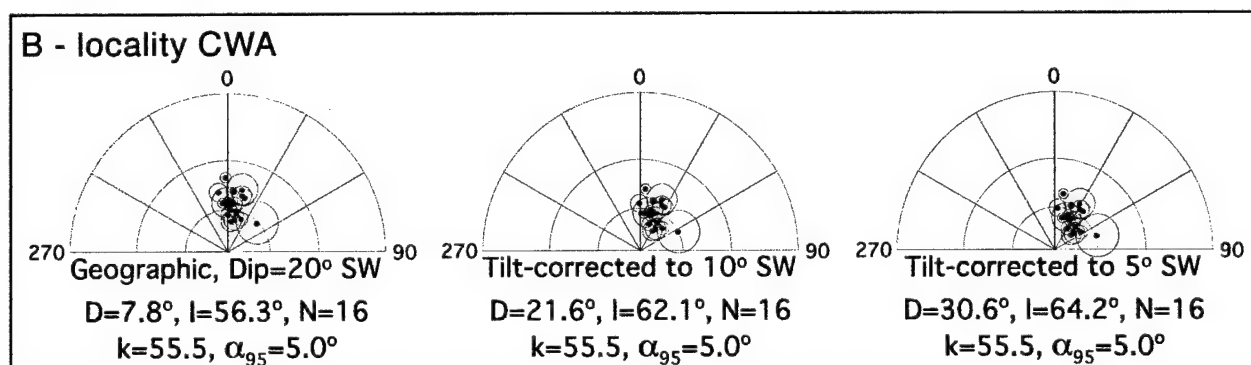
**Figure 3.22 - Combined XRF and Paleomagnetic Fingerprinting, Rb vs. Mg.** Magnetic polarity is indicated by solid symbols for normal, open or lightly filled symbols for reversed, and characters for unknown polarity. These data corroborate eruptive unit correlations except for samples deriving from drillhole 35-2 which probably have been hydrothermally altered.

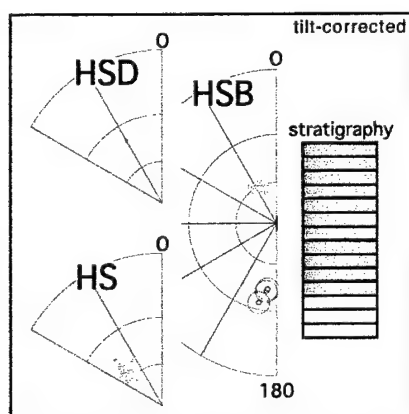


**Figure 3.23 - Mean Directions of Sedimentary Localities** shown with blue stars. A. WHB locality is not rotated within the rather large  $\alpha_{95}$ . Thus additional work may yet reveal significant rotation. B. Two possible tilt corrections necessary to restore CWA fanglomerate to its original dip are depicted. In either case a clockwise vertical-axis rotation is revealed.

- Down inclination with  $\alpha_{95}$   
 ⊙ Up inclination with  $\alpha_{95}$

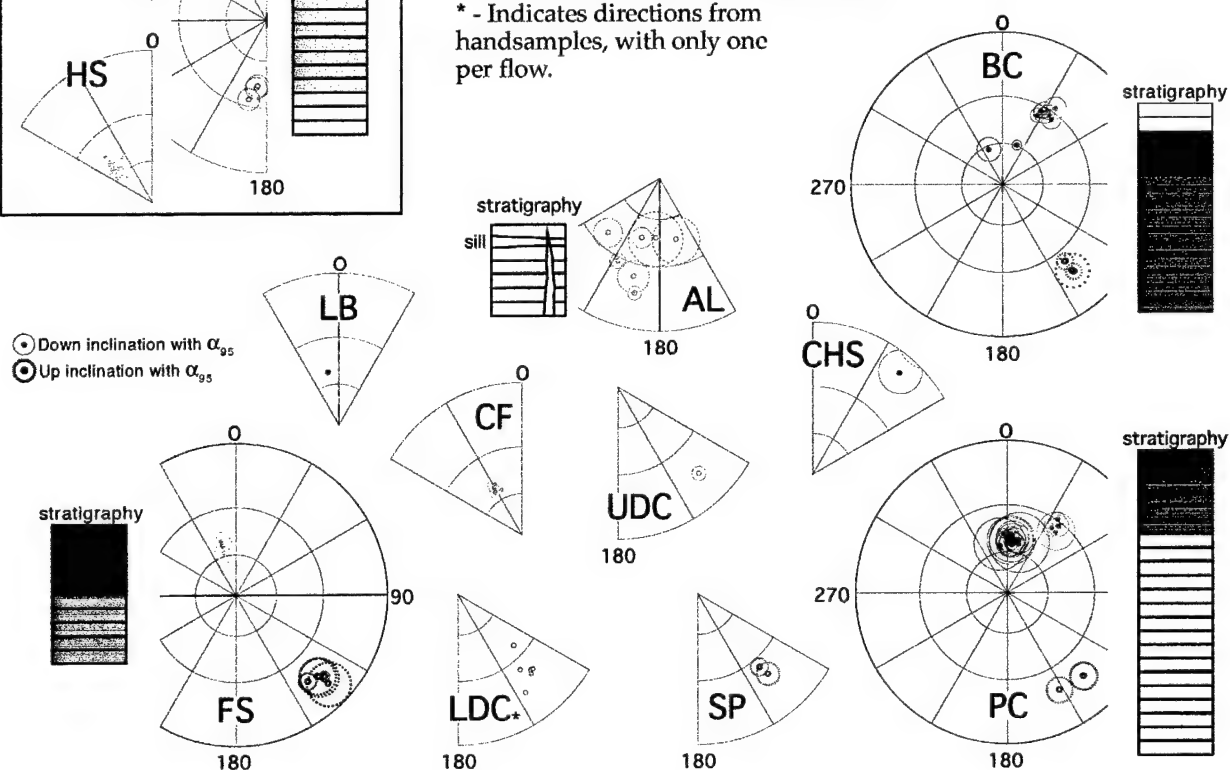
\* - Great circle fit to demag path of one sample that never reaches a stable endpoint

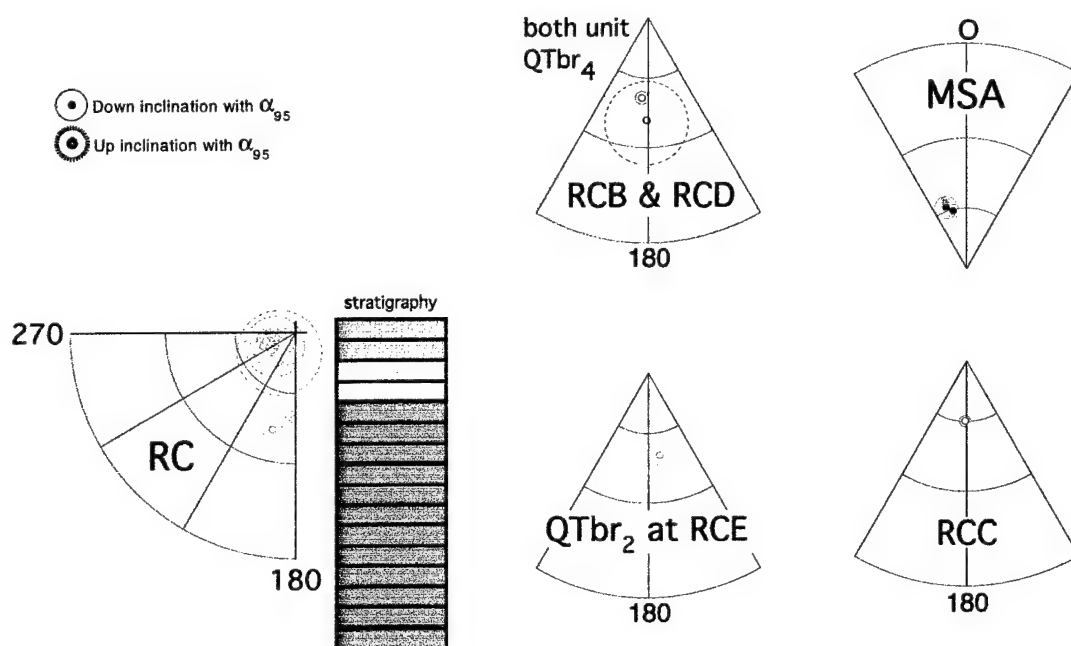




**Figure 3.24 - Paleomagnetic Remanence and Stratigraphy of Units ~3-3.6 Ma.** Depicted are mean ChRMs for each lava flow sampled. For localities exhibiting a stratigraphy exhibiting more than one eruptive unit, stratigraphy is shown to indicate eruptive order. Stratigraphy and directions are colored to indicate likely correlation based on direction or geographic region (HS localities) alone. Directions are not tilt-corrected unless noted.

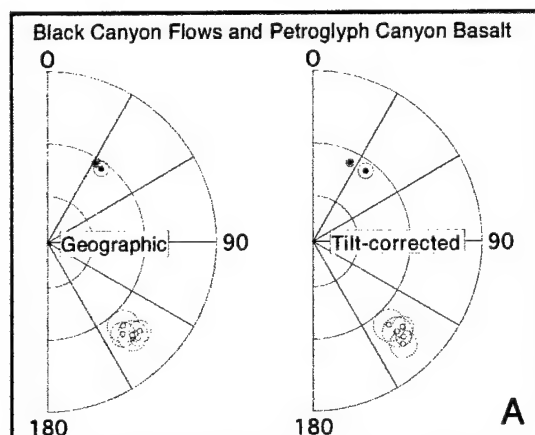
\* - Indicates directions from hand samples, with only one per flow.





**Figure 3.25 - Paleomagnetic Remanence and Stratigraphy of Renegade Canyon Area Units.** Depicted are mean ChRMs for each lava flow sampled. For localities exhibiting a stratigraphy exhibiting more than one eruptive unit, stratigraphy is shown to indicate eruptive order. Stratigraphy and directions are colored to indicate correlation based on geochemistry presented in this report. Directions are not tilt-corrected.

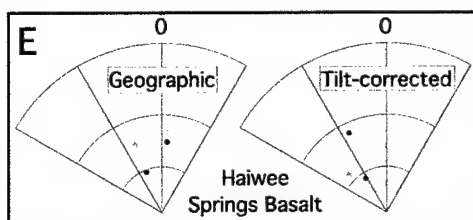
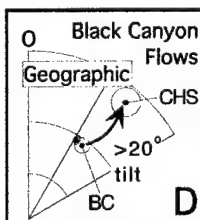
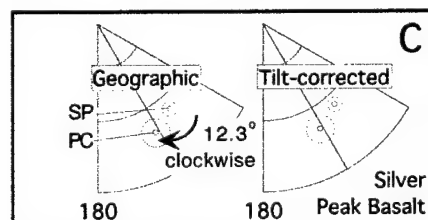
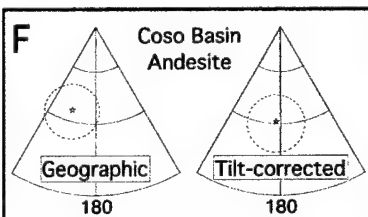
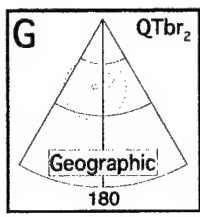
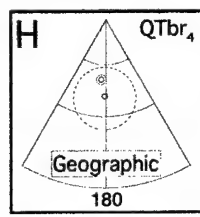
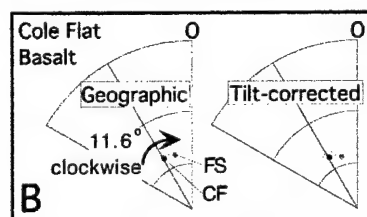


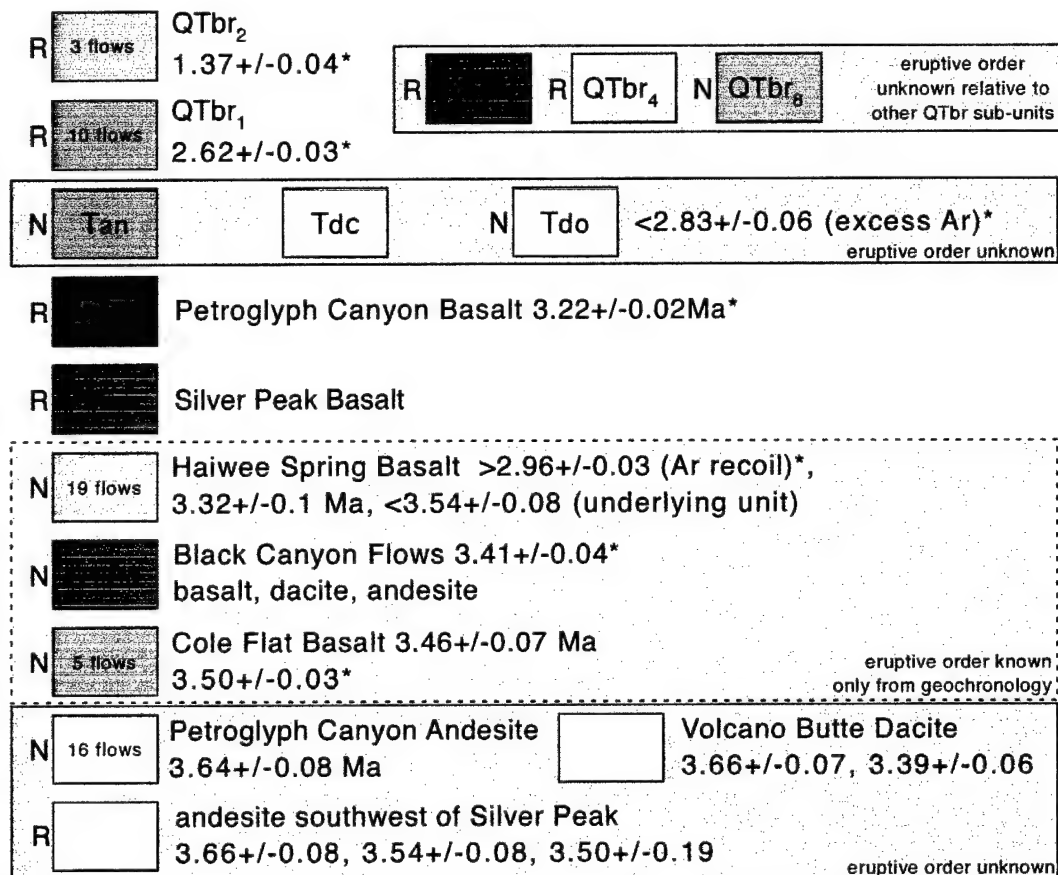


**Figure 3.26 - Measures of Rotation from Lavas.** Eruptive unit mean directions are averaged within locality and unit. In all cases except F, geographic coordinates are preferred because of original dips of lava flows (e.g. note increased scatter in A, tilt-corrected). (A) Localities within Wild Horse Mesa are not rotated relative to one another. (B&C) Localities within Wild Horse Mesa are rotated relative to Cole Flat area. (D) CHS is tilted relative to Wild Horse Mesa. (E) Results suggesting unaccounted-for, large original dips. (F) The shallow inclination suggests that secular variation is not fully averaged. (G&H) No discernable rotation. No tilt-correction is available for these latter two groups of localities.

○ Down inclination with  $\alpha_{95}$

⊙ Up inclination with  $\alpha_{95}$

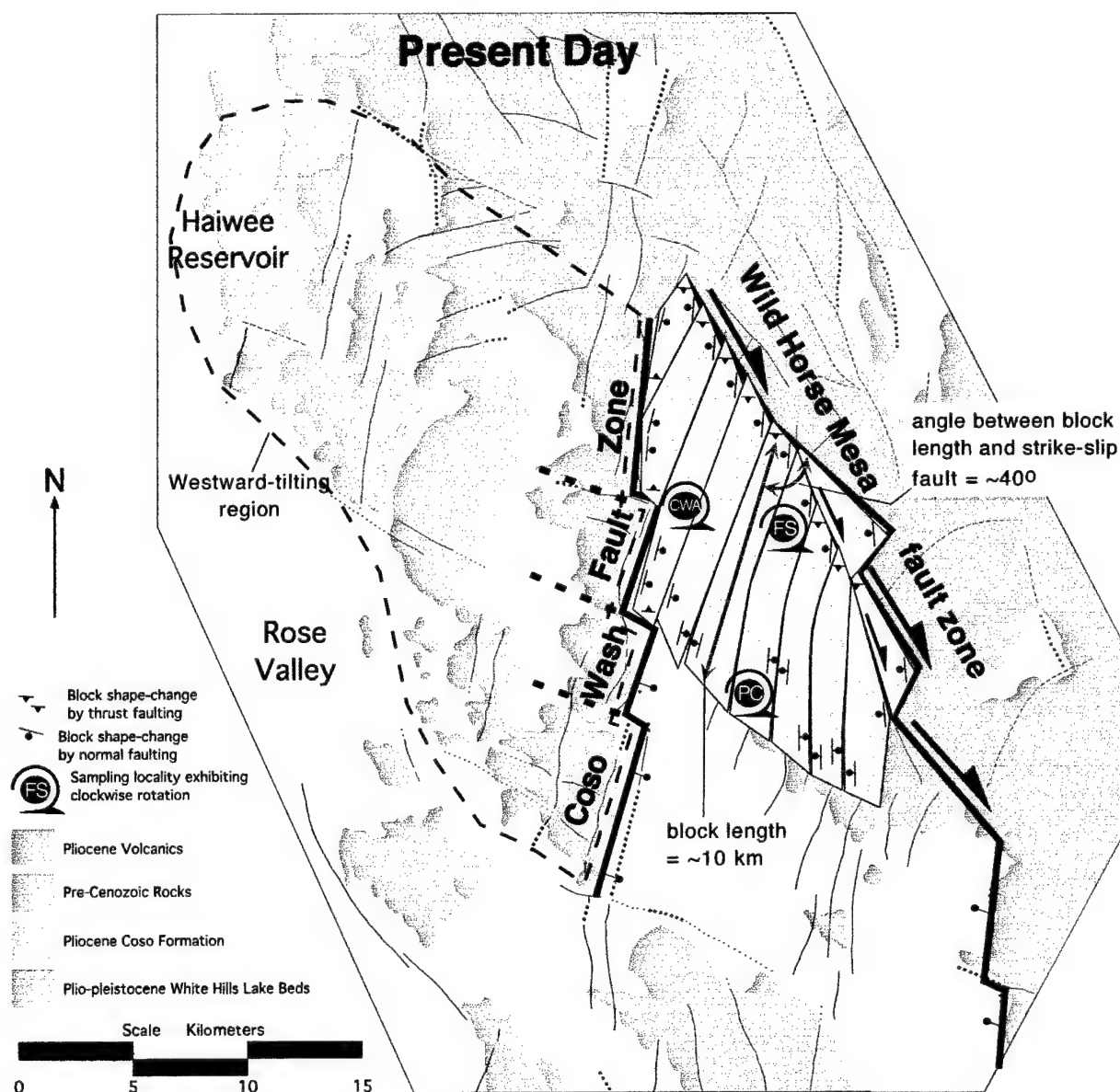




\* Ar/Ar presented here, with 2  $\sigma$  error. All other geochronology - K/Ar by Duffield et al., 1980. Polarity: R - reversed, N - normal.

**Figure 3.27 - Volcano-stratigraphy of the Study Area.** Combined use of stratigraphic relations, geochronology, and paleomagnetic polarity reveals this sequence of major eruptive units. Some minor units are not included. Color scheme matches that used in other figures.

**Figure 4.1 - Rotated Blocks of Wild Horse Mesa.** This cartoon depicts approximate boundaries of the greater Wild Horse Mesa; the Coso Wash fault zone and the newly named Wild Horse Mesa fault zone. Enclosed are blocks oriented obliquely to both boundaries which have rotated about 12°-20° clockwise. Three localities for which we have direct measures of rotation are shown. Boundaries between blocks are likely sinistral-normal faults. Block boundaries curve to more north-south orientations towards the south causing a space problems and additional east and west vergent normal faulting. In our model block shapes change to accomodate space problems. Likely shape change is indicated at block corners. This explains the observation of thrust faults in the slickenline data.



### Slip Calculations from Finite Rotation Measurements

#### Assumptions;

- block ends are pinned to the boundary faults
- block length does not change
- block corners change shape to accommodate space problems
- Wild Horse Mesa fault zone does not change shape or rotate

It follows that the change in length of the block projected along the dextral fault is the strike-slip displacement accommodated by rotation.

$L$  = block length

$\theta$  = angle between dextral fault and block long axis at 3 Ma

$R$  = angle of rotation of blocks

$\theta+R$  = angle between dextral fault and block long axis at present

$P$  = projected block length

Strike slip displacement =  $P_{\text{initial}} - P_{\text{now}}$

$P_{\text{initial}} = L \times \cos(\theta)$

$P_{\text{now}} = L \times \cos(\theta+R)$

Therefore,  
strike-slip displacement  
=  $L[\cos(\theta) - \cos(\theta+R)]$

Assuming blocks originally parallel to the dip-slip boundary fault, net opening of the basin =  $L \times \sin(R)$

Thus, for a pinned block model, using a block length of 10 km and other values as indicated:  
dextral slip (minimum) = 1.5 km      net opening (minimum) = 2 km

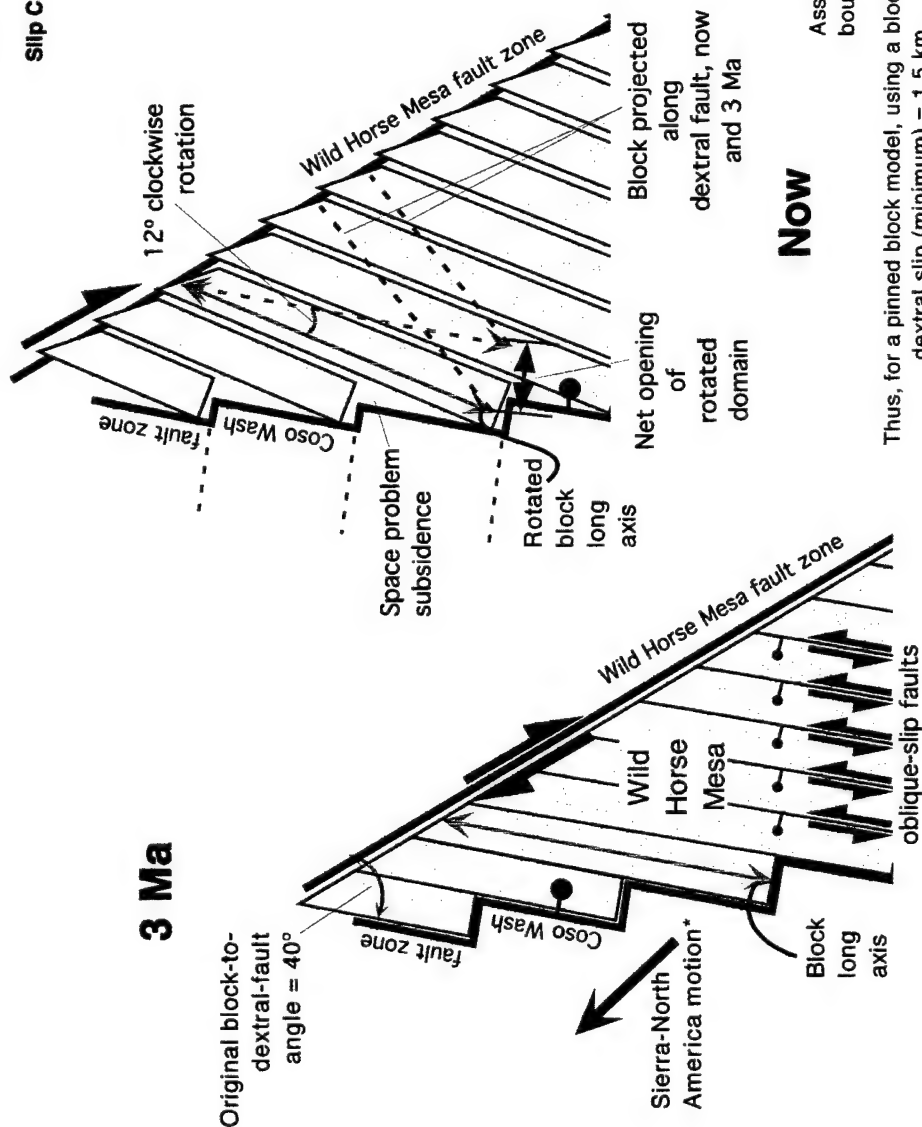


**Figure 4.2 - Kinematic Model of the Wild Horse Mesa.** This unconventional model that attempts to address non-parallel bounding faults. The grey fault blocks of the Wild Horse Mesa accommodate relative motion between two boundary faults. Results of this accommodation include (1) 12° of clockwise block rotation, (2) dextral slip of about 1.5 km parallel to the Wild Horse Mesa fault zone (3) normal faulting along Coso Wash fault zone and shape change of this boundary (4) basin opening almost perpendicular to Coso Wash fault zone of 2 km distributed between the basin boundary faults and inter-block faults (5) sinistral-normal faulting between blocks (6) space problems throughout causing block-shape changes by exhumation of footwalls along block boundaries and intra-block deformation (as evidenced by thrust faulting, see text). Basin opening is calculated perpendicular to the Coso Wash fault zone because this is apparently the largest single structure accommodating said opening. \* - from Dixon et al., 2000

### References Cited

- Bacon, C. R., Giovannetti, D. M., Duffield, W. A., Dalrymple, G. B. & Drake, R. E., 1982, Age of the Coso formation, Inyo County, California, 18.
- Cogne, J. P., 2003, PaleoMac: a MacIntosh application for treating paleomagnetic data and making plate reconstructions. *Geochemistry, Geophysics, Geosystems* 4(1), 1007.
- Demarest, H. H., Jr., 1983, Error analysis for the determination of tectonic rotation from paleomagnetic data. *JGR. Journal of Geophysical Research. B* 88(5), 4321-4328.
- Dewey, J. F., 2002, Transtension in Arcs and Orogens, In: *International Geology Review* 44, V. H. Winston & Sons, Inc., Silver Spring, MD, 402-439.
- Dixon, T. H., Miller, M., Farina, F., Wang, H. & Johnson, D., 2000, Present-day motion of the Sierra Nevada block and some tectonic implications for the Basin and Range province, North America Cordillera, *Tectonics*, 19(1), 1-24.
- Duffield, W. A., Bacon, C. R. & Dalrymple, G. B., 1980, Late Cenozoic volcanism, geochronology, and structure of the Coso Range, Inyo County, California, *Journal of Geophysical Research*, 85, 2381-2404.
- Lewis, J. C., Unruh, J. R. & Twiss, R. J., 2003, Seismogenic strain and motion of the Oregon coast block, *Geology*, 31(2), 183-186.
- Monastero, F. C., 1997, Evidence for a nascent metamorphic core complexes at the Coso geothermal area, California, *Eos, Transactions of the American Geophysical Union*, 78(46), F659.
- Monastero, F. C., Walker, J. D., Katzenstein, A. M. & Sabin, A. E., 2002, Neogene evolution of the Indian Wells Valley, east-central California, In: *Geologic Evolution of the central Mojave Desert and southern Basin and Range* (edited by Glazner, A. F., Walker, J. D. & Bartley, J. M.), Memoir 195, Geological Society of America, Boulder, Colorado.
- Twiss, R. J., Protzman, G. M. & Hurst, S. D., 1991, Theory of slickenline patterns based on the velocity gradient tensor and microrotation, *Tectonophysics*, 186, 215-239.
- Twiss, R. J., Souter, B. J. & Unruh, J. R., 1993, The effect of block rotations on the global seismic moment tensor and the pattern of P and T axes, *Journal of Geophysical Research*, 98(B1), 645-674.
- Unruh, J., Humphrey, J. & Barron, A., 2003, Transtensional model for the Sierra Nevada frontal fault system, eastern California, *Geology*, 31, 327-330.
- Unruh, J. R., Hauksson, E., Monastero, F. C., Twiss, R. J. & Lewis, J. C., 2002, Seismotectonics of the Coso Range-Indian Wells Valley region, California: Transtensional deformation along the southeastern margin of the Sierra Nevada microplate, In: *Geologic Evolution of the central Mojave Desert and southern Basin and Range* (edited by Glazner, A. F., Walker, J. D. & Bartley, J. M.), Memoir 195, Geological Society of America, Boulder, Colorado, 277-294.
- Unruh, J. R. & Twiss, R. J., 1998, Coseismic growth of basement-involved anticlines: the Northridge-Laramide connection, *Geology*, 26(4), 335-338.
- Unruh, J. R., Twiss, R. J. & Hauksson, E., 1996, Seismogenic deformation field in the Mojave block and implications for tectonics of the eastern California shear zone, *Journal of Geophysical Research*, 101(B4), 8,335-8,361.
- Wells, R. E., Simpson, R. W., Bentley, R. D., Beeson, M. H., Mangan, M. T. & Wright, T. L., 1989, Correlation of Miocene flows of the Columbia River Basalt Group from

the central Columbia River Plateau to the coast of Oregon and Washington.  
*Special Paper - Geological Society of America* 239, 113-129.

Whitmarsh, R. S., 1996, A geologic map of the Coso Range, with supplemental U-Pb geochronology and Ar-Ar thermochronology. In: *Abstracts with Programs - Geological Society of America* 28, 123-124.

Whitmarsh, R. S., Walker, J. D., Monastero, F. C., 1996, Mesozoic and Cenozoic structural framework of the Coso Range and adjacent areas of eastern California. In: *Abstracts with Programs - Geological Society of America* 28, 124.

Whitmarsh, R. W., Walker, J. D., Monastero, F. C., 1996, Structural domains within the Coso Range of east-central California; a case for right-oblique extension. In: *Abstracts with Programs - Geological Society of America* 28, 116.



## Appendix A

### Supplementary Geochemical Data: V, Ni, Cr

Eruptive Unit Locality /Flow #	Cole Flat Basalt		Petroglyph Canyon Basalt													
	FS Flow 8	Mean	FS Flow 12	Mean	PC Flow 22	Mean	BC Flow 6	Mean	FS Flow 2	Mean	FS Flow 3	Mean	FS Flow 14	Mean	FS Flow 4	Mean
Sample ID	BD0802B		BD1202B		PC2206A		99BC0603A		BD0201C		BD0303B		BD1401C		BD0403B	
Ni	81.95		85.53		120.90		130.85		150.13		134.48		146.13		135.06	
standard dev.	1.77		0.51		0.80		2.95		2.01		3.42		1.32		0.59	
Cr	195.87		192.10		212.67		275.82		292.86		254.40		291.64		219.21	
standard dev.	1.59		3.83		0.57		8.51		15.33		12.36		7.11		6.80	
V	177.81		181.49		178.56		174.73		170.94		179.03		167.68		167.89	
standard dev.	0.51		2.48		0.79		0.59		0.05		1.59		0.36		9.92	

Eruptive Unit		Silver Peak Basalt			Black Canyon Flows								Coso Basin Andesite			
Locality /Flow #		SP Flow 1	Mean	PC flow 21	Mean	CHS Site 1	Mean	PC Flow 19	Mean	BC Flow 10	Mean	BC Flow 12	Mean	BC Flow 18	Mean	AL Flow 3
Sample ID		SP0107A		PC2108A		CHS0103A		PC1907A		BC1003A		BC12		BC1806A		AL0303B
Ni		111.71		111.62		65.34		68.17		58.58		30.33		66.89		52.06
standard dev.		0.71		0.01		0.29		4.12		4.06		0.21		0.23		2.83
Cr		170.22		190.67		195.36		184.54		158.66		66.02		126.79		160.20
standard dev.		6.66		9.86		3.47		4.57		3.98		0.30		3.13		5.54
V		193.49		174.78		166.68		174.80		153.95		90.24		180.38		122.14
standard dev.		0.67		1.23		0.19		0.59		0.94		1.35		2.05		0.85

## Appendix B

### $^{40}\text{Ar}/^{39}\text{Ar}$ Geochronology Data

Analytical methods5 fresh volcanic rocks were chosen for  $^{40}\text{Ar}/^{39}\text{Ar}$  geochronology HS-19, Tdo, RC-14, RC-01 and BC-18. Rocks were crushed and sieved, selected fraction were washed in water and in an ultrasonic cleaner. Using mesh 40-60 (230 to 380  $\mu\text{m}$ ) fraction, phenocrysts of olivine were removed after four passes through a magnetic separator operating from 0.5 to up to 1.7A. The presence of quartz in the final passes indicates the presence of xenocrysts in most of the rocks, which have basaltic composition (e.g. HS-19, RC-01 and BC-18). In order to avoid the spurious effects of possible plagioclase xenocrysts we have separated the groundmass. This groundmass is mainly composed of fine laths of plagioclase (20-50  $\mu\text{m}$ ) and pyroxenes. Transparent plagioclase phenocrysts from the same samples were also concentrated by magnetic separation. Quartz and plagioclase were separated from the non-magnetic part using heavy liquid (lithium metatungstate adjusted at density = 2.645). 35 to 75 mg groundmass and plagioclase samples were loaded in four Al disks as described by Renne et al. (1998) and irradiated for 30 minutes in the CLICIT facility of the TRIGA reactor at Oregon state University. After irradiation 25mg of plagioclase and 90 grains of groundmass for each sample were degassed with a defocused argon laser (Synrad) then analyzed with a MAP 215C mass spectrometer at the Berkeley Geochronology Center using methods described by Renne et al. (1998).

Procedural blanks were measured between every two or three steps and typical values were  $(3.3 \pm 0.5) \times 10^{-16}$  for  $^{40}\text{Ar}$ ,  $(2.3 \pm 1.0) \times 10^{-18}$  for  $^{39}\text{Ar}$ ,  $(5.3 \pm 1.0) \times 10^{-19}$  for  $^{38}\text{Ar}$ ,  $(6.6 \pm 1.0) \times 10^{-18}$  for  $^{37}\text{Ar}$ ,  $(2.26 \pm 0.3) \times 10^{-18}$  for  $^{36}\text{Ar}$ . Neutron fluence (J) was monitored by Fish Canyon sanidine (FCs: 28.02 Ma, Renne et al. (1998)) grains in four positions in the Al disk. The J value for each disk was determined from individual analyses of 6 separate FCs grains in each position fused with the  $\text{CO}_2$  laser (total of 24 grains). The corresponding J values calculated with the total decay constant of Steiger and Jäger (1977) are  $0.0001376 \pm 0.0000007$  for Tdo and HS-19 plagioclases,  $0.0001371 \pm 0.0000010$  for BC18, RC-01 and RC-14 plagioclases,  $0.0001377 \pm 0.00000006$  for Tdo and HS-19 for groundmass grains,  $0.0001378 \pm 0.00000007$  for BC18, RC-01 and RC-14 groundmass grains. These J values were calculated excluding age uncertainties on the FCs and the decay constant. Mass discrimination was monitored by automated analysis air pipettes, interspersed with the unknowns was  $1.0641 \pm 0.0026$  ( $2\sigma$  error) per mass atomic unit. Nucleogenic production ratios from K and Ca were  $(^{38}\text{Ar}/^{39}\text{Ar})_{\text{K}} = (1.22 \pm 0.01) \times 10^2$ ,  $(^{38}\text{Ar}/^{37}\text{Ar})_{\text{Ca}} = (2.19 \pm 0.35) \times 10^5$ . Plateau ages are defined as comprising three continuous steps corresponding to a least 50% of the total  $^{39}\text{Ar}$  released. The individual fraction ages should agree to within  $2\sigma$  of the 'integrated' age of the plateau segment.

## Results

**Groundmass:** Figures 1-5 show the  $^{40}\text{Ar}/^{39}\text{Ar}$  incremental heating and  $^{37}\text{Ar}_{\text{Ca}}/^{39}\text{Ar}_{\text{K}}$  ratio spectra and inverse isochron plots obtained for the five samples.

**HS-19:** The spectrum is discordant and displays a dome shape. This spectrum is characterized by rising ages that reach old apparent ages. The last 35 % of the spectrum correspond to lower constant ages. Well known mechanisms that produce discordant spectra in such material is recoil of  $^{39}\text{Ar}$  during irradiation (Huneke and Smith, 1976; Forland et al., 1993; Sharp et al., 1996). In the summit of the spectrum (older apparent age) plagioclases are the main reservoir of  $^{39}\text{Ar}$ . As a consequence, older ages are found when plagioclases degas unsupported  $^{40}\text{Ar}^*$  (Sharp et al., 1996) which correspond to intermediate temperature. The  $^{39}\text{Ar}$  released at higher temperatures, principally from

pyroxene (higher Ca/K ratio, see Fig. B1), without corresponding  $^{40}\text{Ar}^*$  result in low apparent ages. In short this spectrum shape is due to the partial redistribution of the  $^{39}\text{Ar}$  from the plagioclase to pyroxenes during the irradiation.

Sample Tdo displays a saddle-shaped spectrum (Fig B2). Such spectra are characteristic of rocks that contain excess  $^{40}\text{Ar}$  (Dalrymple et al., 1975). This sample has an isotope correlation diagram that indicates a trapped  $^{40}\text{Ar}/^{36}\text{Ar}$  ratio of  $379 \pm 6$ . This ratio is higher than that of atmospheric at the 95 % confidence level, confirming the presence of excess argon. This excess argon is generally interpreted in lavas flow as the result of incomplete degassing of magmatic Argon (Sharp et al., 1996). We interpret the inverse isochron age,  $2.83 \pm 0.02$  Ma, as the maximum age for the Tdo sample.

RC-14 display a less disturbed spectrum that, after a slight decrease of the apparent ages in the first degassing steps displays a very flat spectrum yielding a plateau age of  $2.62 \pm 0.03$  Ma (Fig. B3) and consistent with the isochron age,  $2.607 \pm 0.017$  Ma. The trapped  $^{40}\text{Ar}/^{36}\text{Ar}$  ratio ( $295.3 \pm 1.1$ ) is not distinct from that of atmospheric Ar.

BC-18 and RC-01 yield ages of  $3.41 \pm 0.04$  ( $3.31 \pm 0.03$  isochron age; Fig. B4) and  $1.37 \pm 0.04$  Ma ( $1.30 \pm 0.07$  Ma isochron age; Fig. B5), respectively. Both spectra are very flat on more than 90 % of the total  $^{39}\text{Ar}$  released. The trapped  $^{40}\text{Ar}/^{36}\text{Ar}$  ratios are not distinct from that of atmospheric ( $297.3 \pm 0.4$  and  $296.7 \pm 1.1$ , respectively).

**Plagioclase:** Four samples display discordant spectra (HS-19, RC-01, BC-18, and Tdo; none of these are shown). The complexity of these spectra could be attributed to the presence of plagioclase xenocrysts and also to non-atmospheric initial (excess) argon, which contributes to the apparent high ages at low and high temperatures. Sample RC-14 shows a plateau age according to our criteria defined above of  $2.63 \pm 0.04$  Ma (97%). This age is not distinct from that one obtained from the coexisting groundmass (compare Figures B6 and B3).

#### References cited in this appendix:

- Dalrymple et al., 1975 : Geological Society of America Bulletin, 86, 399-411.  
 Huneke and Smith, 1976 : Geochimica and Cosmochimica Acta Supplement 7, 1987-2008  
 Forland et al., 1993 : : Chemical Geology 107, 173-190.  
 Sharp et al., 1996 : Journal of Geophysic Research vol 101, 11,607-11,616.  
 Steiger and Jäger 1977 : Earth and Planetary Science Letter 36, 359-362.  
 Renne et al., 1998 : Chemical Geology 145, 117-152.

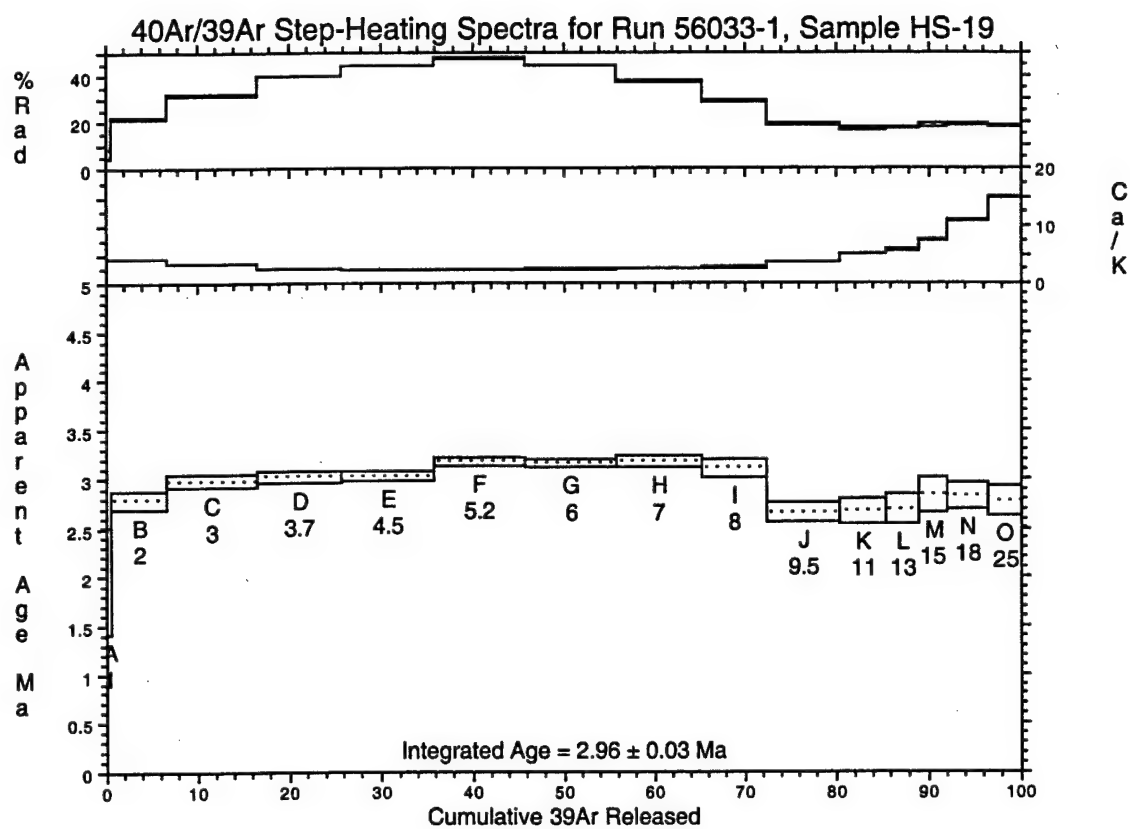


Figure B1 - groundmass

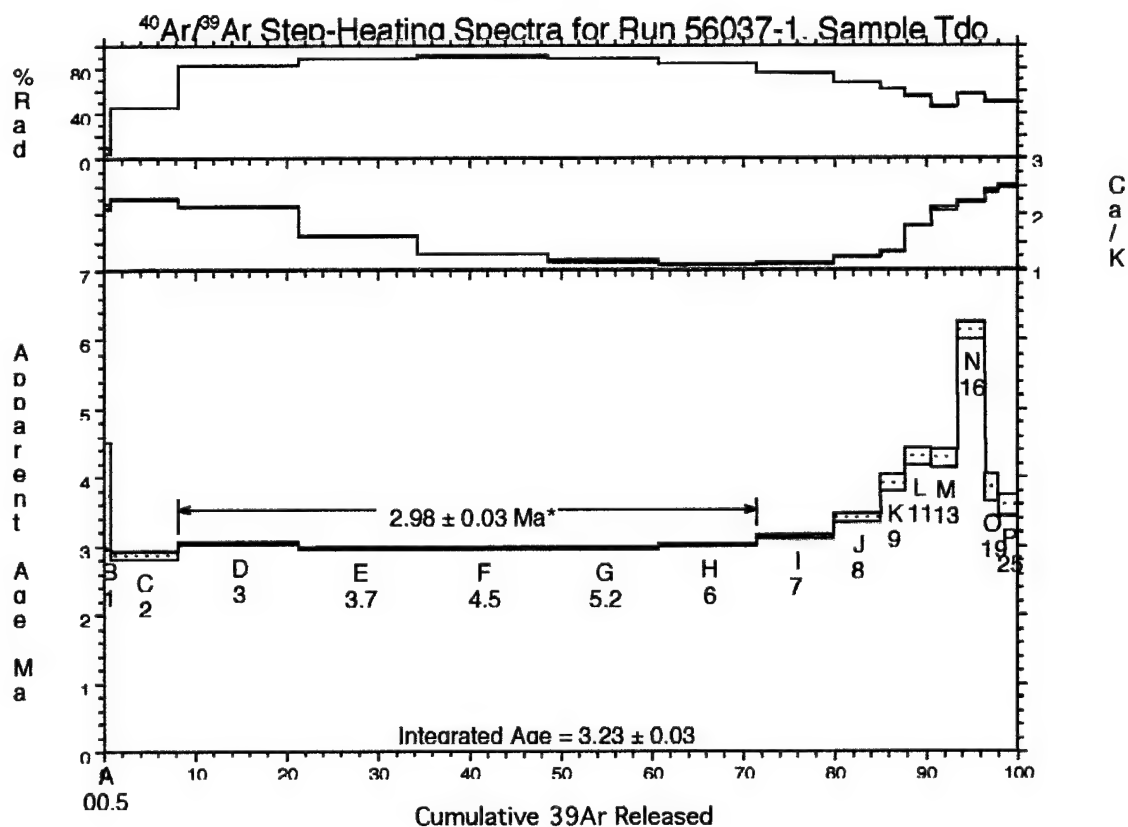
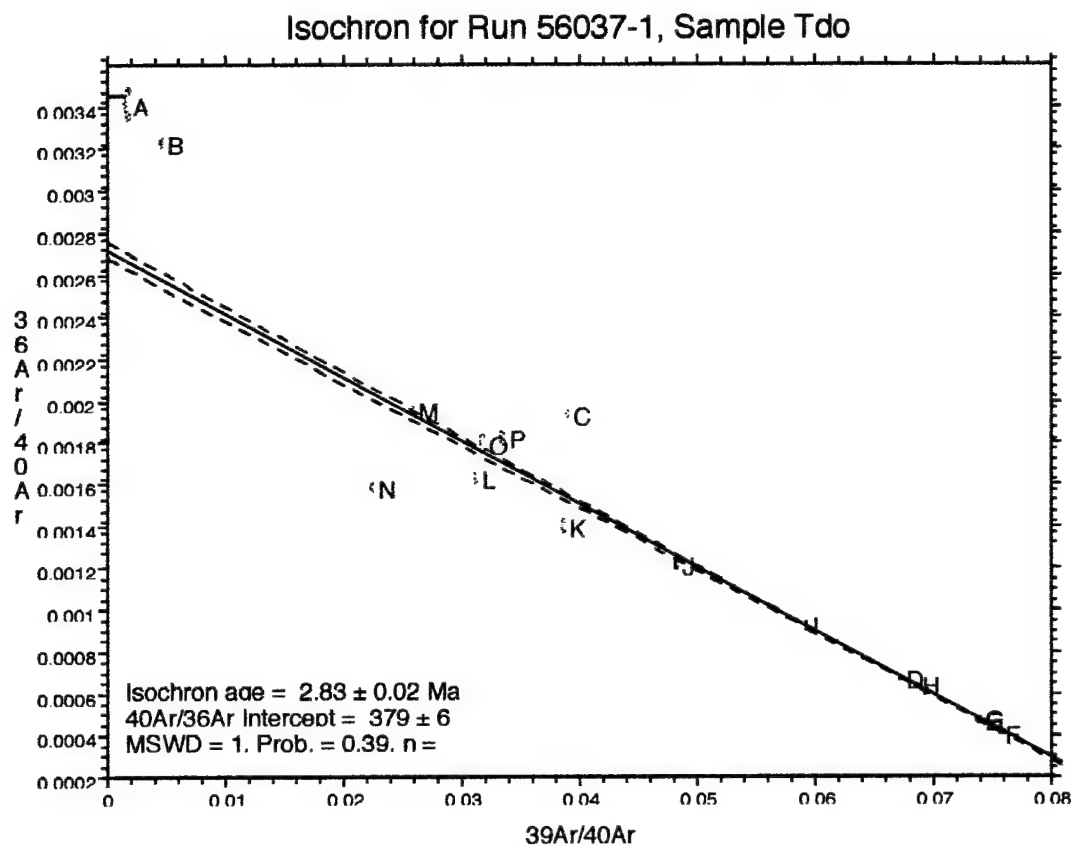


Figure B2 - groundmass



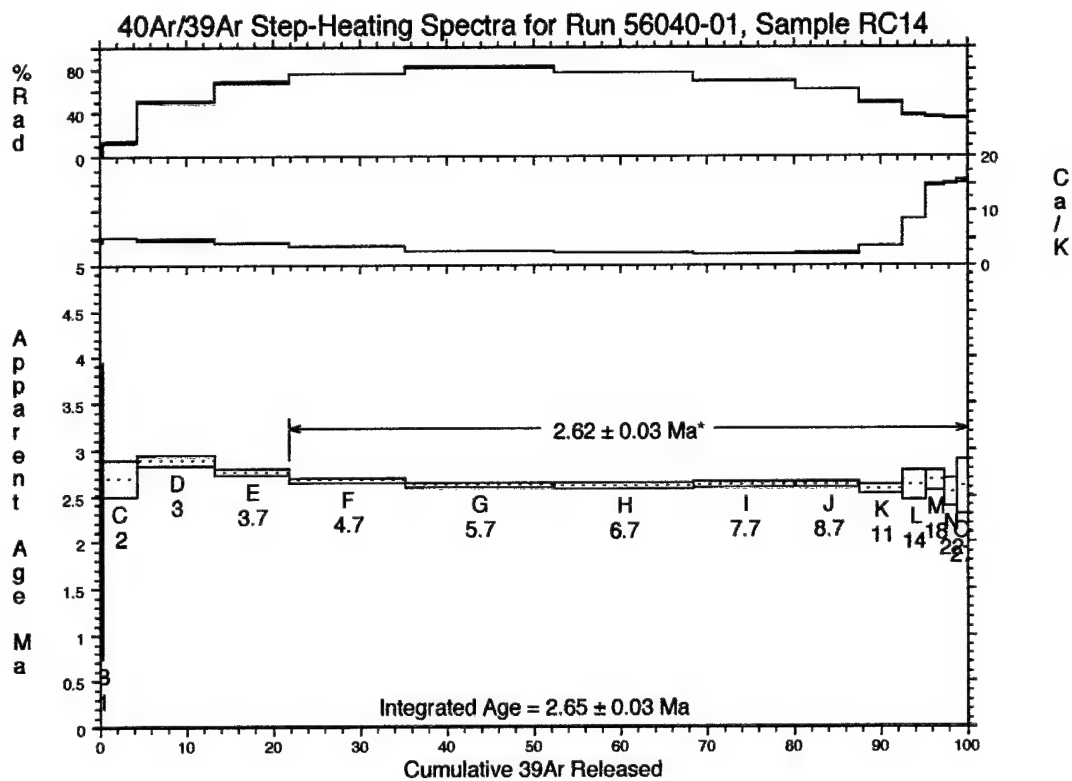
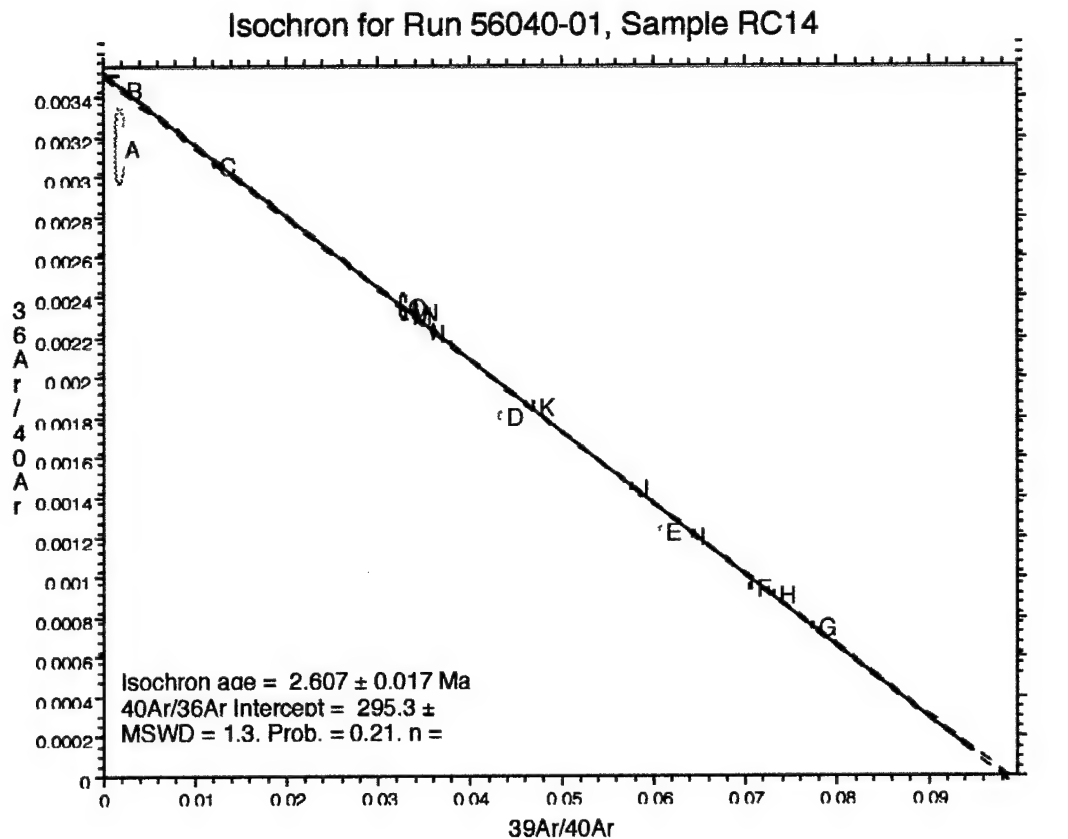


Figure B3 - groundmass

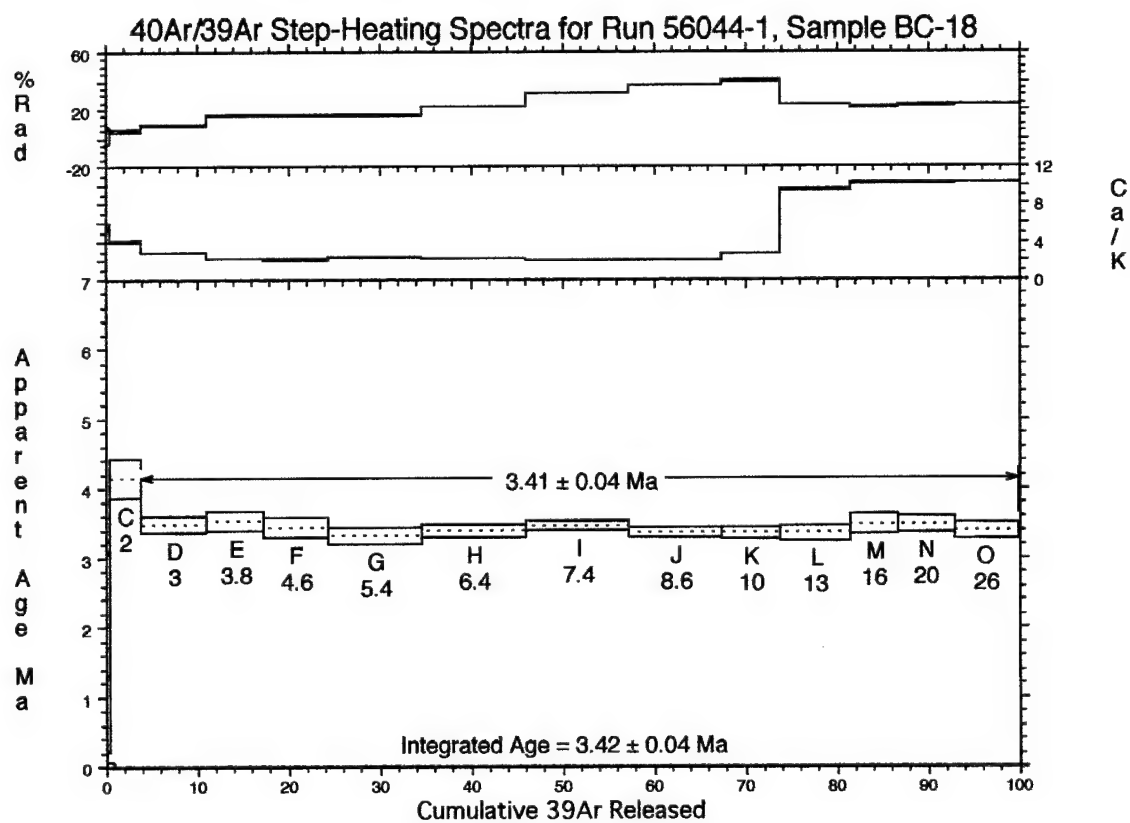
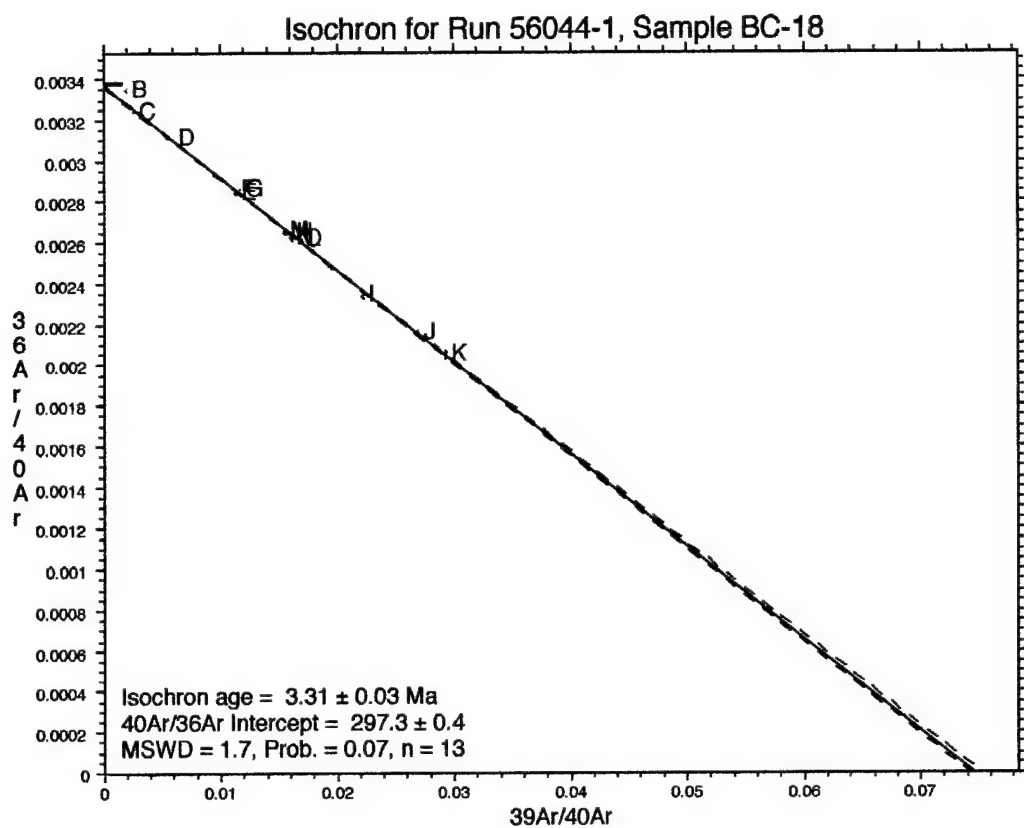


Figure B4 - groundmass

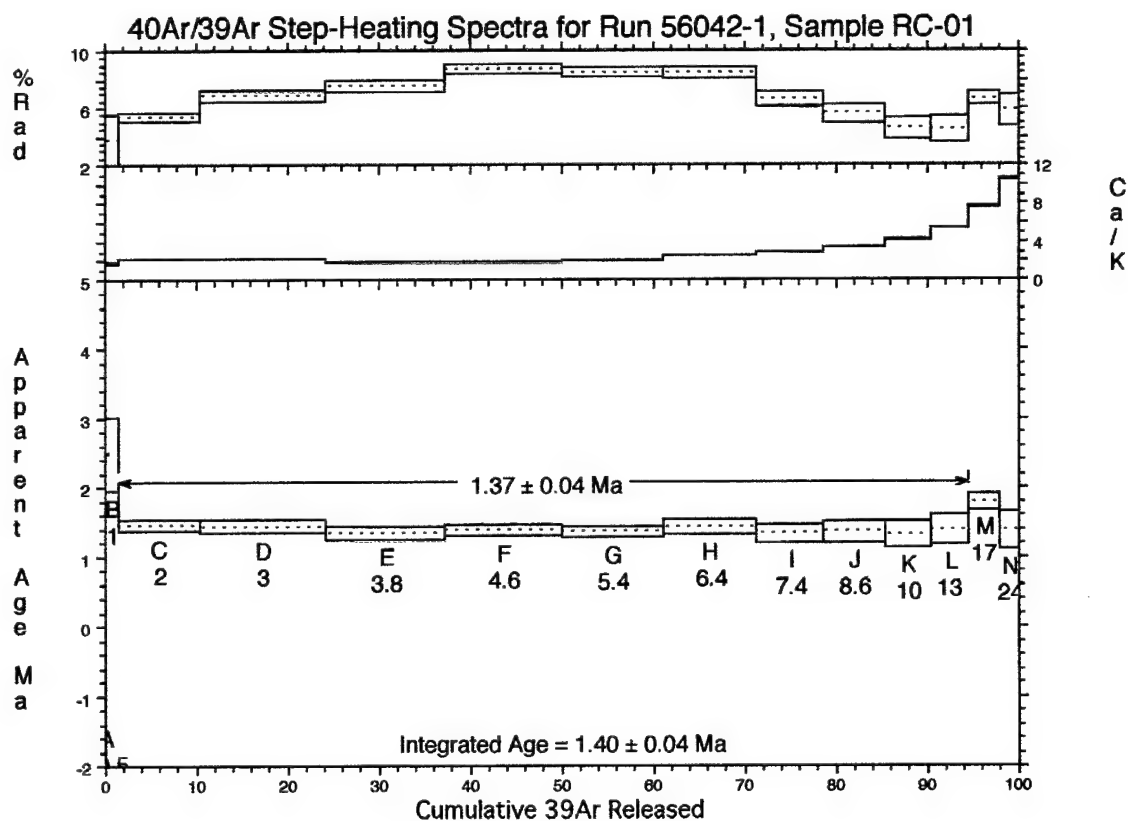
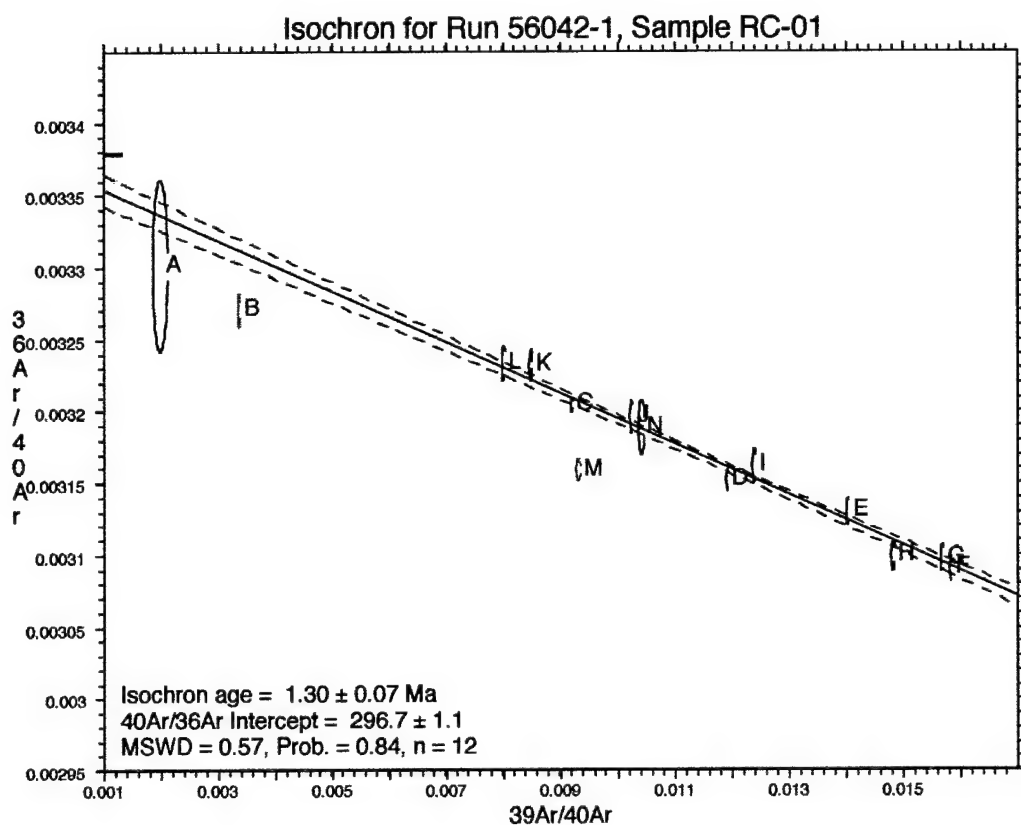


Figure B5 - groundmass

Purchase Request Number: N68936-01-C-0094

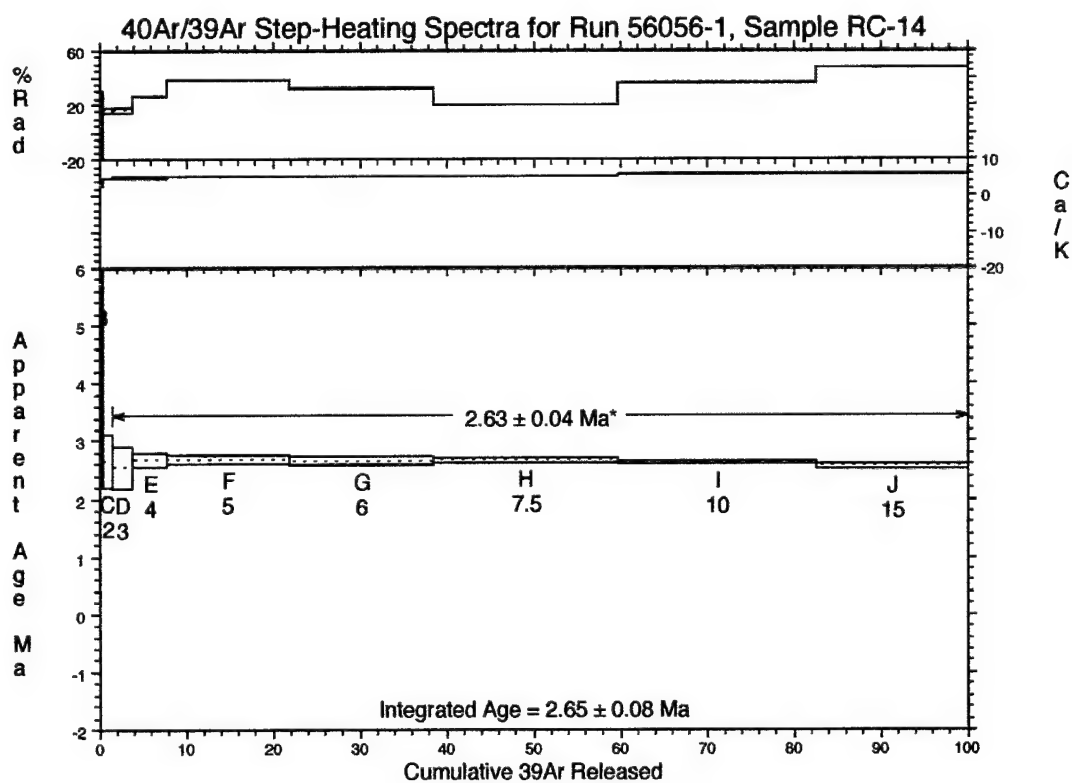
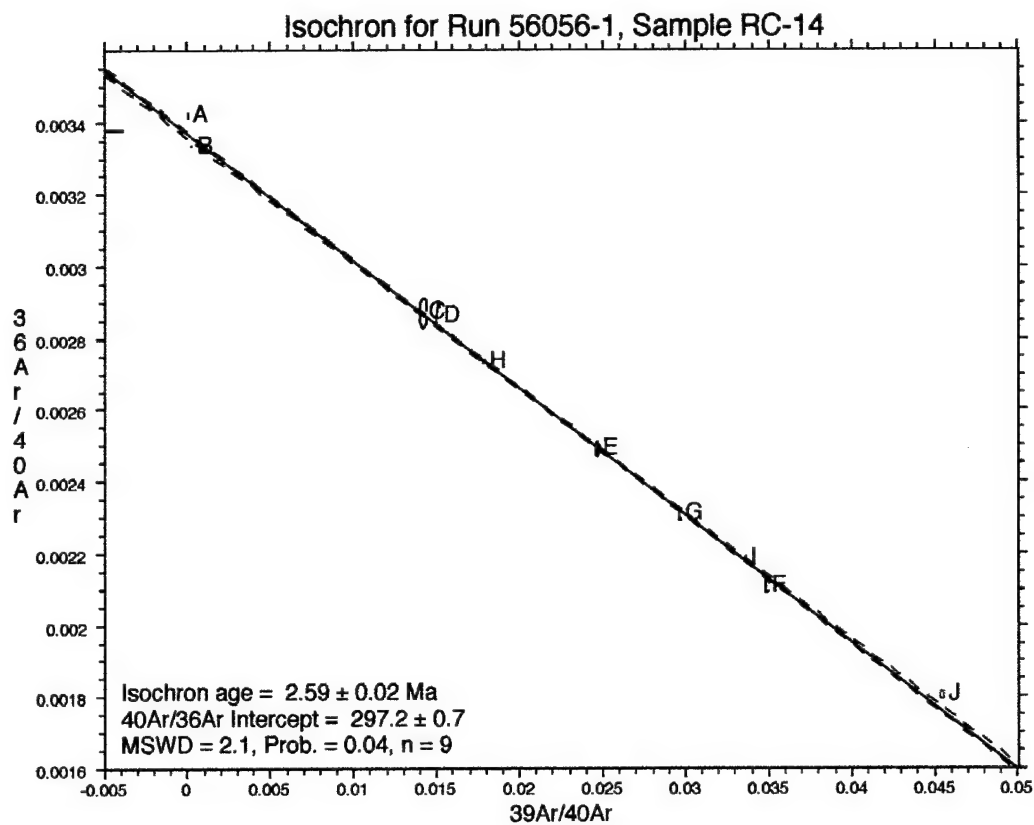
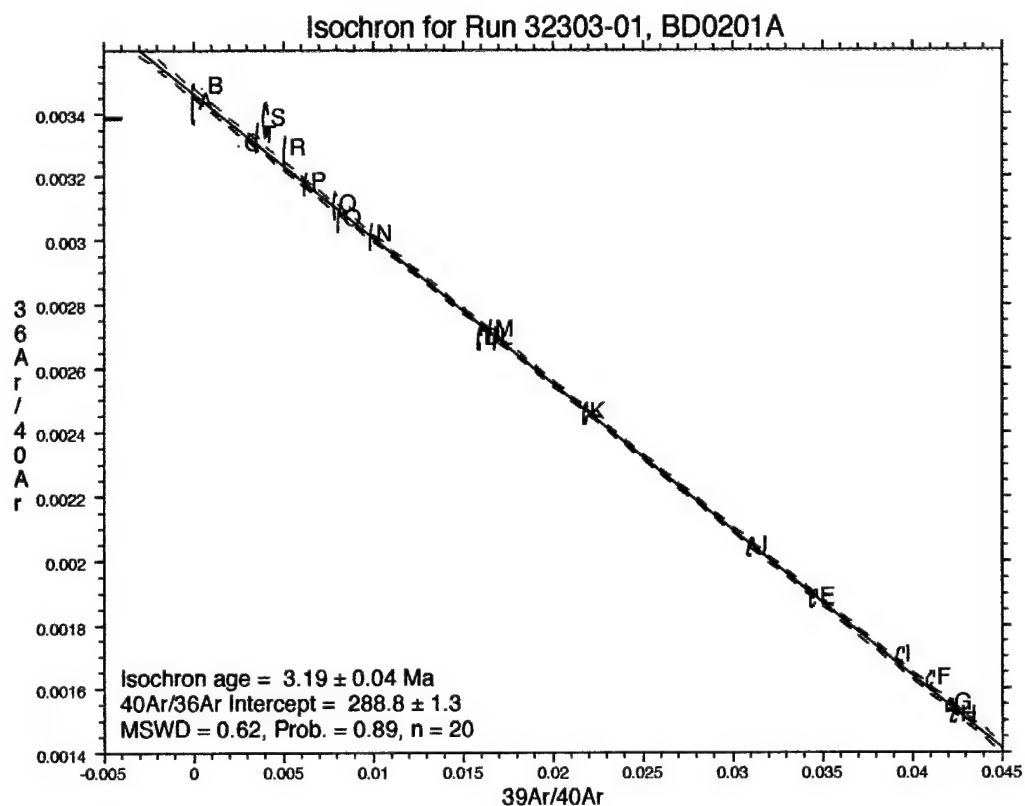
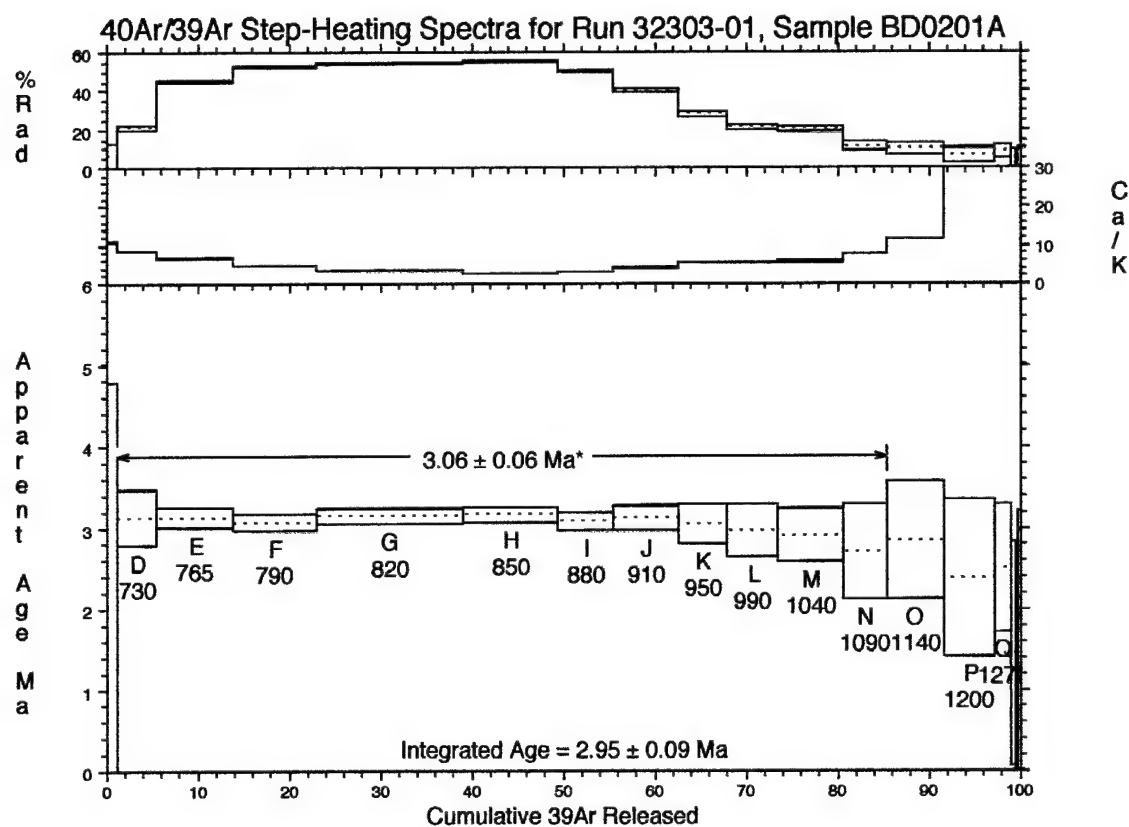
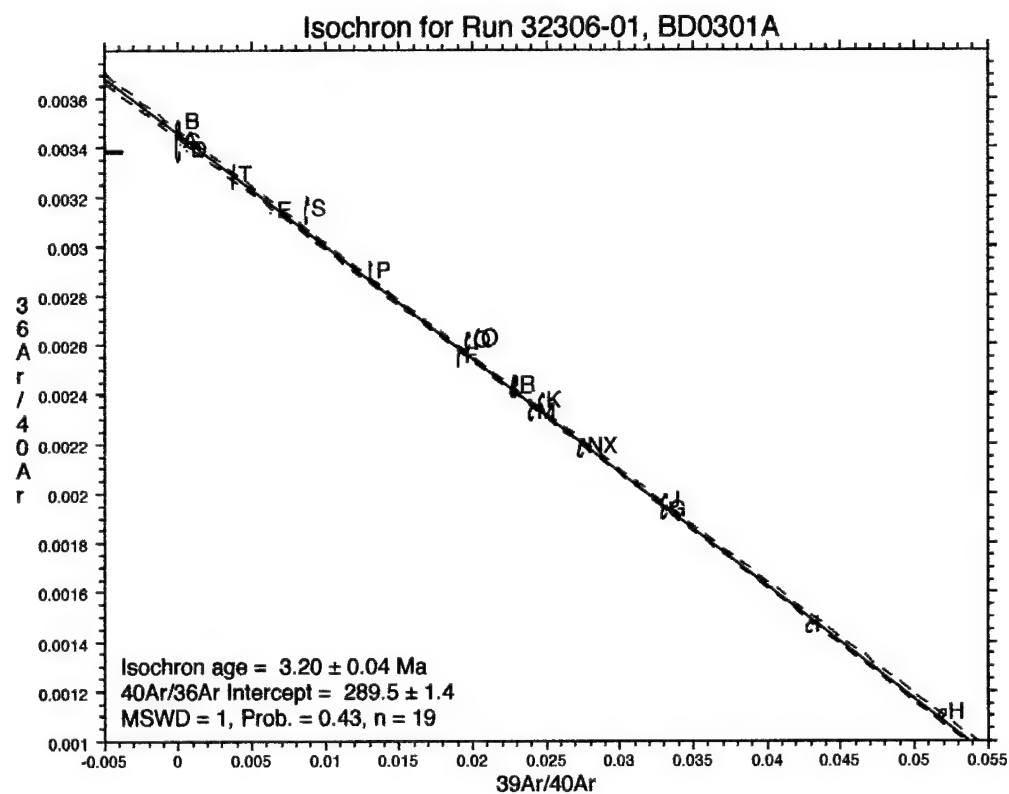
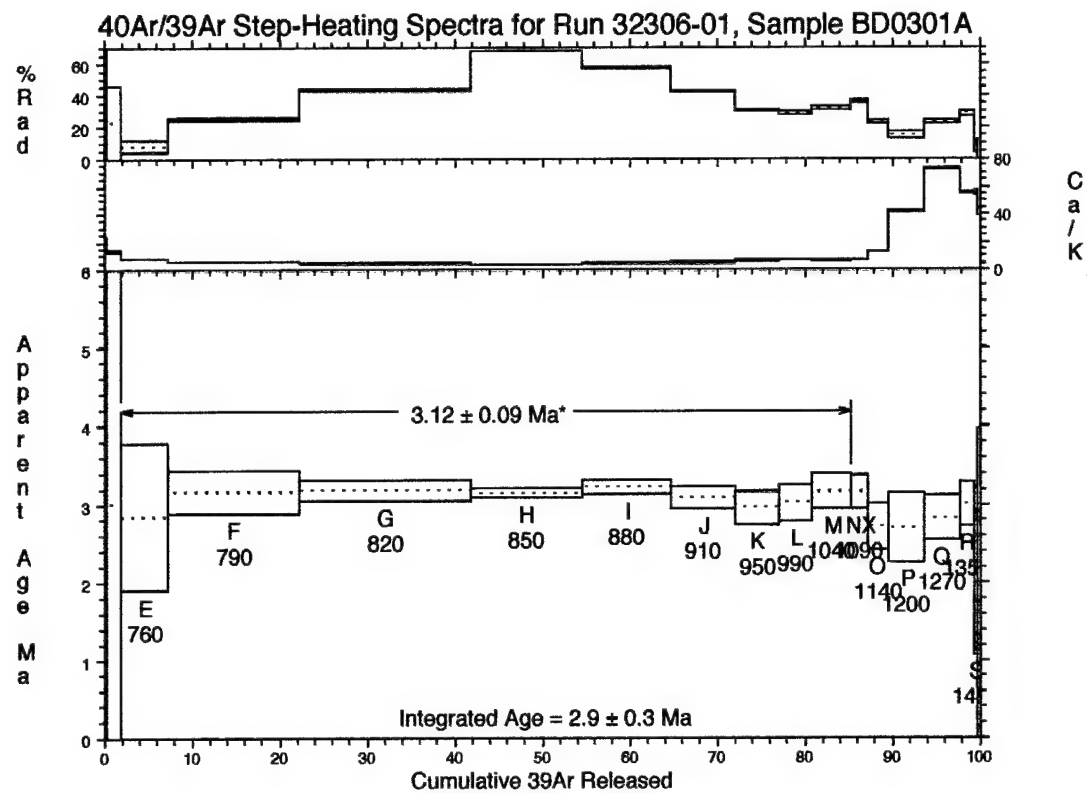
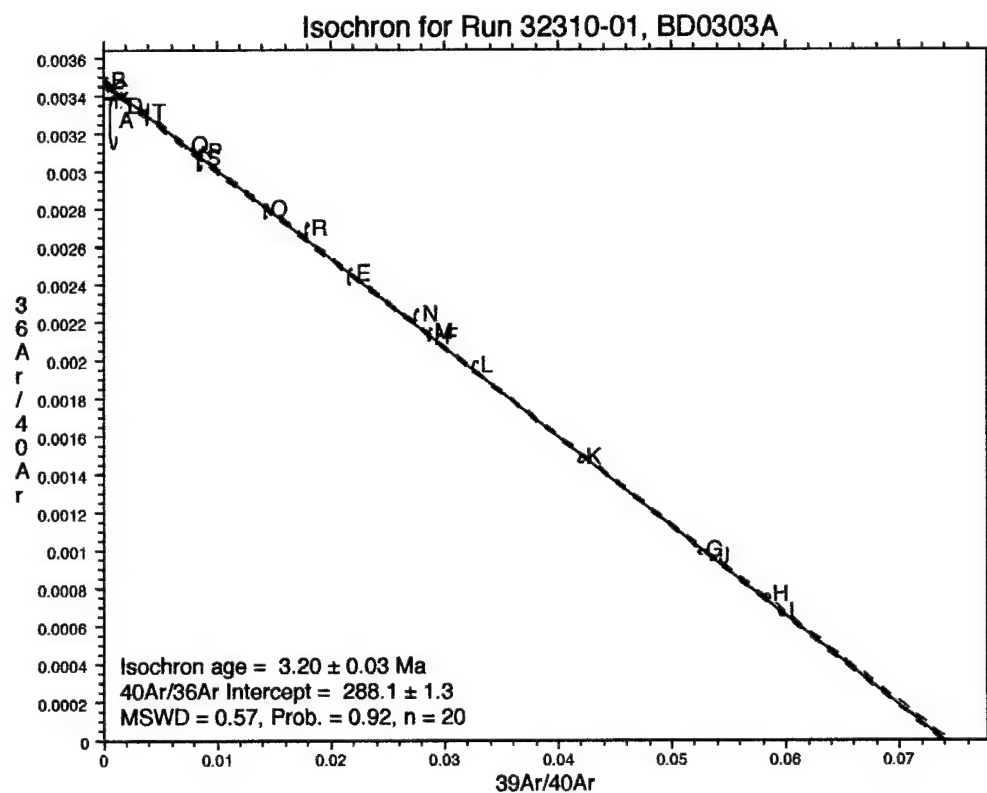
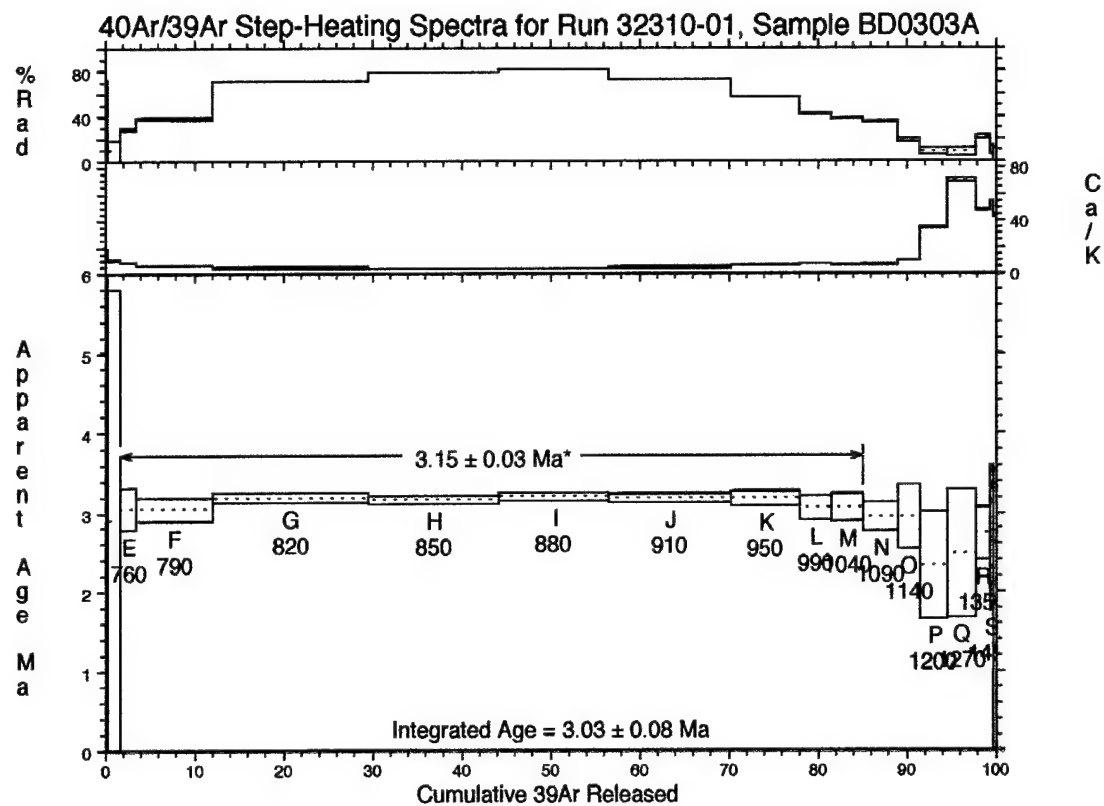


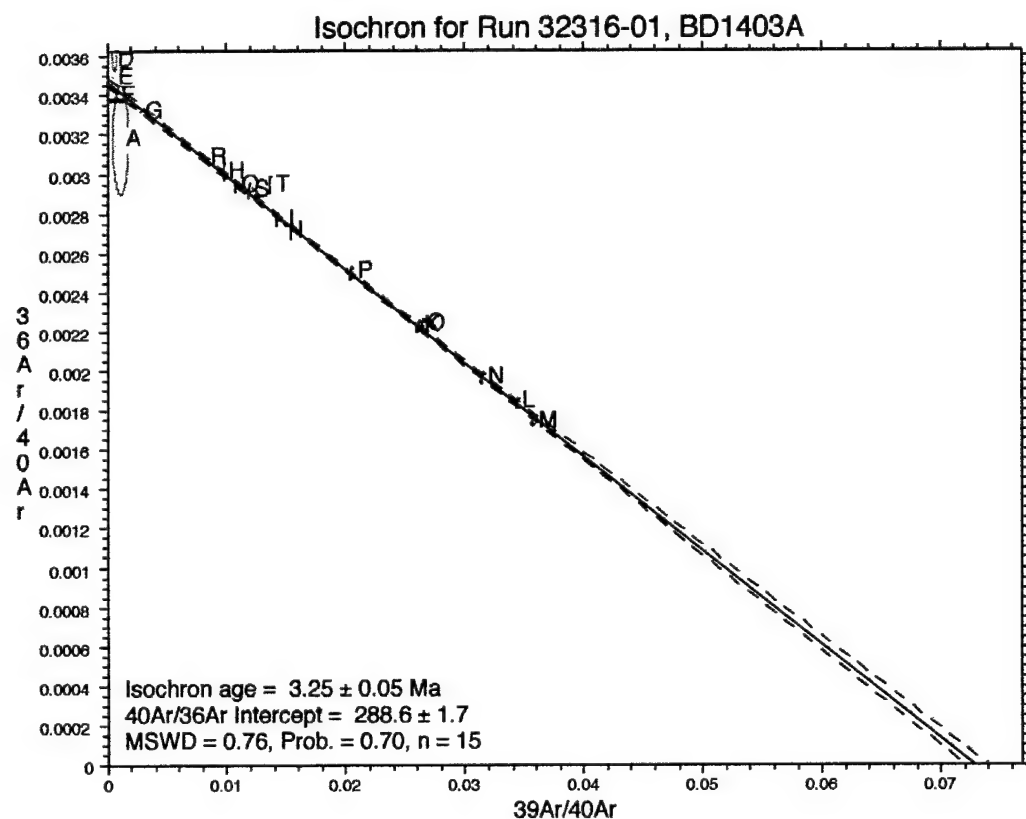
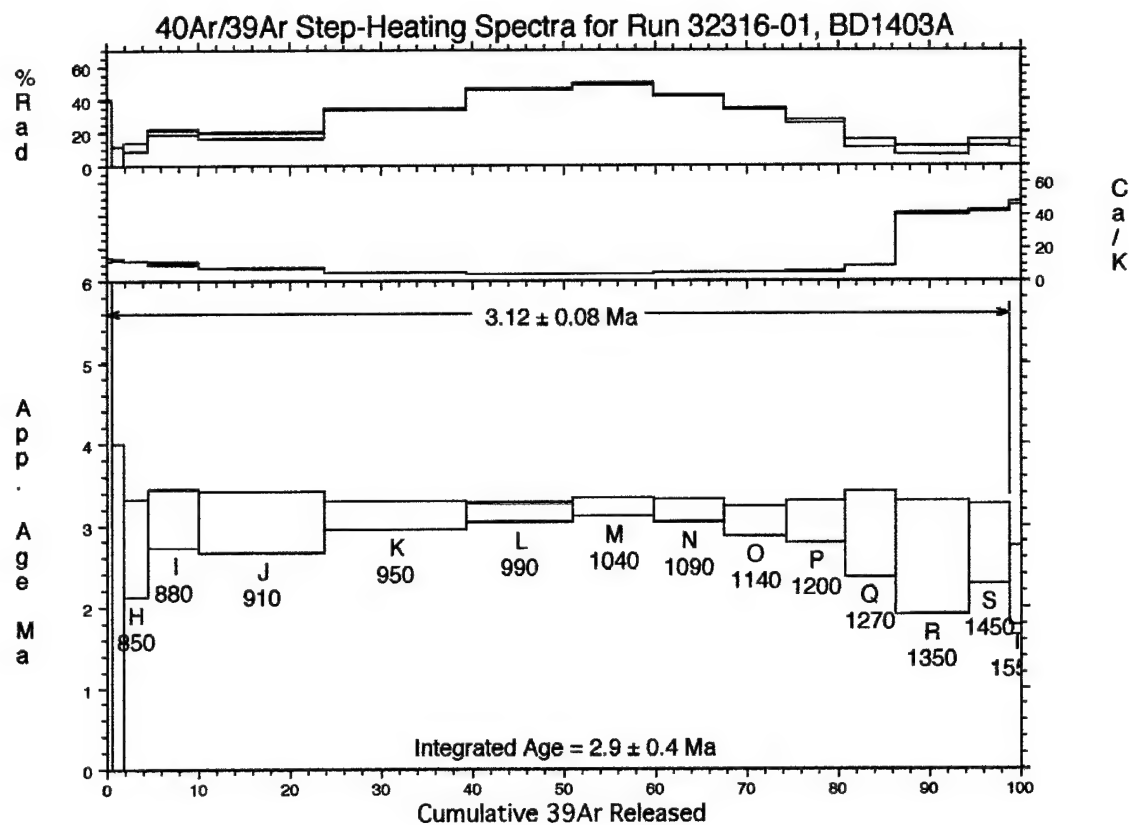
Figure B6 – plagioclase

Purchase Request Number: N68936-01-C-0094

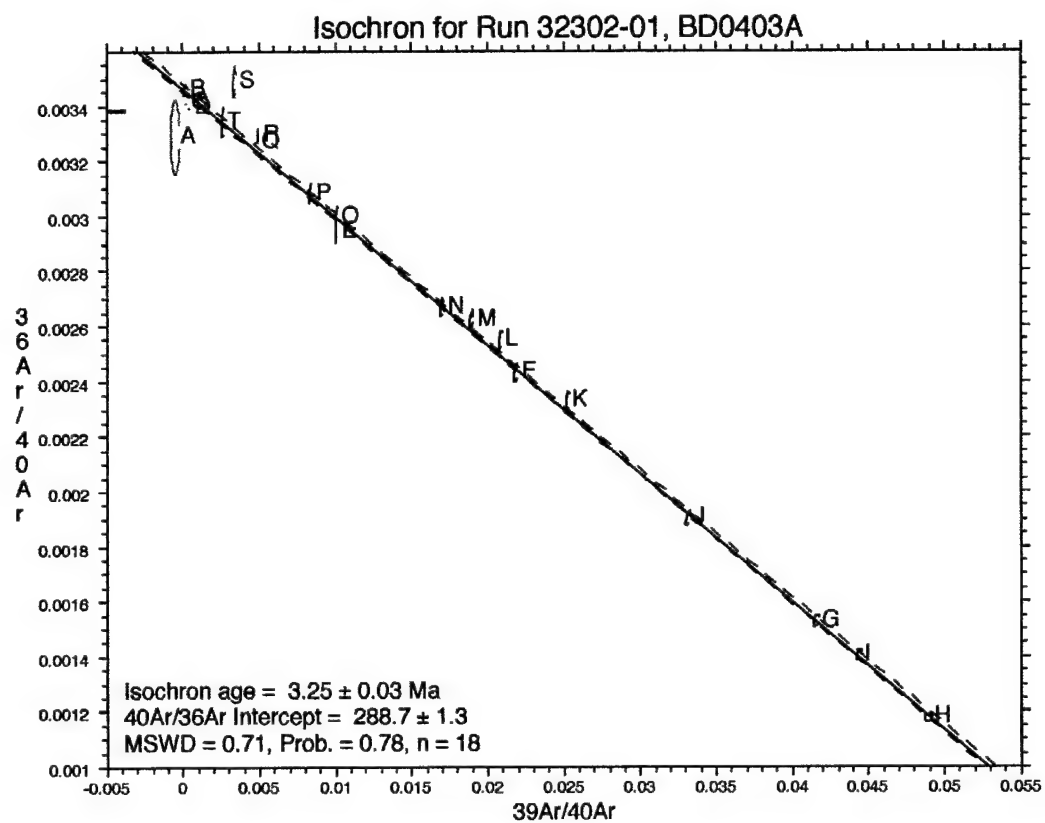
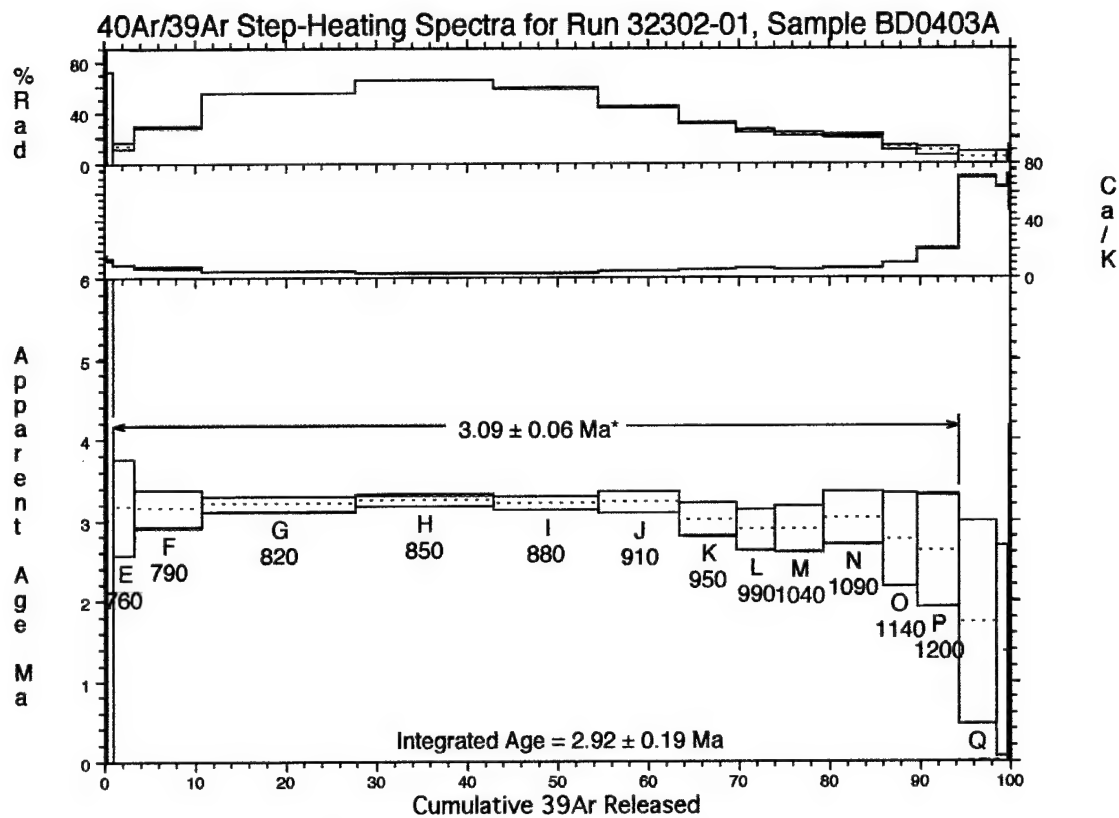


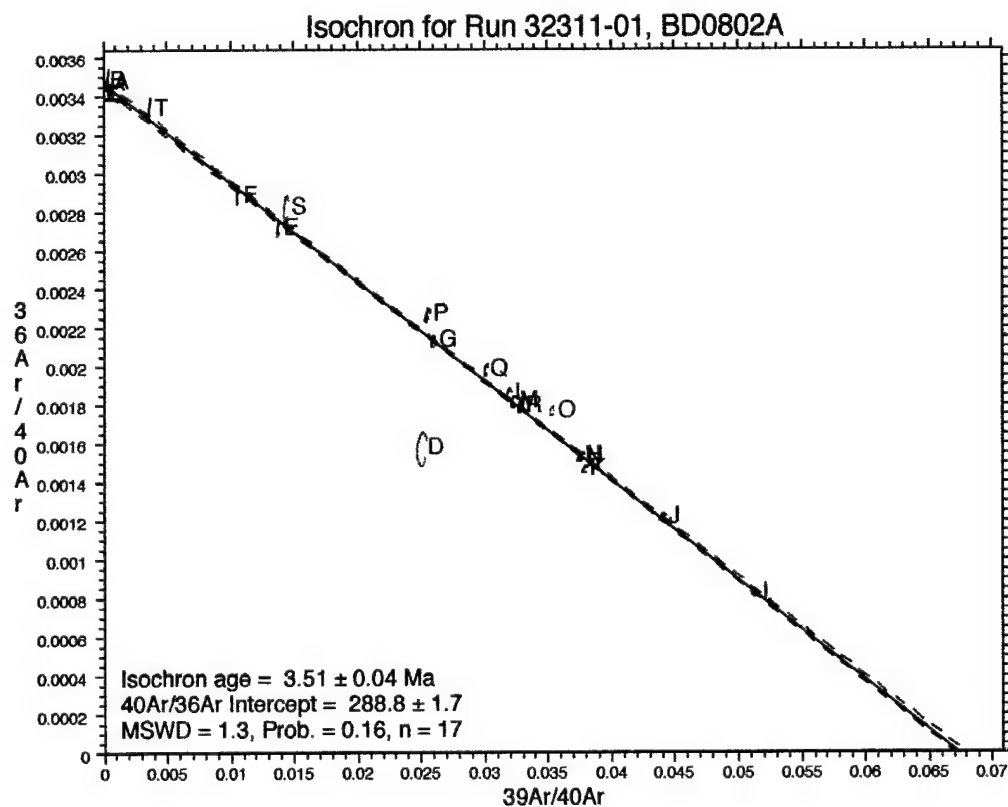
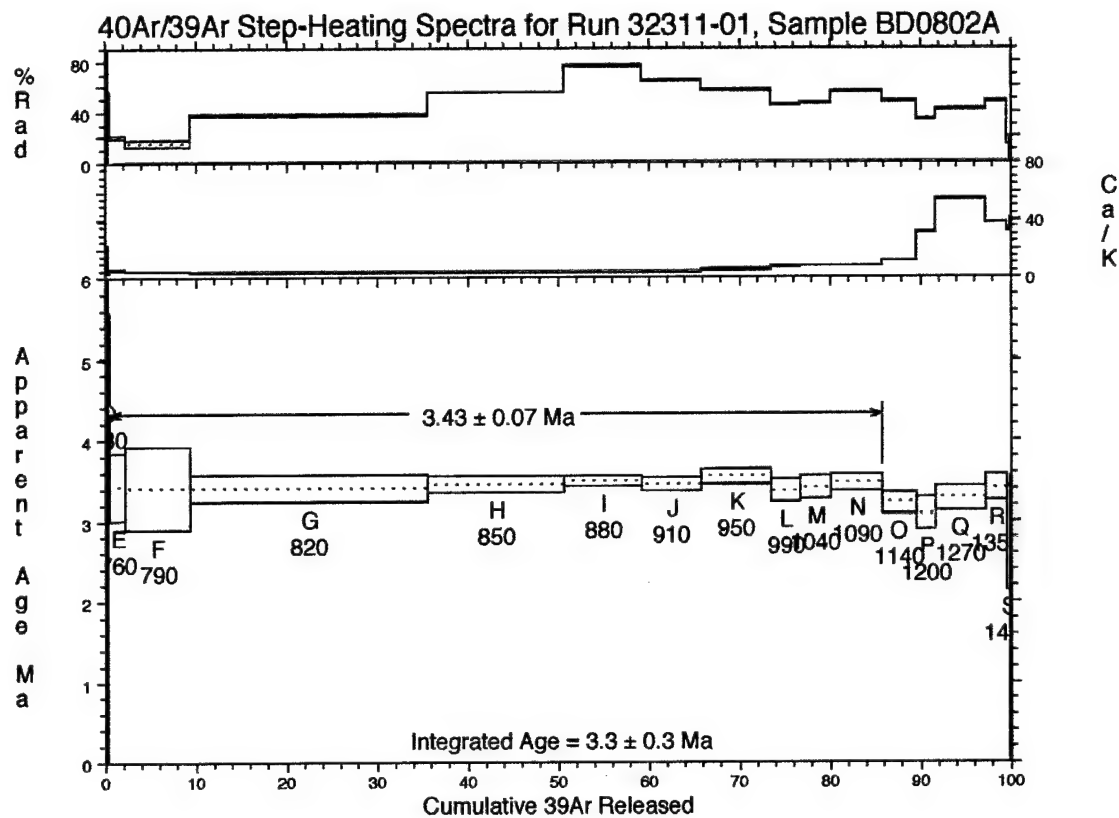


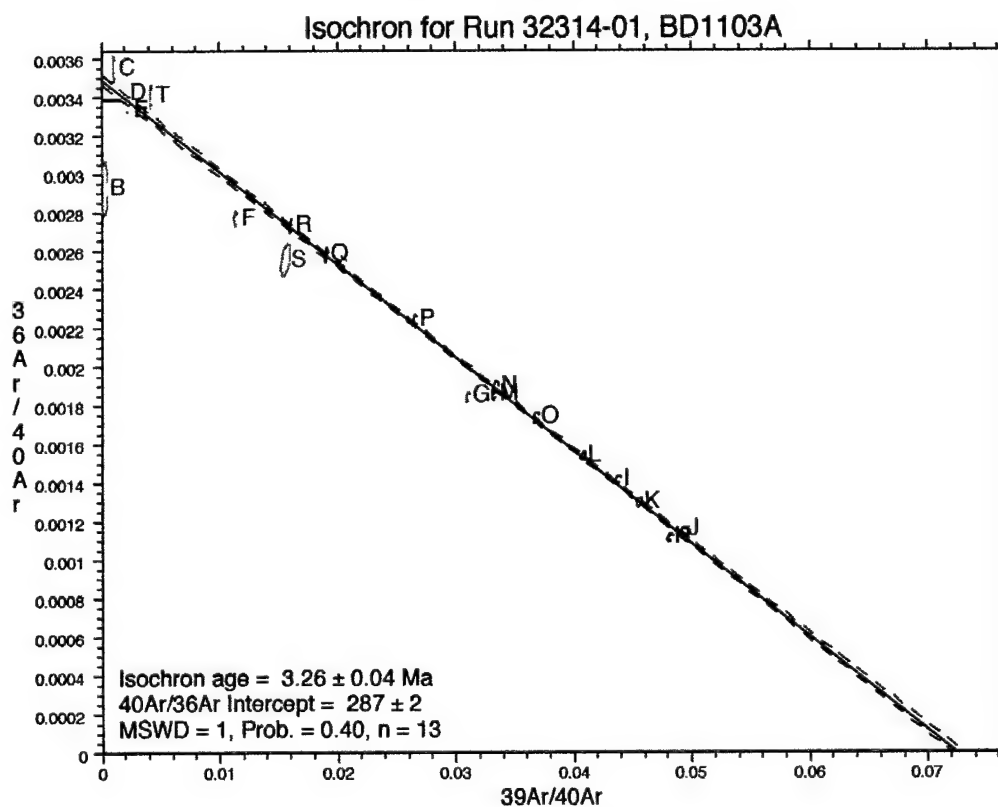
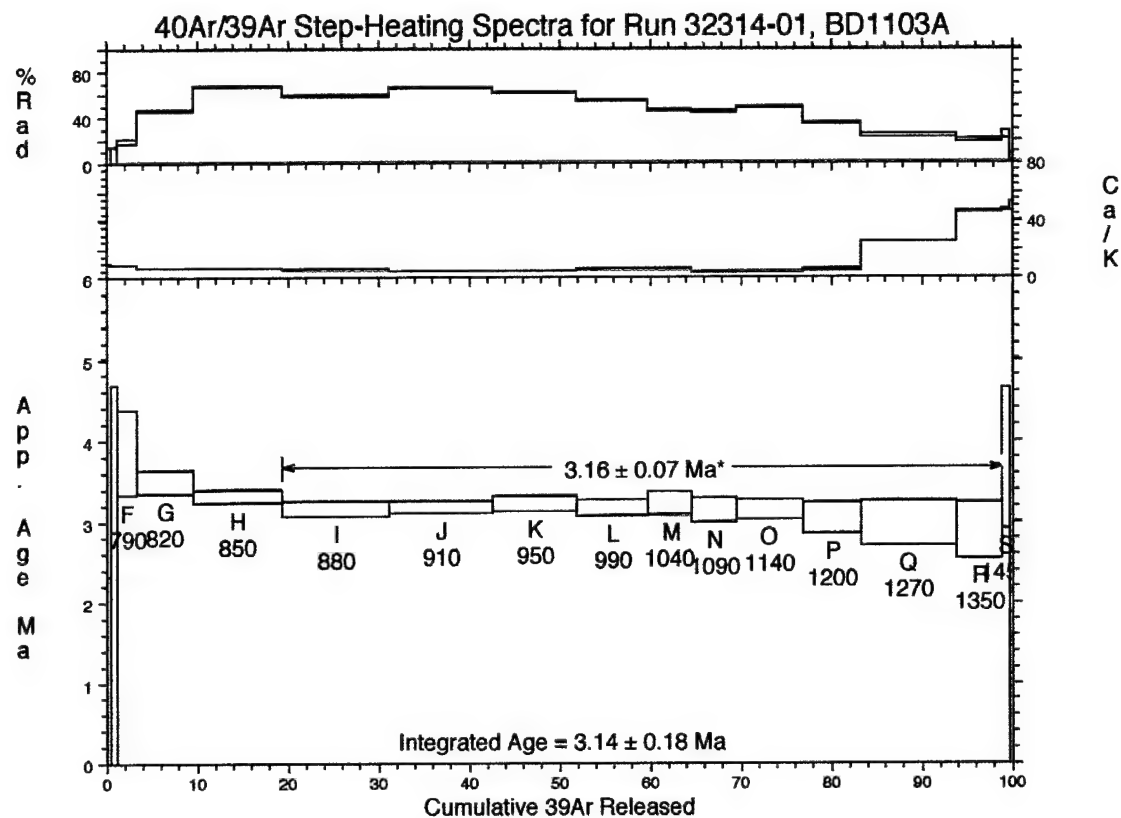












## **Appendix C**

### **Lateral Extent of Eruptive Units**

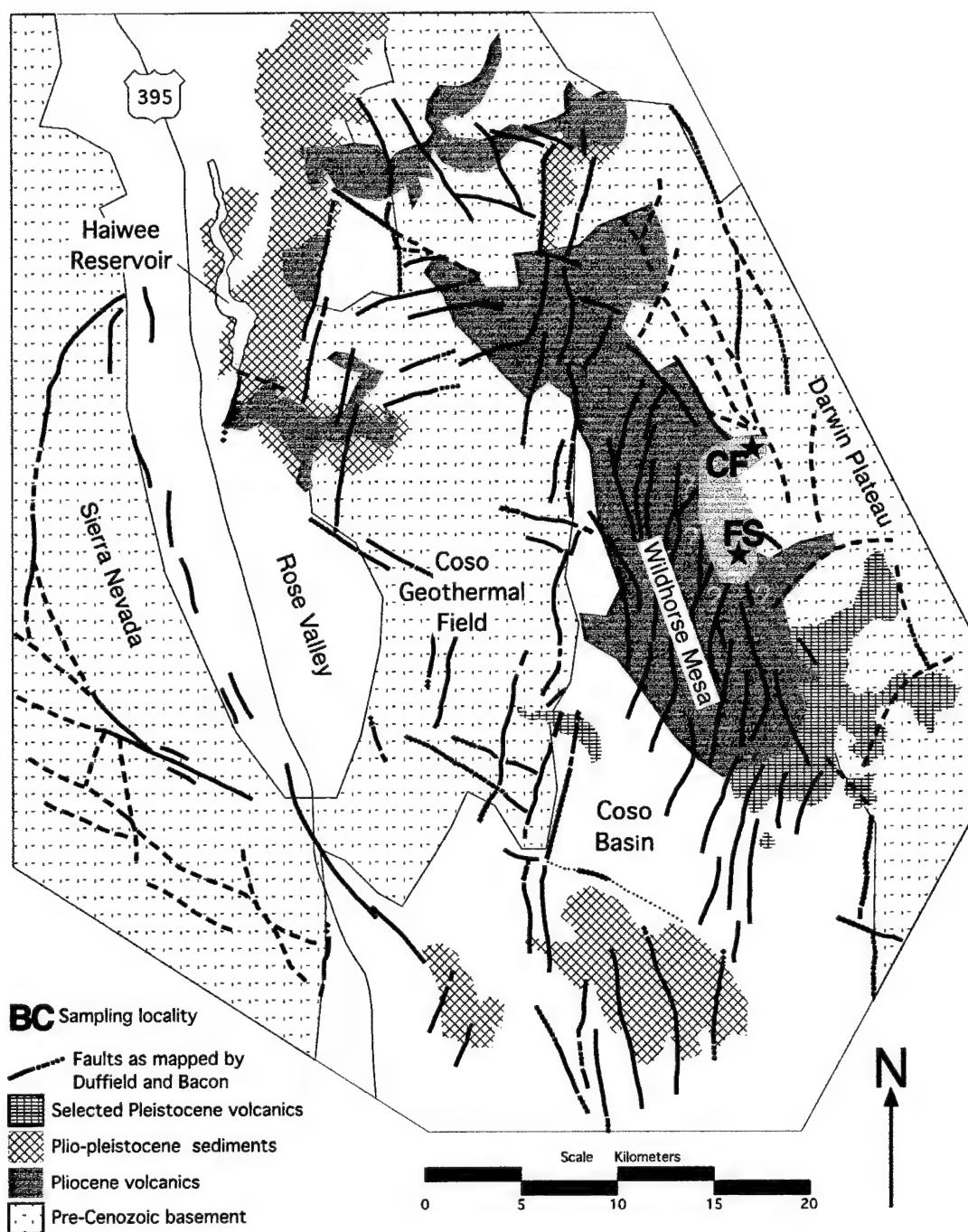


**Figure C1 - Lateral Extent of Cole Flat Basalt** - in green. This unit, comprised of at least four flows near its source, exhibits normal paleomagnetic polarity (declination  $\sim 335^\circ$ , inclination  $\sim 52^\circ$ ). Question marks indicate uncertainty on the location of the edge of the unit. This member erupted just northeast of sampling locality CF at  $3.50 \pm 0.03$  Ma. See main report for geochemical composition and details of geochronology.

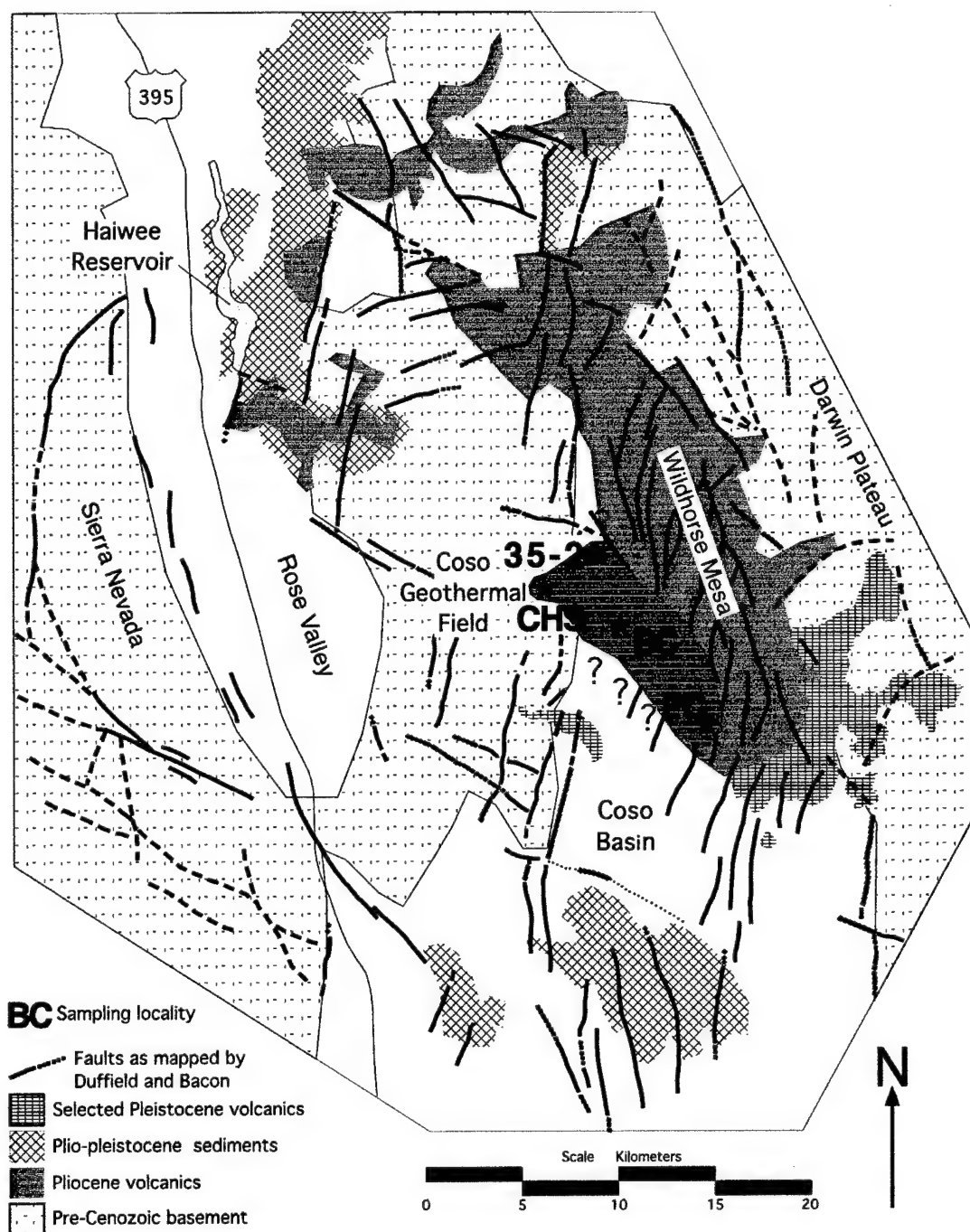


**Figure C2 - Lateral Extent of Black Canyon Flows** - in red. This unit, comprised of at least ten flows near its source, exhibits normal paleomagnetic polarity (declination  $\sim 35^\circ$ , inclination  $\sim 27^\circ$ ). Question marks indicate uncertainty on the location of the edge of the unit. This member erupted just southwest of sampling locality BC at  $3.41 \pm 0.04$  Ma. See main report for geochemical composition and details of geochronology.

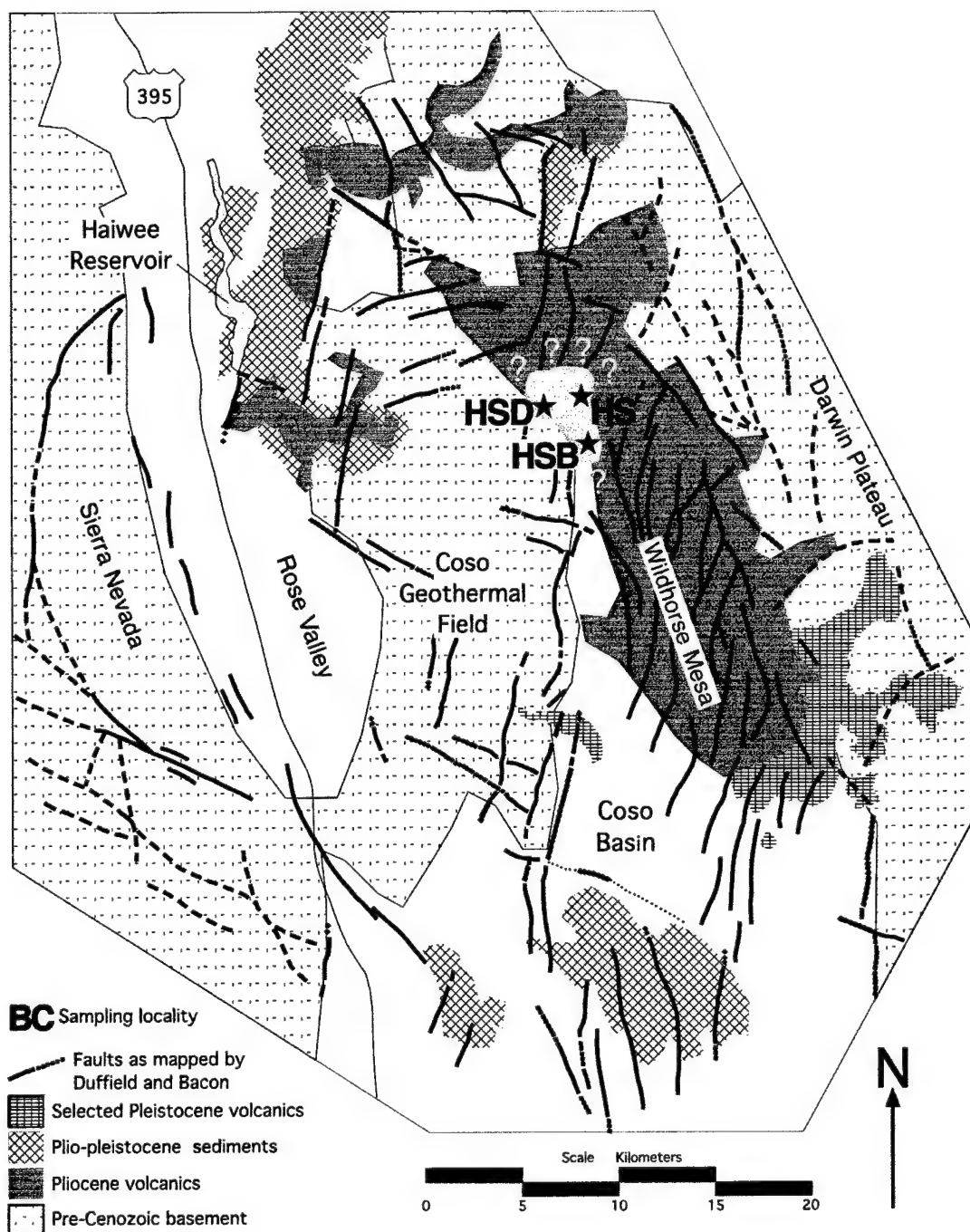


**Figure C3 - Lateral Extent of Haiwee Spring Basalt - in aqua.** This unit, comprised of nineteen flows at locality HS, exhibits normal paleomagnetic polarity (declination  $\sim 320\text{--}330^\circ$ , inclination  $\sim 50\text{--}60^\circ$ ). Question marks indicate uncertainty on the location of the edge of the unit. This member erupted from an unknown locality north of the sampled localities indicated around  $3.32 \pm 0.1$  Ma (Duffield and Bacon, 1981). See main report for geochemical composition.

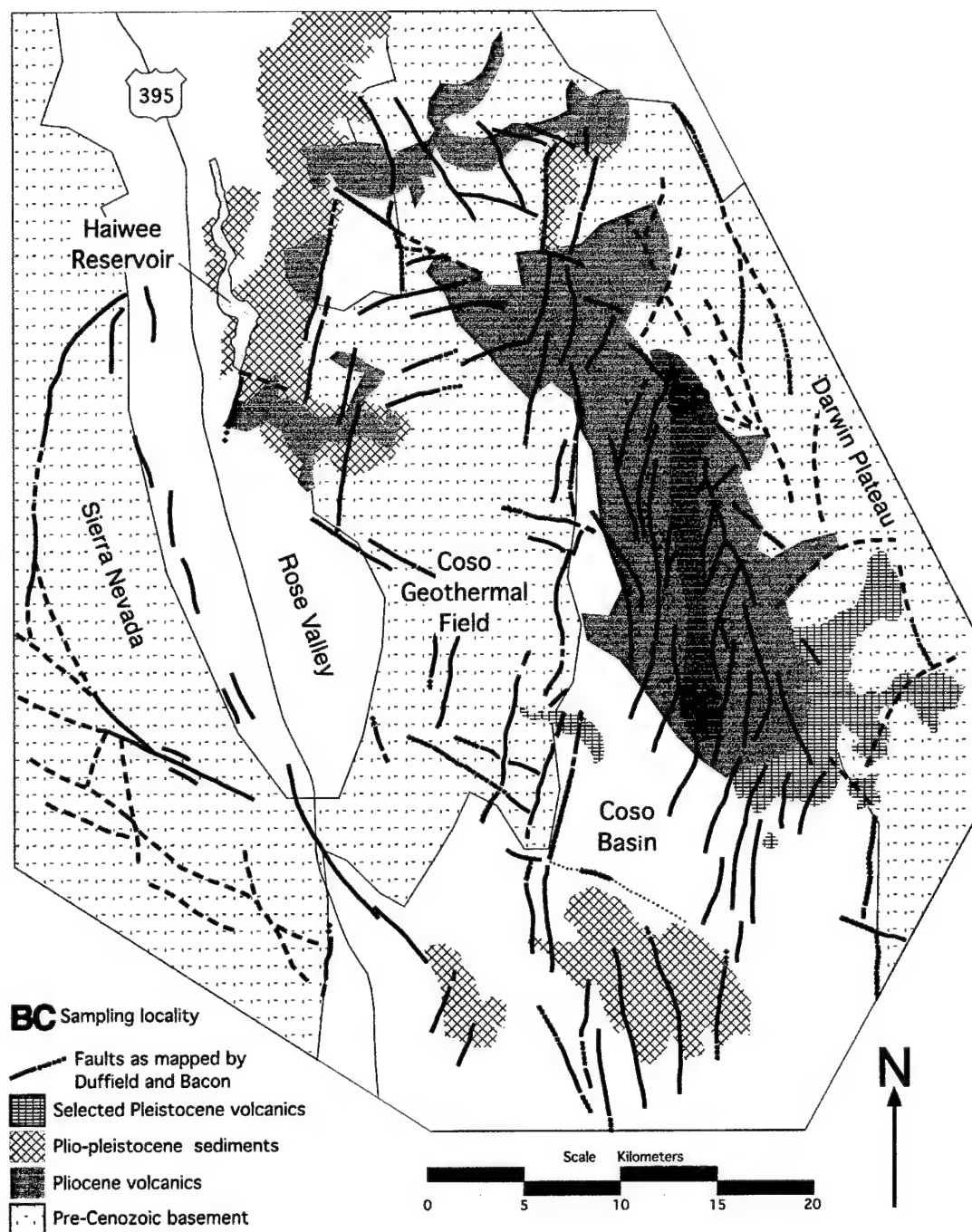


**Figure C4 - Lateral Extent of Silver Peak Basalt** - in pink. This unit exhibits reversed paleomagnetic polarity (declination  $\sim 140-150^\circ$ , inclination  $\sim -20^\circ$ ). Question marks indicate uncertainty on the location of the edge of the unit. This unit erupted just northwest of sampling locality SP between  $3.22 \pm 0.02$  and  $3.41 \pm 0.04$  Ma based on stratigraphic considerations. See main report for geochemical composition.



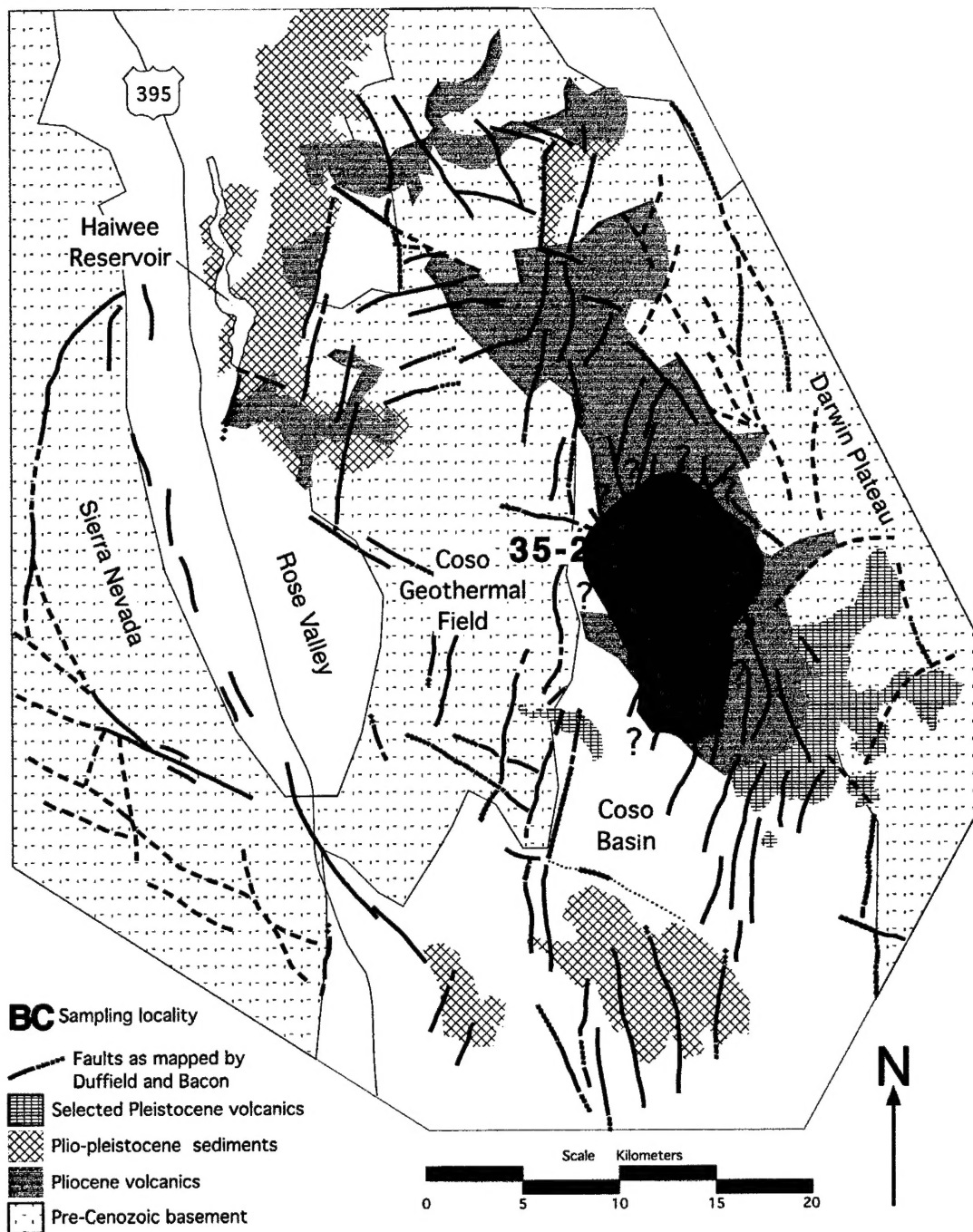


**Figure C5 - Lateral Extent of Petroglyph Canyon Basalt - in blue.** This unit, comprised of at least six flows at locality LDC, exhibits reversed paleomagnetic polarity (clockwise rotated to declination  $\sim 137^\circ$ , inclination  $\sim -18^\circ$ ). Question marks indicate uncertainty on the location of the edge of the unit. This member perhaps erupted just east of sampling locality FS at  $3.22 \pm 0.02$  Ma. See main report for geochemical composition and details of geochronology.

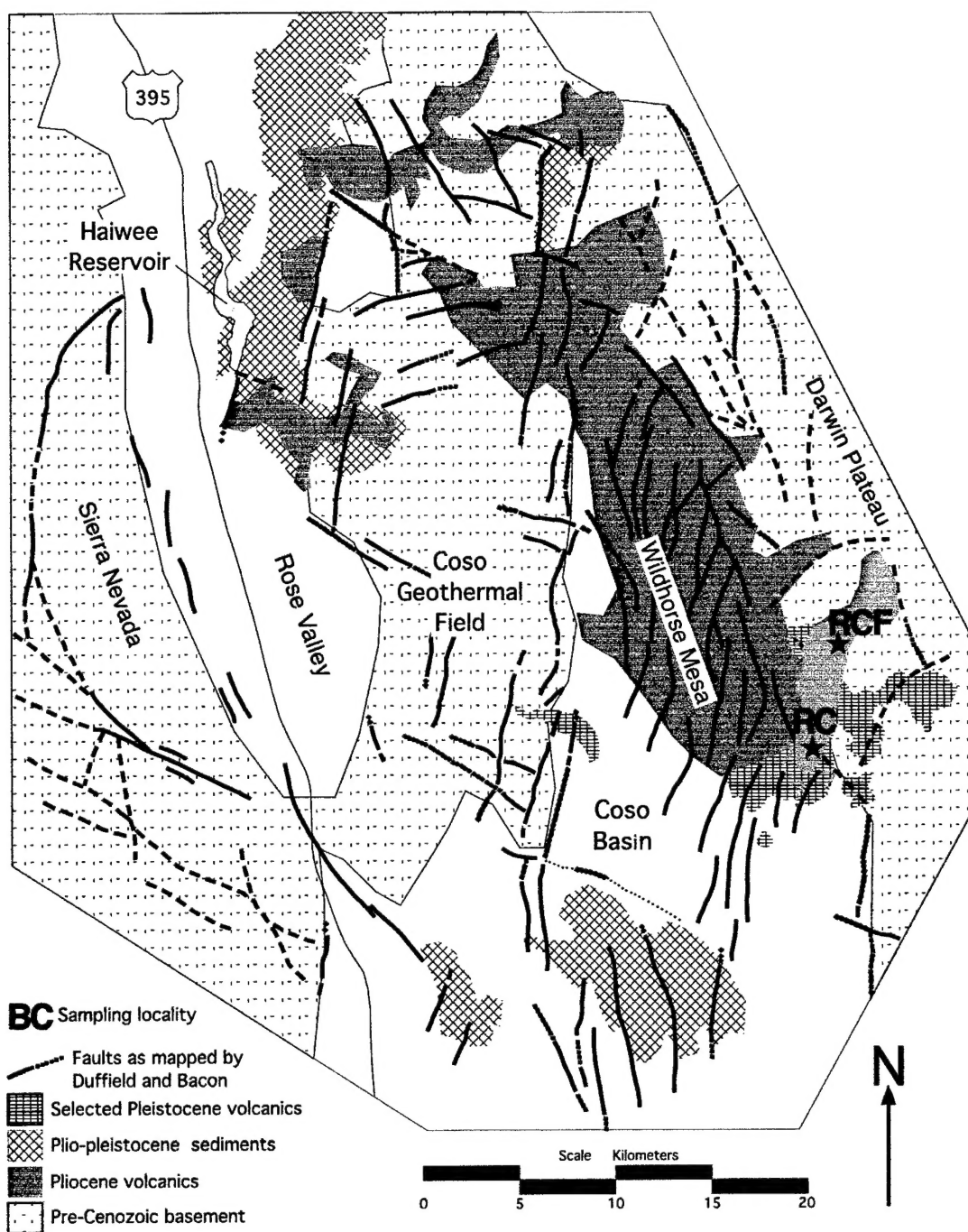


**Figure C6 - Lateral Extent of QTbr<sub>1</sub> Andesite** - in light blue. Correlation of this unit is tentative because of equivocal geochemical correlation and the lack of paleomagnetic results at locality RCF. Locality RC is comprised of at least ten flows thought to be QTbr<sub>1</sub> and exhibiting an unusual reversed paleomagnetic direction (declination ~ 250°, inclination ~ -75°). Question marks indicate uncertainty on the location of the edge of the unit. This member erupted just northeast of sampling locality RCF at 2.62 ± 0.03 Ma. See main report for geochemical composition and details of geochronology.

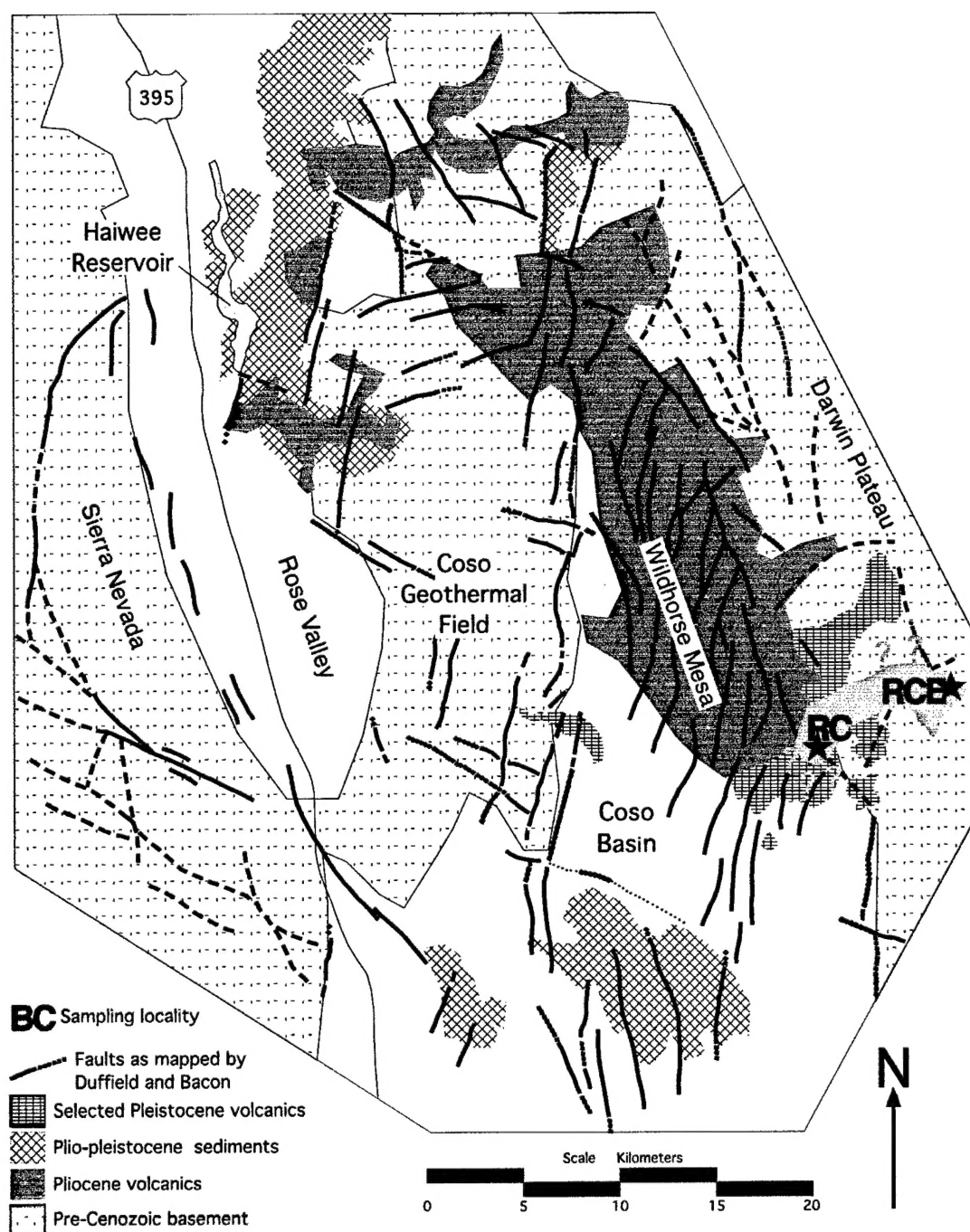


**Figure C7 - Lateral Extent of QTbr<sub>2</sub> Andesite** - in orange. This unit is composed of a maximum of only two or three flows (at locality RC). QTbr<sub>2</sub> exhibits reversed paleomagnetic polarity but variable directions (declination ~ 170-195°, inclination ~ -40 to -50°). Question marks indicate uncertainty on the location of the edge of the unit. This member erupted near sampling locality RCE at 1.37 ± 0.04 Ma. See main report for geochemical composition and details of geochronology.

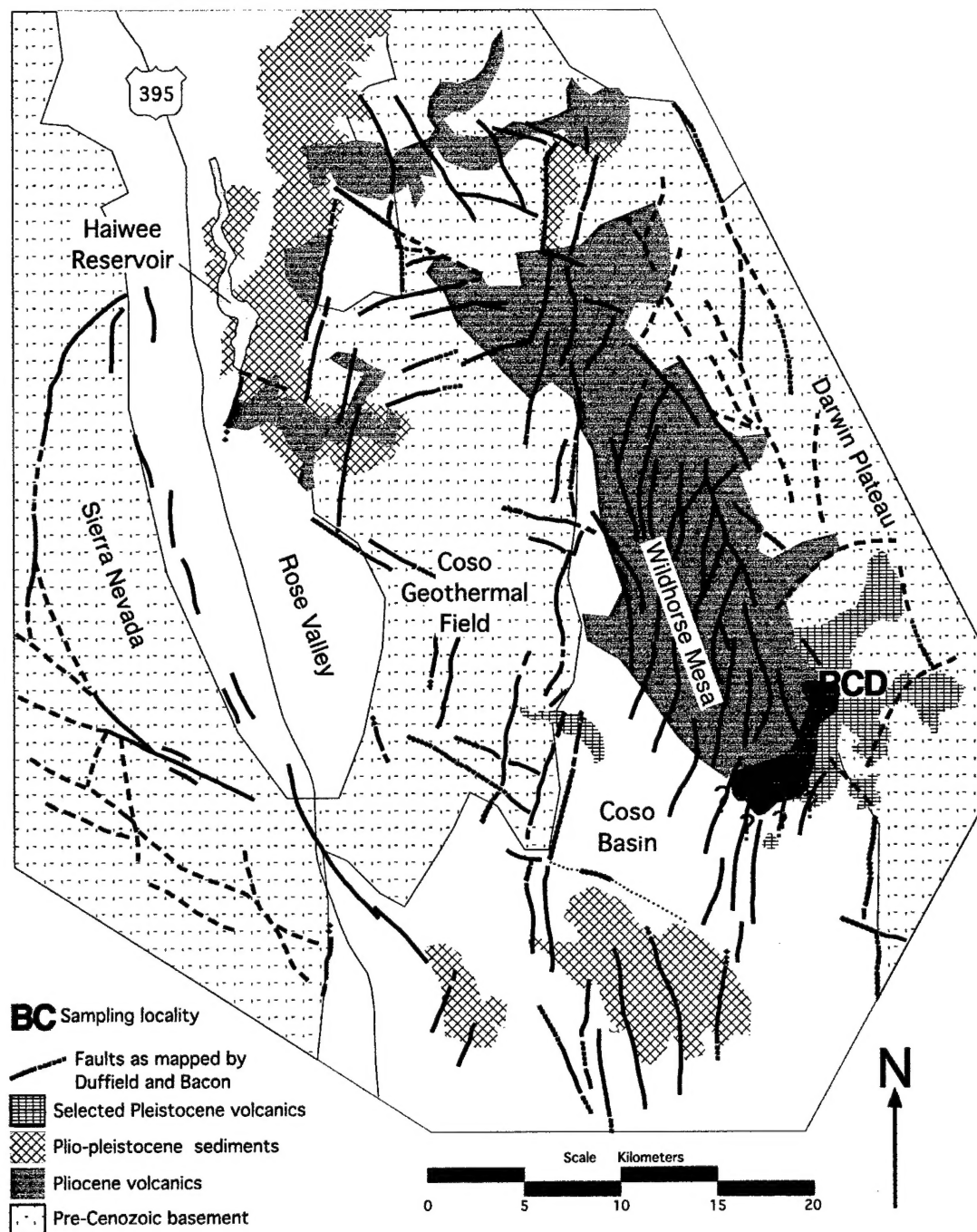


**Figure C8 - Lateral Extent of QTbr<sub>4</sub> Basalt** - in plum color. Only one cooling unit of QTbr<sub>4</sub> is visible at the localities depicted. QTbr<sub>4</sub> exhibits reversed paleomagnetic polarity (declination ~ 183°, inclination ~ -45°). Question marks indicate uncertainty on the location of the edge of the unit. This member erupted west of sampling locality RCD at an unknown time and no stratigraphic constraints are available. See main report for geochemical composition.